

We are IntechOpen, the world's leading publisher of Open Access books Built by scientists, for scientists

6,300

Open access books available

171,000

International authors and editors

190M

Downloads

Our authors are among the

154

Countries delivered to

TOP 1%

most cited scientists

12.2%

Contributors from top 500 universities



WEB OF SCIENCE™

Selection of our books indexed in the Book Citation Index
in Web of Science™ Core Collection (BKCI)

Interested in publishing with us?
Contact book.department@intechopen.com

Numbers displayed above are based on latest data collected.
For more information visit www.intechopen.com



One-Photon Absorption-Based Direct Laser Writing of Three-Dimensional Photonic Crystals

Dam Thuy Trang Nguyen, Mai Trang Do, Qinggle Li,
Quang Cong Tong, Thi Huong Au and
Ngoc Diep Lai

Additional information is available at the end of the chapter

<http://dx.doi.org/10.5772/intechopen.71318>

Abstract

A simple and low-cost technique called low one-photon absorption (LOPA) direct laser writing (DLW) is demonstrated as an efficient method for structuration of multidimensional submicrostructures. Starting from the diffraction theory of the electromagnetic field distribution of a tightly focused beam, the crucial conditions for LOPA-based DLW are theoretically investigated, and then experimentally demonstrated using a simple optical confocal microscope. Various 1D, 2D, and 3D submicrostructures were successfully fabricated in different materials, such as commercial SU8 photoresist and magnetic nanocomposite. The advantages and drawbacks of this LOPA-based DLW technique were also studied and compared with the conventional two-photon absorption based DLW. Several methods were proposed to overcome the existing problem of the DLW, such as the dose accumulation and shrinkage effect, resulting in uniform structures with a small lattice constant. The LOPA-based DLW technique should be useful for the fabrication of functionalized structures, such as magneto-photonic and plasmon photonic crystals and devices, which could be interesting for numerous applications.

Keywords: direct laser writing, one-photon absorption, photonic crystal, magnetic nanocomposite, magneto-photonic microstructures

1. Introduction

In recent years, various fabrication techniques have been proposed and implemented to realize structures at micro- and nanoscales, opening numerous applications such as micro-machining, optical data storage, nanophotonics, plasmonics, and bio-imaging, etc. [1–4]. Among those techniques, optical lithography, which includes mask lithography [5, 6], interference

or holography photolithography [7–9], and direct laser writing [10–13], is the most popular because of its simplicity, flexibility and capability of producing different kinds of microstructures, addressing a variety of applications.

The fundamental working principle of the optical lithography involves the use of a photoresist, a light-sensitive material, which changes its chemical property when exposed to light. Based on the reactions of photoresists to light, they are classified into two types: positive photoresist and negative photoresist. With positive photoresists, the areas exposed to the light absorb one or more photons and become more soluble in the photoresist developer. These exposed areas are then washed away with the photoresist developer solvent, leaving the unexposed material. With negative resists, exposure to light causes the polymerization of the photoresist chemical structure, which is just the opposite of positive photoresists. The unexposed portion of the photoresist is then dissolved by the photoresist developer. Light sources of different wavelengths are used based on the purposes of the fabrication, which involve the absorption mechanisms of the used photoresist. There are two types of absorption mechanisms, namely one-photon absorption (OPA) and two-photon absorption (TPA). The OPA excitation method is an ideal way to fabricate one- and two-dimensional (1D and 2D) thin structures [14]. In this technique, a simple and low-cost continuous-wave (CW) laser operating at a wavelength located within the absorption band of the thin film material is used as the excitation source. Wavelengths in the UV range or shorter are commonly used to achieve high resolution [15]. This method is usually applied in mask lithography and interference techniques, where an entire pattern over a wide area is created in seconds. All structures are often realized at the same time; therefore, these techniques are called parallel processes. However, due to the strong absorption effect, light is dramatically attenuated from the input surface. Thus, it is impossible for OPA to address thick film materials or 3D optical structuring.

The TPA (or multi-photon absorption) technique presents a better axial resolution. In this case, two low energy photons are simultaneously absorbed inducing the optical transition from the ground state to the excited state of the material, equivalent to the case of linear absorption (OPA). Two-photon absorption is a nonlinear process, which is several orders of magnitude weaker than linear absorption, thus very high light intensities are required to increase the number of such rare events. In practice, the process can be achieved using a pulsed (picosecond or femtosecond) laser. The TPA method is commonly applied for the technique called direct laser writing (DLW), in which a pulsed laser beam is focused into a sub-micrometer spot, resulting in a dramatic increase of the laser intensity at the focusing spot. Hence, TPA-based 3D imaging or fabrication can be achievable [4, 11, 12] with high spatial resolution.

Indeed, DLW has been proved to be an ideal way to fabricate sub-micrometric arbitrary structures, offering flexibility, ease of use, and cost effectiveness. As opposed to mask lithography and interference techniques, DLW is a serial process in which a structure is realized by scanning the focusing spot following a desired pattern. Thus, any arbitrary 1D, 2D, and 3D periodic or non-periodic pattern can be fabricated on demand.

However, as mentioned above, the TPA-based DLW requires the use of a femtosecond or picosecond laser and a complicated optical system, making it a rather expensive fabrication technique. Recently, an original method called LOPA (low one-photon absorption) DLW has

been demonstrated [16, 17], allowing one to combine the advantages of both OPA and TPA methods. Indeed, the LOPA method employs a simple, CW and low power laser, as in the case of conventional OPA, but it allows the optical addressing of 3D objects, as what could be realized by the TPA method, by using a combination of an ultralow absorption effect and a tightly focusing spot. The illustration of an absorption spectrum of photoresist shown in **Figure 1(a)** represents three absorption mechanisms, which are shown in **Figure 1(b)**: conventional OPA (solid ring), LOPA (dashed ring) and TPA (dash-dotted ring), respectively. If a laser beam, whose wavelength is positioned at the edge of the absorption band where the absorption is ultralow, is applied, the light intensity distribution remains almost the same as in the absence of material. In short, by tightly focusing an optical beam inside a thick material with a very low absorption at the operating wavelength, it is possible to address 3D imaging and 3D fabrication, as what realized by TPA method. As compared to the latter one, this LOPA-based DLW is very simple and inexpensive and it allows one to achieve very similar results.

This chapter presents theoretically and experimentally this original fabrication method, LOPA-based DLW technique, which allows the realization of multidimensional sub-micrometer photonic crystals. The advantages of this fabrication method will also be presented and compared with other fabrication techniques.

In Section 2, the theory of the LOPA-based DLW method and experimental conditions to realize 3D sub-microstructures are presented. In this case, the vectorial diffraction theory of a laser beam, tightly focused by a high numerical aperture objective lens, is extended taking into account the very low absorption of the propagating medium. Numerical calculations will also be shown.

In Section 3, it will be demonstrated experimentally that any sub-micrometer 1D, 2D, and 3D structures can be realized by the LOPA-based DLW technique, by choosing appropriate photoresist and excitation laser wavelength.

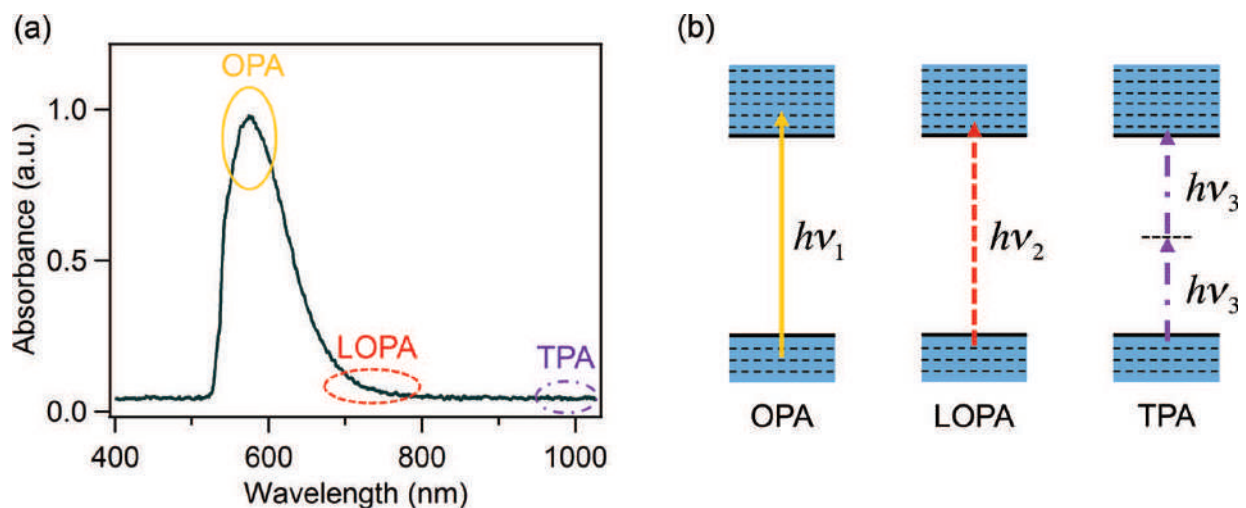


Figure 1. (a) Illustration of the absorption spectrum of a photoresist. The three rings illustrate three ranges of wavelength corresponding to (b) three absorption mechanisms: standard one-photon absorption (OPA), low one-photon absorption (LOPA), and two-photon absorption (TPA).

In Section 4, different additional methods to optimize the LOPA-based DLW are demonstrated in order to obtain sub-microstructures, which show high uniformity, less shrinkage, and with a lattice constant smaller than the diffraction limit.

To demonstrate the versatility of the LOPA-based DLW, in Section 5, the fabrication of magneto-photonic sub-microstructures for biomedical engineering realized by the LOPA-based DLW technique is presented. This opens many promising applications, such as tunable photonic structures based on magneto-optical effect and development of microrobotic tools for transport in biological systems.

In the last section, some conclusions of the newly developed LOPA-based DLW technique, advantages this technology brings to the photonic crystal field, as well as some prospects will be discussed.

2. Theory of LOPA-based DLW technique

In this section, the vectorial Debye approximation is presented, based on which a new mathematics representation is further established, where the absorption effect of the material is taken into account when a light beam propagates through an absorbing medium. Based on the new evaluation form of vectorial Debye theory, the influence of absorption coefficient of the studied material, the numerical aperture (NA) of the objective lens (OL), and the penetration depth of light beam on the formation of a tight focusing spot are investigated. From that, the crucial conditions for the realization of LOPA microscope and LOPA DLW are established.

2.1. Electromagnetic field distribution of a tight focused beam in an absorbing medium

The mathematical representation of the electromagnetic field distribution in the focal region of an OL was proposed by Wolf in the 1950s [18]. This theory based on the vectorial Debye approximation allows the calculation and prediction of the intensity and polarization distributions of a light beam focused inside a material by a high NA OL. Nonetheless, the influence of material absorption on the intensity distribution and the focused beam shape of a propagating optical wave have not been systematically investigated yet. In this section, the mathematical representation proposed by Wolf [18] will be employed, taking into account the absorption effect of the material when a focused light beam propagates through it, in order to investigate the intensity distribution, especially in the focal region.

The schematic representation of light focusing in an absorption medium is shown in **Figure 2**. D is the interface between the transparent material, such as a glass substrate or air, and the absorbing material. To simplify the problem, it is assumed that the refractive index mismatch problem arising at any interface is negligible. d represents the distance between the D interface and the focal plane. The electromagnetic field near the focal plane in Cartesian coordinates (x, y, z) [16, 19] is represented by,

$$\mathbf{E} = -\frac{ikC}{2\pi} \iint_{\Omega} \mathbf{T}(s)A(s) e^{[ik(s_x x + s_y y + s_z z)]} ds_x ds_y \quad (1)$$

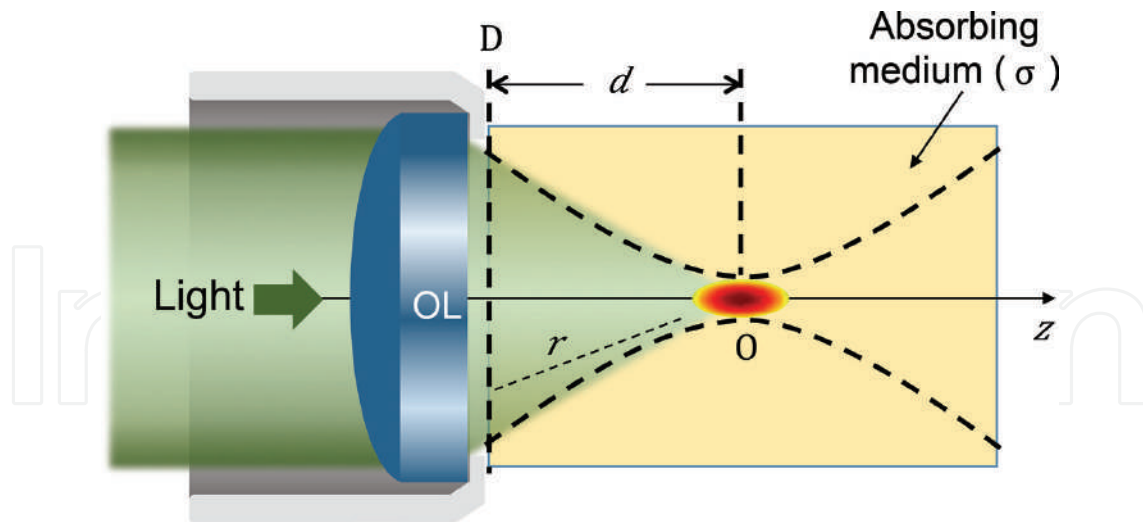


Figure 2. Schematic representation of a tightly focused light beam inside an absorbing medium. σ is the absorption coefficient of the medium, O is the focal point, D is the interface between the transparent and the absorbing media, r is the distance from an arbitrary point on the D plane to the focal point, and d is the distance between the D plane and the focal plane of the objective lens.

where C is a constant, k is the wave number ($k = 2\pi n/\lambda$), n is the refractive index of the absorbing medium, λ is the excitation wavelength, Ω is a solid angle corresponding to the objective aperture, $\mathbf{S} = (s_x, s_y, s_z)$ is the vector of an arbitrary optical ray, and $\mathbf{T}(s) = \mathbf{P}(s)\mathbf{B}(s)$ is a transmission function where $\mathbf{P}(s)$ is the polarization distribution and $\mathbf{B}(s)$ is the amplitude distribution at the exit pupil. $A(s)$ represents the absorption effect of the material, which is expressed as $A(s) = \exp(-\sigma r)$, where σ is the absorption coefficient and r indicates the optical path of each diffracted light ray in the absorbing medium, which is defined as the distance from a random point located in the D plane to the focal point, as shown in **Figure 2**. For calculations, r is determined by

$$r = \sqrt{(x'-x)^2 + (y'-y)^2 + (d-z)^2}, \quad (2)$$

where (x', y', d) gives the position of an arbitrary diffracted light ray located on the D plane. Theoretically, Eq. (1) allows calculation of the light distribution resulting from the interference of all light rays diffracted by the exit pupil of the OL. However, in practice, the light intensity and the focus shape at the focus region depend strongly on the absorption term $A(s)$ since light is absorbed by the material in which it propagates and its amplitude decreases along the propagation direction.

The light intensity distribution, also called point spread function (PSF), in the focal region of the OL is defined as

$$I_{PSF} = \mathbf{E}\mathbf{E}^* \quad (3)$$

This theory is applicable for any cases, OPA, LOPA, or TPA. It can be seen that the EM field distribution in the focal region depends on various parameters, such as the polarization of

incident light, the NA of OL, the absorption coefficient of the material, etc. It is impossible to have an analytical solution of the light field at the focusing spot of a high NA OL. However, it can be numerically calculated, which will be shown in the next part.

2.2. Numerical calculation of point spread function

In order to numerically calculate the light intensity distribution, the I_{PSF} equation was programmed by a personal code script based on Matlab software, with the influence of different input parameters including the absorption coefficient of the studied material, the NA of the OL, and the penetration depth of the light beam.

First, the influence of the absorption effect of the SU8 material, which will be used later for experimental demonstration in the next sections, was investigated. Based on the absorption spectrum of SU8 shown in **Figure 5(b)**, three typical wavelengths to calculate the intensity distribution in the focal region were chosen, representing three cases of interest: conventional OPA (308 nm), LOPA (532 nm) and TPA (800 nm), respectively. The corresponding absorption coefficients in each case are: $\sigma_1 = 240,720 \text{ m}^{-1}$ ($\lambda_1 = 308 \text{ nm}$), $\sigma_2 = 723 \text{ m}^{-1}$ ($\lambda_2 = 532 \text{ nm}$), and $\sigma_3 = 0 \text{ m}^{-1}$ ($\lambda_3 = 800 \text{ nm}$). The absorption interface (D) was arbitrarily assumed to be separated from the focal point O by a distance of 25 μm , the NA of the OL was chosen to be 0.6, the refractive index (n) of SU8 is 1.58. As seen in **Figure 3(a₁)**, the incoming light is totally attenuated at the interface D because of the strong absorption of SU8 at 308 nm, which explains why it is not possible to optically address 3D object with the conventional OPA method. However, when using an excitation light source emitting at 800 nm, the absorption coefficient is zero, thus light can penetrate deeply inside the material, resulting in a highly resolved 3D intensity distribution. The numerical calculation result derived from the quadratic dependence of the EM field is shown in **Figure 3(a₃)**. The size of the focusing spot (full width at half maximum, FWHM) is quite large due to the use of a long wavelength. However, in practice, two photons can only be simultaneously absorbed at an intensity above the polymerization threshold. Therefore, a small effective focusing spot below the diffraction limit can be achieved with the TPA method by controlling the excitation intensity.

The case where the linear absorption is very low (LOPA) was considered. At the wavelength $\lambda = 532 \text{ nm}$, the absorption coefficient is only 723 m^{-1} , which is much smaller than that at 308 nm. Simulation results show that light can penetrate deeply inside the absorbing material without significant attenuation thanks to this very low linear absorption. As shown in **Figure 3(a₂)**, the light beam can be tightly confined at the focusing spot, which can then be moved freely inside the thick material, exactly as in the case of TPA. Furthermore, LOPA requires a shorter wavelength as compared with TPA, the focusing spot size (FWHM) is therefore smaller. The diagram depicted in **Figure 3(a₄)** shows clearly the difference of the intensity distribution along the optical axis of three excitation mechanisms. It is important to note that there is no intensity threshold in the case of LOPA, because it is a linear absorption process. Therefore, LOPA requires a precise control of light dose in order to achieve high resolution optical addressing.

The NA of OL is also an important parameter to be taken into account for LOPA case. It was demonstrated that the use of a high NA OL is a crucial condition. The intensity distributions at the focusing spot obtained with OLs of different NA values (with the same low absorption

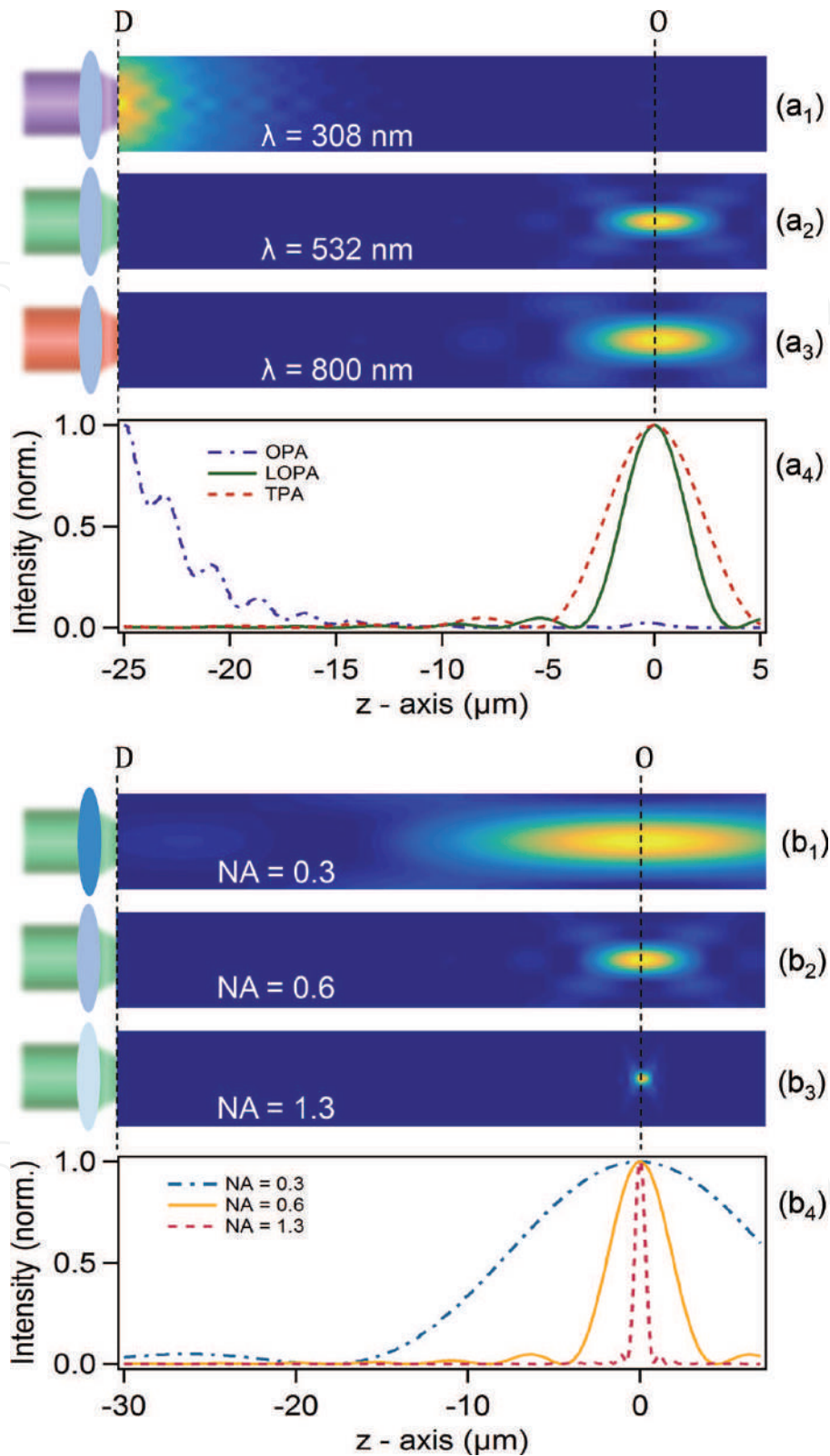


Figure 3. (a) Numerical calculations of light propagation inside SU8, by using different wavelengths, (a₁) 308 nm, (a₂) 532 nm, and (a₃) 800 nm, respectively. (a₄) Intensity distributions along z -axis of the light beams shown in (a₁₋₃). In this calculation, NA = 0.6, refractive index $n = 1.58$, and $d = 25$ μm . (b) Propagation of light ($\lambda = 532$ nm) inside SU8, with (b₁) NA = 0.3, (b₂) NA = 0.6, and (b₃) NA = 1.3, respectively, $d = 30$ μm . (b₄) Intensity distributions along z -axis of the light beams shown in (b₁₋₃).

coefficient $\sigma_2 = 723 \text{ m}^{-1}$) are shown in **Figure 3(b)**. It is clearly seen that with an OL of low NA ($\text{NA} = 0.3$), the light beam is not well focused, resulting in low contrast intensity distribution between the focal region and its surrounding. Therefore, the LOPA-based microscopy using a low NA OL cannot be applied for 3D optical addressing. However, in the case of tight focusing (for example, $\text{NA} = 1.3$), the light intensity at the focusing spot is a million time larger than that at out of focus, resulting in a highly resolved focusing spot (**Figure 3(b₃)**).

For all the above calculations, it can be concluded that the LOPA-based microscopy is promising for the realization of 3D imaging and 3D fabrication, similarly to what could be realized by TPA microscopy. By using the LOPA technique, 3D fluorescence imaging or fabrication of 3D structures can be realized by moving the focusing spot inside the material since fluorescence (for imaging) or photopolymerization (for fabrication) effects can be achieved efficiently within the focal spot volume only.

It is worth noting that in LOPA technique, the absorption exists, even if the probability is very small, the penetration depth is therefore limited to a certain level. This effect exists also in the case of TPA, but it is more important for LOPA. **Figure 4** represents the maximum intensity at the focusing spot as a function of the penetration length, d . For this calculation, the ultralow absorption coefficient of SU8 at $\lambda = 532 \text{ nm}$, $\sigma = 723 \text{ m}^{-1}$ was considered. At the distance of $390 \mu\text{m}$, the intensity was found to decrease by half with respect to that obtained at the input of absorbing material (D interface). This penetration depth of several hundred micrometers is fully compatible with the scanning range of piezoelectric stage (typically, $100 \mu\text{m}$ for a high resolution), or with the working distance of microscope OL (about $200 \mu\text{m}$ for a conventional high NA OL).

In summary, in order to realize the LOPA-based microscopy, two important conditions are required: (i) ultralow absorption of the studied material at the chosen excitation wavelength, and (ii) a high NA OL for tight focusing of the excitation light beam. To experimentally demonstrate the application of LOPA in DLW, in the next chapter, SU8 will be used as the material and a CW laser at $\lambda = 532 \text{ nm}$ as the excitation source.

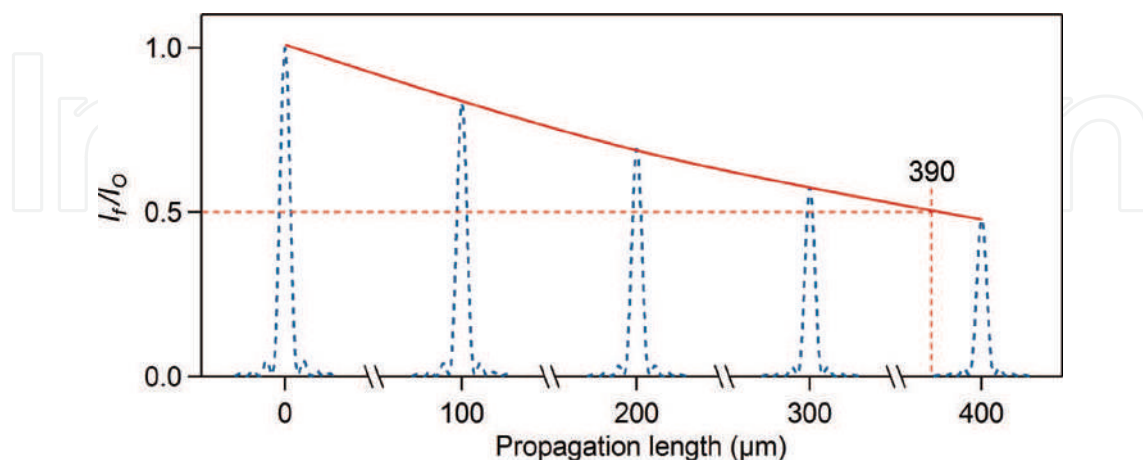


Figure 4. Red curve: normalization of intensity (I_f/I_0) at the focusing spot as a function of the propagation length. I_f and I_0 are the intensities obtained with and without absorption medium, respectively. Dot curves: zoom on intensity profiles of the focusing spot along the optical axis, calculated at different d . The results are simulated with: $\sigma = 723 \text{ m}^{-1}$; $\lambda = 532 \text{ nm}$; $\text{NA} = 1.3$ ($n = 1.58$).

3. Experimental demonstration of LOPA-based 3D microfabrication

3.1. Experimental setup and fabrication procedure

The LOPA technique can obviously be used for all 3D applications, including 3D imaging and 3D fabrication. As mentioned in section 2, two conditions are required: a photoresist that presents an ultralow absorption at the wavelength of the excitation laser, and a high focusing confocal laser scanning (CLSM) system. For the first condition, SU8 photoresist is an excellent candidate, thanks to its ultralow absorption in the visible range, for example at 532 nm (Figure 5(b)), which is the wavelength of a very popular and low-cost laser. By using a high NA oil-immersion OL of NA = 1.3 to focus a laser beam into the photoresist, the second condition is then satisfied.

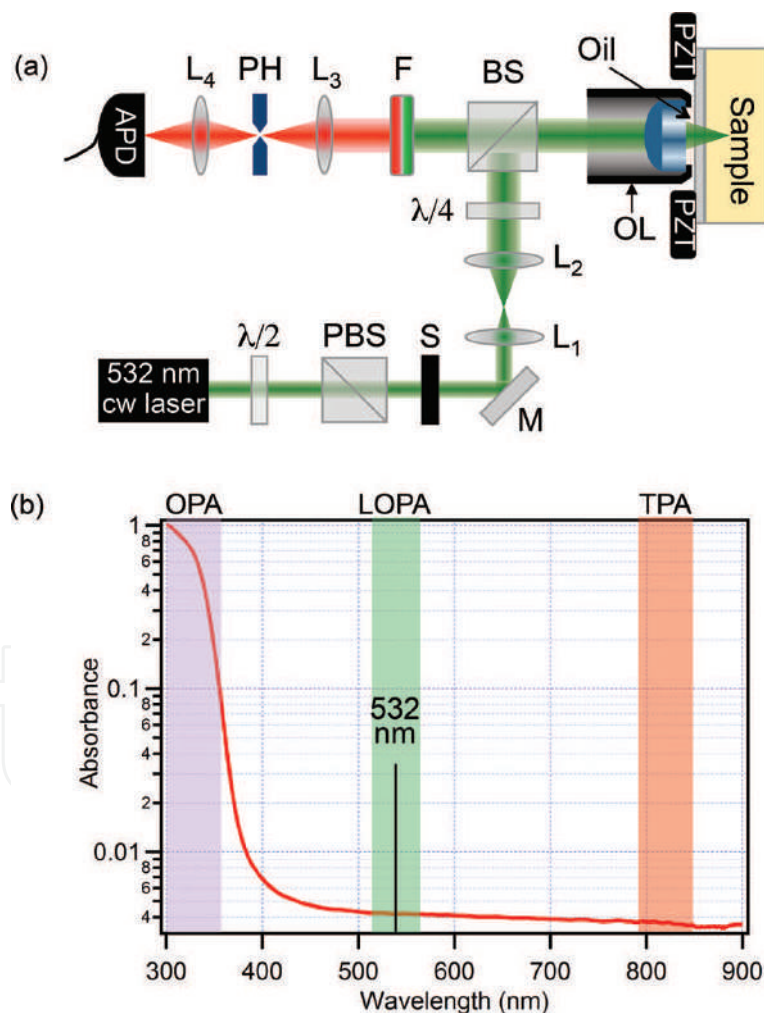


Figure 5. (a) A sketch of the experimental setup. PZT: piezoelectric translator, OL: oil immersion microscope objective, $\lambda/4$: quarter-wave plate, $\lambda/2$: half-wave plate, BS: beam splitter, PBS: polarizer beam splitter, M: mirror, S: electronic shutter, L_{1-4} : lenses, PH: pinhole, F: 580 nm long-pass filter, APD: avalanche photodiode. (b) Absorption spectrum of SU8 photoresist. The color bars indicate three cases: OPA (purple bar), LOPA (green bar), and TPA (red bar). To demonstrate LOPA DLW, a laser operating at 532 nm is used.

In order to demonstrate the LOPA DLW technique, a confocal optical system illustrated in **Figure 5(a)** was built. In this system, a CW laser operating at 532 nm is used. The laser power is monitored by a combination of a half-wave plate ($\lambda/2$) and a polarizer. The laser beam is directed and collimated by a set of lenses and mirrors. In order to realize mapping or fabrication, samples are mounted on a 3D piezoelectric actuator stage (PZT), which is controlled by a LabVIEW program. A quarter-wave plate ($\lambda/4$) placed in front of the OL is inserted and oriented to generate a circularly polarized beam for mapping and fabrication. The high NA oil-immersion objective (NA = 1.3) placed beneath the glass coverslip is used to focus the excitation laser beam. The fluorescence signal emitted by the samples is collected by the same objective, filtered by a 580 nm long-pass filter, and detected by an avalanche photodiode (APD).

For fabrication, SU8 photoresist is coated on a glass substrate. In order to remove all contamination on the surface, glass substrates must be treated with acetone and an ultra-sonication prior to the spin coating. After the cleaning process, SU8 of different viscosities (SU8 2000.5, SU8 2005, or SU8 2025) is spin coated on the glass substrates, depending on the types of the desired structure. For 1D and 2D structures, SU8 2000.5 and 2002, which give a layer thickness of 0.5 and 2 μm , are used. For 3D structures, other types of SU8 at higher viscosity, for example SU8 2005 or 2025, are required. The spin coating step is followed by a soft baking step at 65°C and 95°C, the soft baking time depends on the types of SU8 used.

Before writing the structure on the photoresist, the interface between the glass substrate and the photoresist layer must be determined. To determine the interface, the focusing spot is scanned along xz or yz plane at very low laser power to prevent polymerization, and the fluorescence signal can be collected by the APD. This step allows one to precisely write the structure at the desired position. Then the laser power is increased to several mW to fabricate any desired structures by scanning the focusing spot along a path programmed with Labview. Post exposure bake (PEB) is carried out after the fabrication, and followed by a development step.

3.2. Verification of LOPA-based fabrication

It has been demonstrated, by analyzing fluorescence emission, that the SU8 photoresist linearly absorbs the excitation laser at 532 nm-wavelength [17]. For the LOPA CLSM, the intensity at the focusing region (of the order of 10^7 W/cm^2) is much higher than that at the input of the optical system (10^{-2} W/cm^2), allowing the excitation and fluorescence detection of the focal spot volume only. The fluorescence measurements in which the emission is quite low are enabled by the use of an avalanche photodiode (APD).

By using the standard fabrication process described in the previous part, it was demonstrated that polymerization is achieved only at the focusing spot of the microscope objective, where the excitation intensity is sufficiently high to compensate the low linear absorption of the resist. In the case of TPA, there are two thresholds: the first one related to light intensity, above which two photons are simultaneously absorbed, and the second one related to dose, above which complete photopolymerization is achieved. However, in the case of LOPA, there exists only one threshold related to dose. Thanks to a high intensity at the focusing spot, the complete photopolymerization is only achieved in this region. **Figure 6** shows SEM images of experimental results. For each exposure, a solid structure, called “voxel,” corresponding to

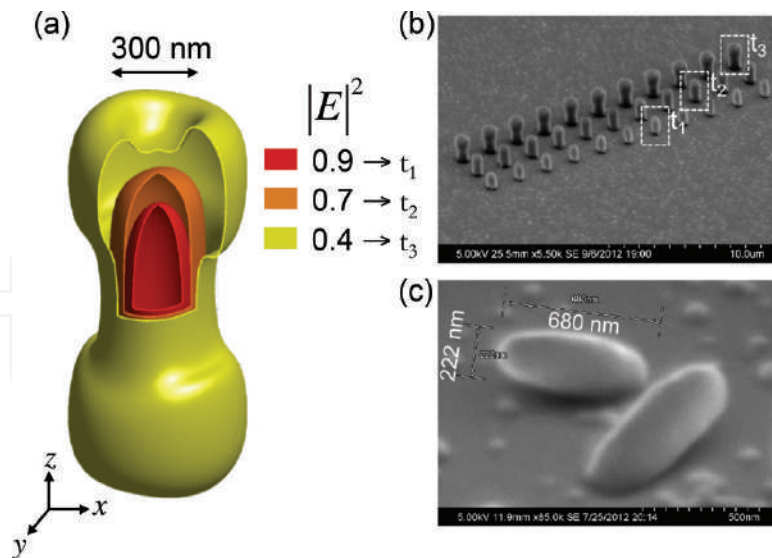


Figure 6. Fabrication of voxels by single-shot exposure. (a) Theoretical calculation of the contour plot of light intensity at the focusing region ($NA = 1.3$, $n = 1.518$, $\lambda = 532$ nm). (b) SEM image of a voxels array obtained by different exposure doses. Three ranges of voxels are fabricated correspondingly to the exposure time t_1 , t_2 and t_3 whose corresponding doses are 0.9, 0.7 and 0.4 as indicated in (a). These experimental results explain the OPA nature where the formed voxel shape is determined by the exposure dose. (c) Complete voxel lying on the substrate indicated an ellipsoidal form (exposure time t_1 was applied). This form is similar to that obtained by the TPA method.

a focusing spot, was obtained. By changing either the excitation power or the exposure time, i.e. the dose, the voxel size and shape can be adjusted, as shown in **Figure 6(b)**. A CW green laser power of only 2.5 mW and an exposure time of about 1 second per voxel were required to create these structures. **Figure 6(b)** shows, for example, a voxel array realized with three different exposure times. The dose dependence can be explained theoretically by calculating the iso-intensity of the focusing spot at different levels. Three kinds of voxels obtained with t_1 , t_2 and t_3 in **Figure 6(b)** correspond to three different iso-intensities illustrated in **Figure 6(a)**, namely 0.9, 0.7 and 0.4, respectively. The operation in the OPA regime is fully confirmed by the evolution of voxel size and shape observed experimentally. Indeed, in the case of TPA, the creation of bone-like voxel shape requires very high excitation intensity and could not be easily realized due to the TPA intensity threshold. In the case of LOPA, all these voxels shapes were obtained by simply adjusting the exposure time while the laser power is kept at a low value. Smaller voxels as shown in **Figure 6(c)** require shorter exposure times. Certainly, the exposure time required to create sub-micrometer structures varies as a function of the laser power.

Pillar arrays were also fabricated by scanning the focusing spot of the laser along the thickness of a 1 μm SU8 film with different writing speeds. **Figure 7** shows the pillar size as a function of writing velocity for three values of laser power, $P = 7.5$, 6, and 4.5 mW. The fabrication of smaller pillars down to 190 nm is possible [17]. The size of individual pillars is quite small when considering the wavelength (532 nm) used for the writing process. As for the linear dependence with intensity (OPA vs. TPA) [20, 21], the diameter-dose relationship agreement confirms this behavior, as the intensity I_0 is used for the fit, instead of I_0^2 in the case of TPA. This result confirms the fabrication of sub-microstructures by LOPA-based DLW method.

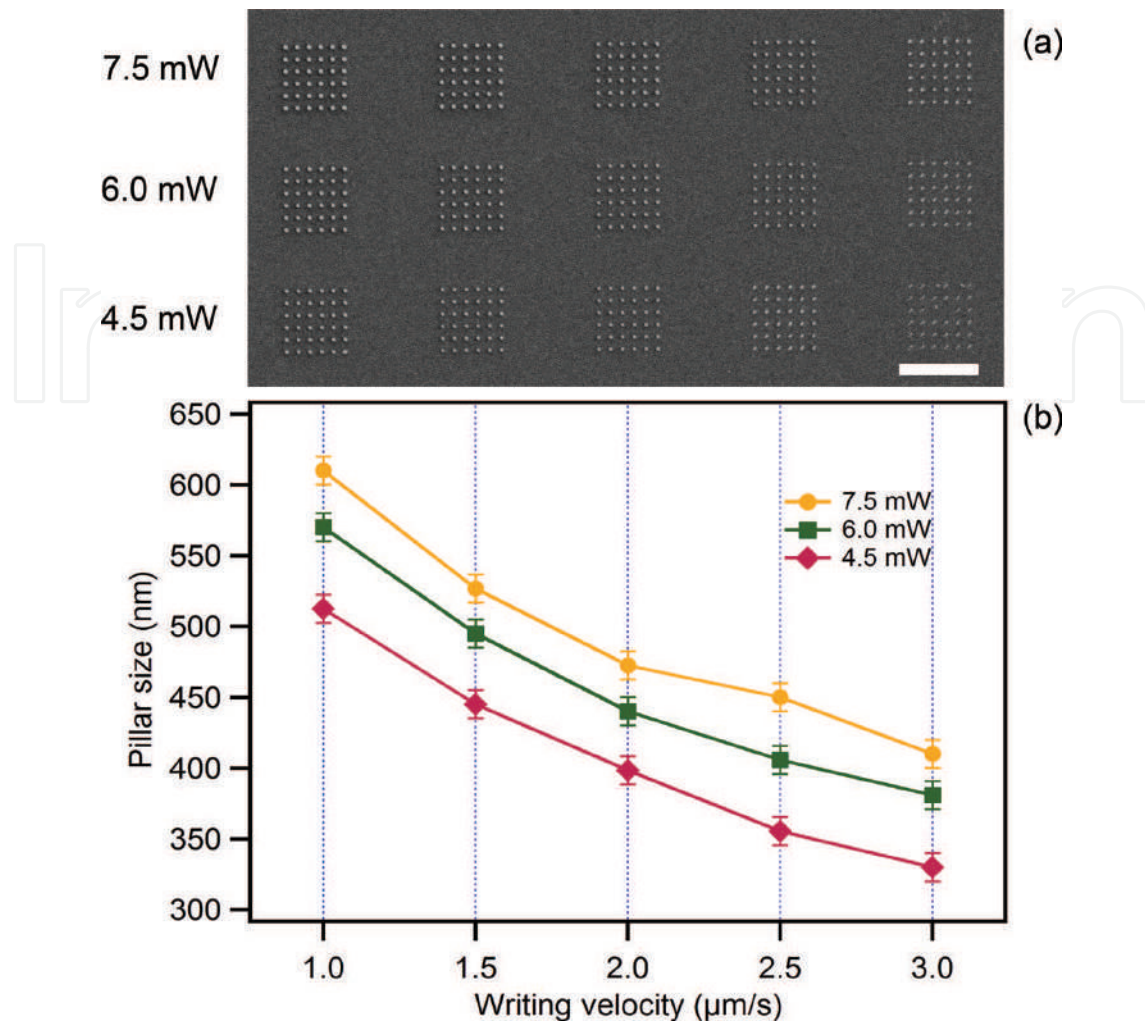


Figure 7. (a) SEM image of a pillar arrays fabricated at different writing velocity and laser powers. (b) Dose dependence of size of pillars shown in (a), with different laser power values, $P = 7.5, 6, 4.5$ mW, and different writing velocities, $v = 1.0, 1.5, 2.0, 2.5,$ and 3.0 $\mu\text{m/s}$. Scale bar: 10 μm .

3.3. LOPA-based DLW for 3D microstructure fabrication

In order to demonstrate 3D fabrication, 3D arbitrary photonic crystals (PCs) have been realized. In the fabrication process, the dose was adjusted by changing the velocity of the PZT movement while the input power is fixed. The doses were varied from structure to structure depending on the size and separation (periodicity of PC). In the first experiment, a series of different size 3D woodpile PC structure on glass substrate was fabricated. It is noted that, SU-8 exhibits a strong shrinkage effect, which results in the distortion of the fabricated structure. After a number of experiments, acceptable parameters for woodpile, which are an input power of 2.5 mW and a velocity of 1.4 $\mu\text{m/s}$, were found. Applying these parameters, 3D diamond lattice-like-based PC structures such as woodpile, twisted chiral and circular spiral can be realized.

Figure 8(a–f) shows SEM images of 3D woodpile, spiral and chiral PCs fabricated with these optimum fabrication parameters. The woodpile structure (**Figure 8(a and b)**) consists

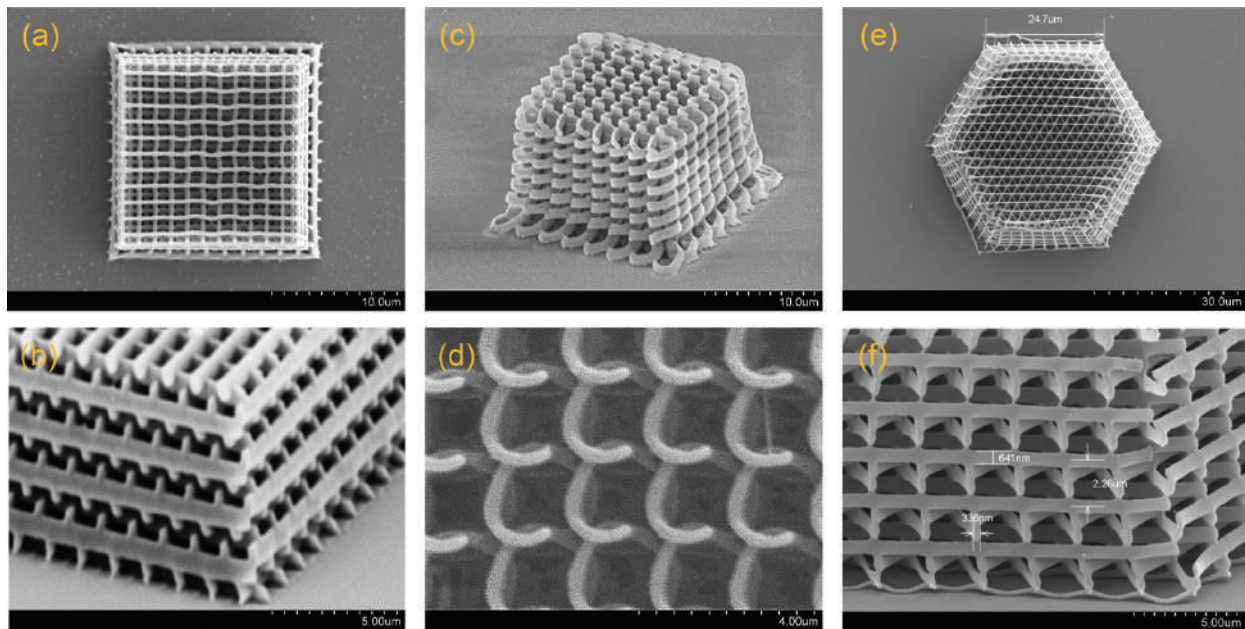


Figure 8. (a–b) SEM images of a woodpile structure fabricated with the following parameters: distance between rods = 1.5 μm ; distance between layers = 0.7 μm ; number of layers = 20; laser power $P = 2.5$ mW and scanning speed $v = 1.4$ $\mu\text{m}/\text{s}$. (c and d) SEM images of a chiral structure. Structure and fabrication parameters: distance between rods $a = 2$ μm ; distance between layers $c/3 = 0.75$ μm ; number of layers = 28; line width $r = 300$ nm; laser power $P = 2.8$ mW and scanning speed $v = 1.34$ $\mu\text{m}/\text{s}$. (e–f) SEM images of a spiral structure (shown in inset). Fabrication parameters: diameter of a spiral $D = 2$ μm ; spiral pitch $C = 2$ μm ; lattice constant $a = 3$ μm ; spiral height equals to film thickness = 15 μm ; laser power $P = 2.6$ mW and scanning speed $v = 1.34$ $\mu\text{m}/\text{s}$.

of stacked 20 layers. Each layers consists of parallel rods with period $a = 1.5$ μm . Rods in successive layers are rotated by an angle of 90° relative to each other. Second nearest-neighbor layers are displaced by $a/2$ relative to each other. Four layers form a lattice constant $c = 2.1$ μm . SEM measurement shows that the line width of rods on the top layer is about 320 nm, which is 1.5 times of the voxel standard size. This means that the size of the rod can be minimized further. Woodpile structure with measured separation between rods on the top layer of only 800 nm and the measured line width of 180 nm was also successfully fabricated. This result shows evidently that separation of rods and layers are comparable to the wavelength of visible light. **Figure 8(c–f)** shows, as examples, two other kinds of sub-micrometer 3D structures. Clearly, 3D chiral or spiral structures are well created, which are as good as those obtained by TPA DLW. The structures features are well separated, layer by layer, in horizontal and in vertical directions. The feature sizes are about 300 nm (horizontal) and 650 nm (vertical).

Experimental realization of LOPA-DLW in fabrication of 1D, 2D and 3D photonic crystal showed evidently the advantage of LOPA idea in combining with regular DLW. With a few milliwatts of a CW laser and in a moderate time, any kind of sub-micrometer structure with or without designed defect could be fabricated. However, some fabricated structures are not uniform or distorted. The physical causes of the distortion can be attributed to two main effects: dose accumulation effect [22] and shrinkage effects [23]. In the next section, some techniques to overcome those effects will be experimentally demonstrated.

4. Optimization of LOPA-based DLW technique

4.1. Dose accumulation effect

As a consequence of linear behavior of absorption mechanism, the dose accumulation effect is the inherent nature of linear absorption material [24, 25]. In contrast to a conventional TPA method, a photoresist operated in OPA regime does not have any threshold of polymerization [26], hence the voxel size can be controlled by adjusting the exposure dose. In principle, polymerization occurs at the focusing spot with a single-shot exposure resulting in a very small voxel (smaller than the diffraction limit) [27]. However, when two voxels are built side-by-side with a distance of about several hundred nanometers, two resulting voxels are no longer separated [17]. This issue evidently originates from the dose accumulation effect in OPA process.

Similar to OPA microscopy where the microscopy image cannot resolve two small objects which localize at about several hundred nanometers from each other, the fabricated voxels in DLW also cannot be separated. Abbe's criterion states that, the minimum resolving distance of two objects is defined as $0.61\lambda/\text{NA}$, where λ is the wavelength of incident light. This diffraction barrier thus imposes the minimum distance between different voxels, created by different exposures. Moreover, when multiple exposures are applied, although isolated voxel fabrication is ideally confined to the focal volumetric spot, the superposition of many out-of-focus regions of densely-spaced voxels leads to undesired and unconfined reaction. This results in the larger effective voxel size, even with a distance far from the diffraction limit. Indeed, in the case of OPA, photons could be absorbed anywhere they are, with an efficiency depending on the linear absorption cross-section of the irradiated material. The absorbed energy is gradually accumulated as a function of exposure time.

Figure 9 shows the theoretical calculations and experimental results of the dependence of the voxels size on distance. When two voxels are separated by a distance shorter than $1\ \mu\text{m}$, a clear accumulation effect is observed, resulting in a voxel of larger size. When the separation changes from 2 to $0.5\ \mu\text{m}$, the FWHM of each voxel is increased from 190 to $300\ \text{nm}$. Moreover, for a short separation, the voxels array is not uniform from the center to the edge part, as can be seen in case of a separation of $0.5\ \mu\text{m}$. In the parts below, two strategies to get rid of this accumulation effect are discussed.

4.1.1. Dose compensation strategy

According to the structures fabricated by LOPA DLW and the theoretical calculation, the dose accumulation effect should be compensated in order to get superior structure uniformity. The compensation technique idea is based on a balance of the exposure doses over the structure. In other words, a certain amount of the exposure dose should be reduced at the region (or a part or a division) where the dose accumulation effect strongly occurs and should be added to the region where the dose is lacking.

As demonstrated above, the accumulation effect depends on the separation distance, s . 2D micropillars array was fabricated by scanning the focusing spot along the z -axis to demonstrate

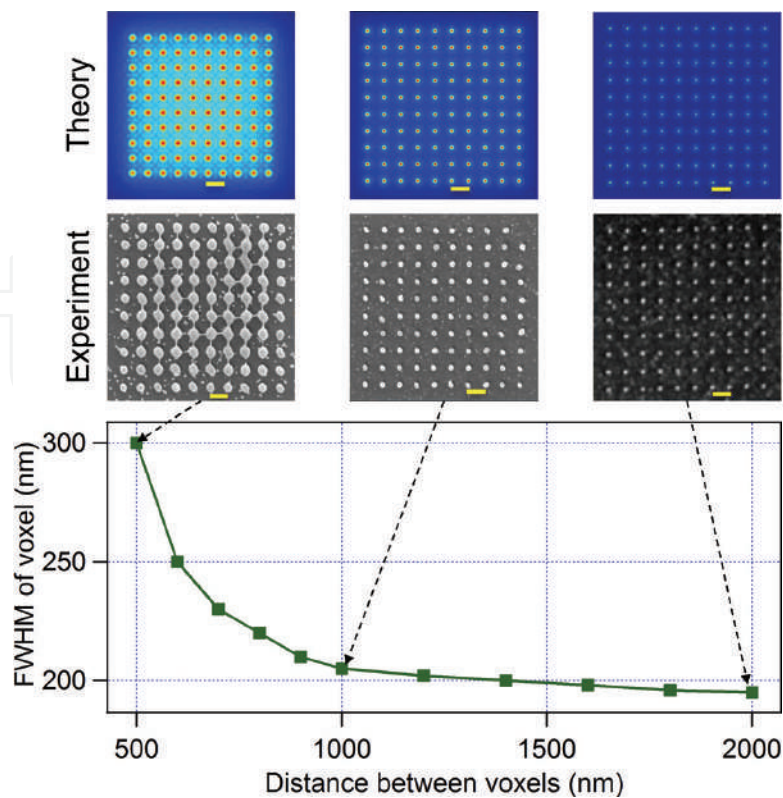


Figure 9. Dependence of voxel sizes on separation between voxels calculated at the iso-intensity = 0.5 ($I = I_0/2$), showing the influence of energy accumulation from one focusing spot to another. Insets show simulated images (blue background) and SEM images (gray background) of 2D voxel arrays fabricated with different distances between two voxels: 2, 1, and 0.5 μm . Scale bar (from left to right): 0.5, 1, and 2 μm .

the accumulation effect and the dose compensation technique. The variation of the pillars size as a function of s distance, from 0.3 to 3 μm , has been systematically investigated [22]. According to the pillars size variation, from the center to the edge of the structure, the size difference could be compensated by gradually increasing the exposure doses for outer pillars. The intensity distribution of a pillar array and the dose compensation strategy are shown in **Figure 10(a)**. Different dose compensation ratios have been experimentally applied, indicated by letters A, B, C, and D. Two sets of structures have been fabricated on the same sample in order to maintain the same experimental conditions: one without and the other with dose compensation. The accumulation effect in the case of $s = 0.4 \mu\text{m}$, obtained without compensation, is shown in **Figure 10(b)**. It can be seen that the structure is not uniform, and the outmost voxels collapse into central pillars. With dose compensation, i.e. the doses for outer pillars are increased, 2D micropillars arrays become uniform. Structures realized with different dose ratios, corresponding to A, B, C, and D schemes depicted in **Figure 10(a)**, are shown in **Figure 10(c–f)**. With high dose compensation amplitude, the size of outer pillars becomes even larger than those in the center. By using an appropriate dose compensation ratio, perfectly uniform 2D micropillars array is obtained, as shown in **Figure 10(c)**. The structure period is only 400 nm, the height of pillars is about 700 nm, and pillar's diameter is about 160 nm. Structures with periods of several hundred nanometers are very suitable for photonic applications in visible range.

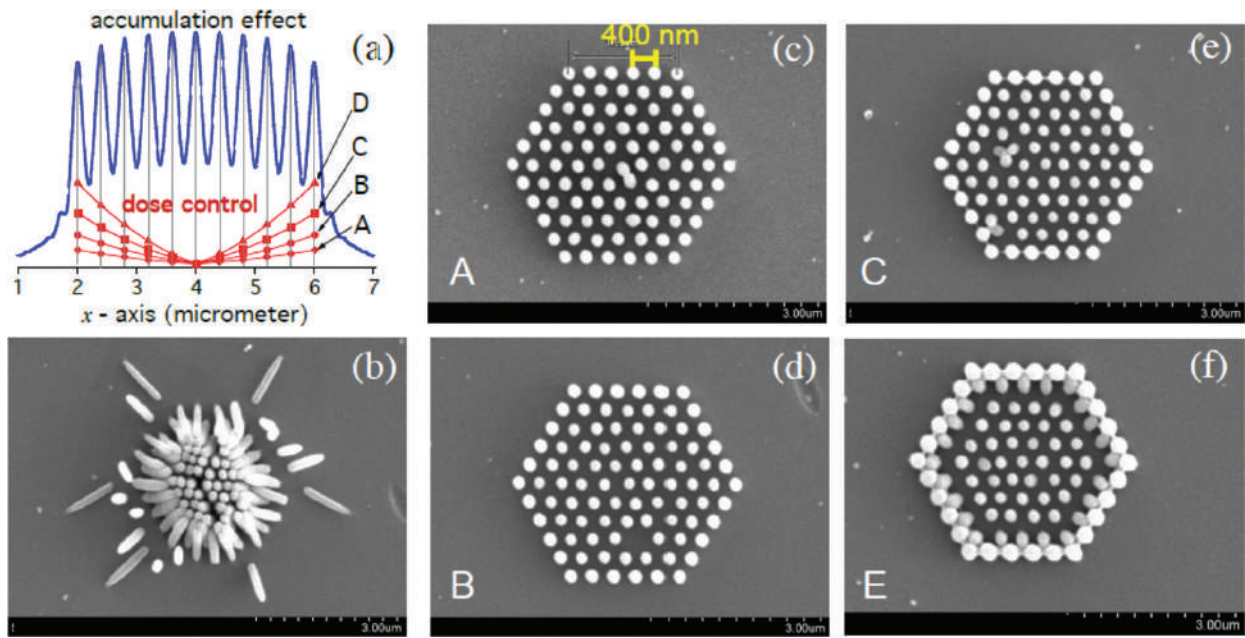


Figure 10. Compensation of dose accumulation for $s = 0.4 \mu\text{m}$. (a) Theoretical calculation of the intensity distribution as a function of x -position (blue color), and proposition of different doses, indicated by A, B, C, and D (red color) to compensate the dose accumulation effect. (b–f) SEM images of 2D hexagonal structures realized without compensation (b), and with compensation with different doses: A (c); B (d); C (e), and D (f). The excitation power was fixed at 2.5 mW and the dose was adjusted by changing the writing velocity.

4.1.2. Local PEB for small and uniform microstructures

The dose compensation techniques are presented above and proved to be able to compensate the size difference in the structures. Nonetheless, this technique requires numerous calculations and tests in order to find out the appropriate dose compensation parameters. For example, for the fabrication of other 2D structures with a sub-micrometer period containing an arbitrary defect, such as a microcavity or a waveguide of arbitrary shape, the dose should be controlled for individual voxel (or pillar) as a function of its position in the structure and with respect to the defect. This requires many attempts to find out the optimized parameters since the dose compensation is different for different structures.

In this part, the thermal effect induced by a CW green laser in the LOPA-based DLW technique has been investigated, which plays a role as a heat assistant for completing the crosslinking process of the photopolymerization of SU8 [28]. The fabrication of sub-microstructures using LOPA DLW with a laser-induced thermal effect, also called local PEB, was demonstrated, and it was also shown to alter the traditional PEB on a hot plate and help overcome the accumulation effect existing in standard LOPA DLW.

For the demonstration of local PEB, two sets of 2D structures were fabricated, each set contains pillar arrays written at different doses (by varying the laser power and the writing speed). One set was realized following the traditional process, i.e., after exposure, the sample was post-baked for 1 min at 65°C and then 3 min at 95°C using a hot plate. For the other set, the PEB step was skipped, which means that the exposure process was followed directly by the

development process. It has been observed that for the same dose, the pillars fabricated without PEB are smaller than those fabricated with PEB [28]. Due to the fact that the structures are not formed at low power (low light intensity), it is assumed that the applied laser power or intensity must be above a threshold in order to induce enough heat for the crosslinking process, and this threshold should be higher than that of standard LOPA (with PEB) for a complete photopolymerization.

Figure 11(a) shows the accumulation effect observed in the structures fabricated using traditional PEB process at different doses. The distance between two pillars is 500 nm, which is considered as a sufficiently short separation to induce noticeable accumulation effect. It can be observed that the pillar size decreases from the center to the edge, with a variation of 10–20%, resulting in non-uniform structures. **Figure 11(b)** shows the SEM images of structures obtained using local PEB. In this case, in order to induce sufficiently high temperature, the laser power (5 mW) was higher than that (3 mW) used with traditional PEB step. In contrast to the structures fabricated using traditional PEB, which shows accumulation effect (**Figure 11(a)** on the top), the structures obtained with local PEB show nearly perfect uniformity (**Figure 11(b)** on the top). Moreover, as compared to the dose compensation method, the LOPA-based DLW using local PEB does not require testing, since the dose applied is constant for all voxels and the range of applicable doses is large. In addition, the PEB step is skipped, which is a great advantage in terms of fabrication time. Furthermore, comparing to structures realized by TPA-based DLW, the period of these fabricated structures is much shorter (only 500 nm or even 400 nm) thanks to the use of short laser wavelength, which can be an additional advantage of this LOPA technique.

The heat equation [29] was also solved using finite element model realized by Matlab to demonstrate that the heat induced by high excitation intensity of a 532 nm CW laser confines the crosslinking reaction in the local region where the temperature is higher than the PEB temperature. This resulted in fine and uniform structures, since only the material within the effective temperature region was properly polymerized. Temperature-depth dependence calculation shows that this technique allows the fabrication of uniform 3D sub-micro structures with large thickness. This is then evident by an experimental demonstration of fabrication of a uniform 3D woodpile structure without PEB step, with a period as small as 400 nm [28]. Compared to the commonly used TPA method, LOPA-based DLW with local PEB shows numerous advantages such as simple, low-cost setup and simplified fabrication process, while producing same high-quality structures.

4.2. Shrinkage effect

Shrinkage is a fundamental issue for photopolymerization in the photopolymer. It is difficult to avoid the non-uniformity when the conventional polymerized microstructures are attached to substrates. The origin of this effect for TPA polymerization has been investigated [30]. It was suggested that the origin of the shrinkage is the collapse of this material during the development stage owing to the polymer not being fully cross-linked when they are made at the irradiation power close to the photopolymerization threshold. At fabrication intensities slightly above the photopolymerization threshold, the photopolymerization yield is not

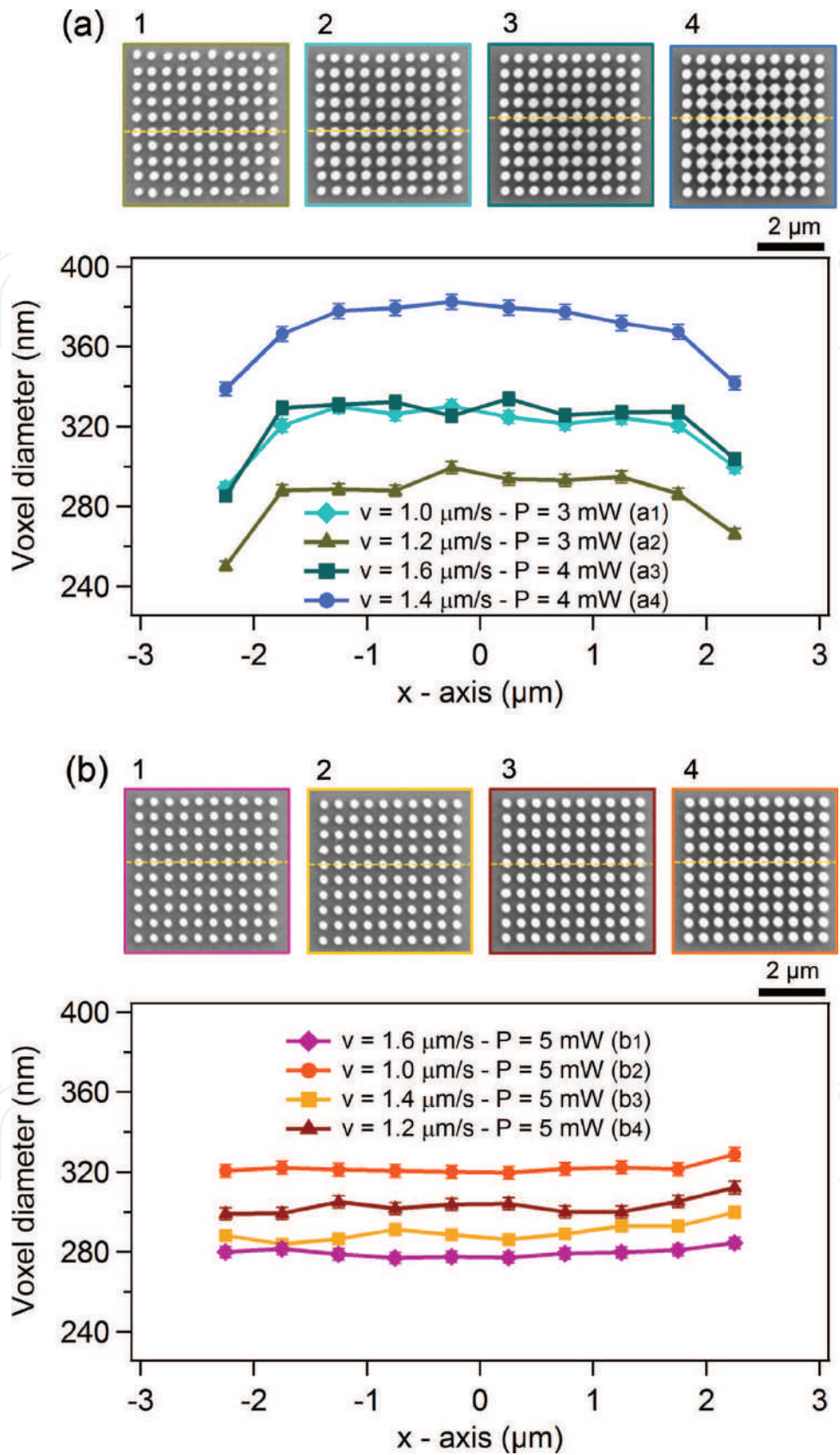


Figure 11. Comparison between structures fabricated with standard PEB (a) and local PEB (b) shows the advantage of “local PEB” in overcoming the accumulation effect. Left: SEM images of fabricated structures. Top: sizes of pillars indicated by the dashed line on SEM images plotted as a function of position. With standard PEB: the pillars are larger at center of pattern. With local PEB: pillars are very uniform. All structures are fabricated with a period of 500 nm.

100%, resulting in a sponge-like material after the development process. Hence, the structural shrinkage observed at average laser powers is the result of the collapse of this material at a molecular level [30]. However, it has also been confirmed that, although the sponge-like materials are formed during the development because of the non-full polymerization at low laser power, the shrinkage indeed occurs due to the capillary forces and the dramatic change of surface tension during the drying process [31].

For LOPA 3D fabrication, this shrinkage effect is also observed, with different levels of distortion for different exposure doses, i.e., the lower the exposure dose is the higher the shrinkage is. (Figure 12a–d) shows the shrinkage effect observed in 3D woodpile structures fabricated at different doses ($P = 9$ mW, writing speed $v = 4, 3, 2,$ and 1 $\mu\text{m/s}$, from left to right, respectively). It can be clearly seen that the degree of shrinkage at different exposure doses is different, i.e., from left to right, the writing speed decreases (the dose increases), the shrinkage decreases. This result is also in agreement with previous report on the shrinkage in the case of TPA polymerization [30], which suggests that in both cases, the shrinkage effect might have a similar origin.

Non-uniform shrinkage might destroy the structural periodicity of a photonic crystal, resulting in the degradation of its optical quality. While shrinkage is an intrinsic problem, which cannot be avoided, non-uniform shrinkage problem can be positively resolved. Several approaches have been reported on how to overcome this non-uniform shrinkage, including pre-compensation for deformation [32], single [33] and multi-anchor supporting method [30, 34], or freestanding microstructures trapped in cages [35]. All the above methods are investigated for the TPA case. In this work, the multi-anchor supporting method was employed to reduce the deformation caused by the non-uniform shrinkage of 3D microstructures by LOPA DLW. To demonstrate this idea, instead of fabricating woodpile structures directly on glass substrate, four “legs” at four corners of structures were created in order to avoid the attachment of the structures to the glass substrate, which is the direct cause of the non-uniform

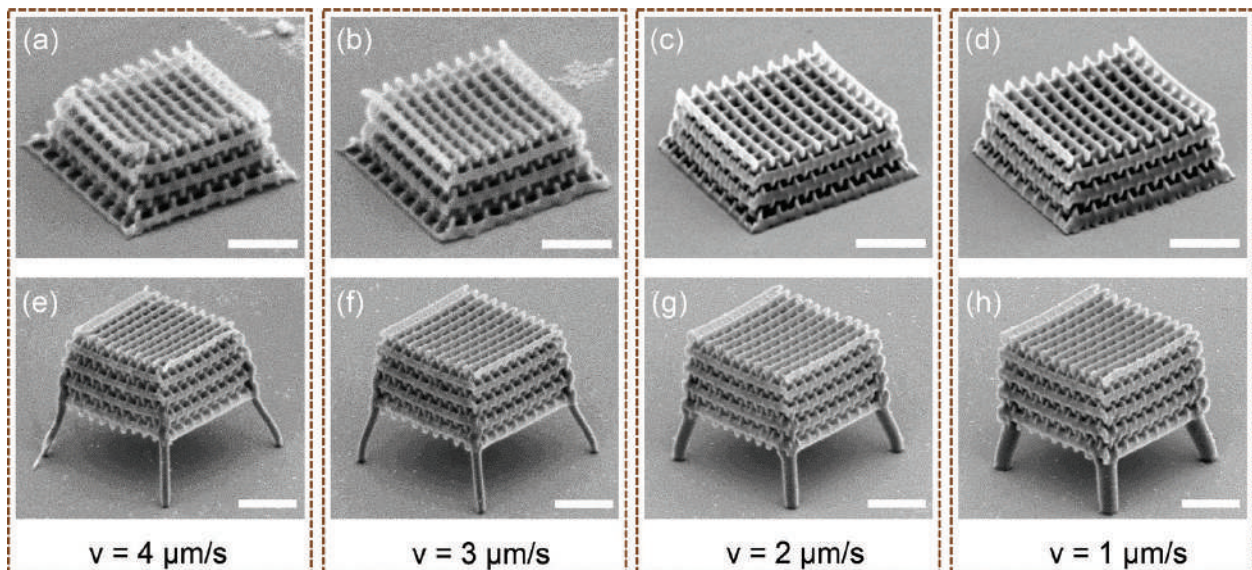


Figure 12. 3D woodpile structures (number of layers =16, rod spacing = 1.5 μm and layer spacing = 0.65 μm) fabricated without (a–d) and with “legs” (e–h), at laser power of 9 mW and different writing speeds: $v = 4, 3, 2,$ and 1 $\mu\text{m/s}$, from left to right. Scale bars: 5 μm .

shrinkage. These anchors were designed and fabricated as rods of several hundred nanometers and did not affect the main structure. (**Figure 12e–h**) shows woodpile structures with anchors fabricated at different doses. It can be seen that at low dose, the non-uniform shrinkage still remains as shown in **Figure 12(e)**. However, when the dose is increased by a small amount, the distortion decreases and disappears. In this case, a laser power of 9 mW and a writing speed of 3 $\mu\text{m/s}$ were sufficient for a considerable uniform structure. Compared to the non-anchored structures, the fabrication speed is reduced by three times to obtain a nearly deformation-free PC, which is remarkable especially for the fabrication of large structures. The shrinkage effect can also be exploited to produce PCs with small lattice constant.

To conclude, the multi-anchor supporting method was successfully applied to reduce the non-uniform deformation of 3D microstructure caused by attachment to the substrate. Since the support with four anchors allows uniform shrinkage of a polymeric microstructure by releasing it from the substrate, the fabricated microstructure shrinks isotropically. The combination of LOPA with local PEB and this supporting method is a promising way of producing small lattice constant photonic structures, which possess a photonic bandgap in the visible range.

5. Realization of magneto-photonic microstructures by LOPA-based DLW

LOPA-based DLW has been demonstrated to be not only applicable for SU8 but also other materials [36, 37], and be capable of fabricating structures incorporated with nanoparticles (NPs), such as plasmonic [38] or magnetic NPs [39]. In this section, as a proof of the versatility of LOPA DLW, the fabrication of 2D and 3D sub-microstructures from nanocomposite consisting of magnetite (Fe_3O_4) NPs and a commercial SU8 photoresist by employing LOPA DLW technique is presented [39]. The nanocomposite was synthesized by incorporating magnetic nanoparticles (MNPs) into SU8 matrix. Due to the magnetic force (mainly inter-particle interactions), MNPs tend to form large agglomerations, causing difficulties in achieving a homogeneous distribution of MNPs in polymer matrix. Hence, different concentrations of Fe_3O_4 MNPs and various types of SU8 with different viscosities have been investigated to obtain the best dispersion of MNPs in the polymer environment. Finally, the best compromise was achieved between SU8 2005, with moderate viscosity, and a MNP concentration of 2 wt%, which is low enough to achieve a homogeneous nanocomposite and high enough to give strong response to external magnetic field.

Arbitrary magnetic structures from magneto-polymer nanocomposite have been realized using LOPA DLW. **Figure 13(a)** shows an SEM image of an arbitrary 2D structure, the letter "LPQM," fabricated at the power of 15 mW with a writing speed of 3 $\mu\text{m/s}$. For this fabrication, a point matrix technique was used to shape the letter. The distance between pillars was set at 150 nm, which resulted in a continuous line due to the accumulation of exposure energy at the vicinity of each point. An SEM image of a 2D pillar array magneto-photonic structure, with a period of 1.5 μm is shown in **Figure 13(b)**. This structure was fabricated at

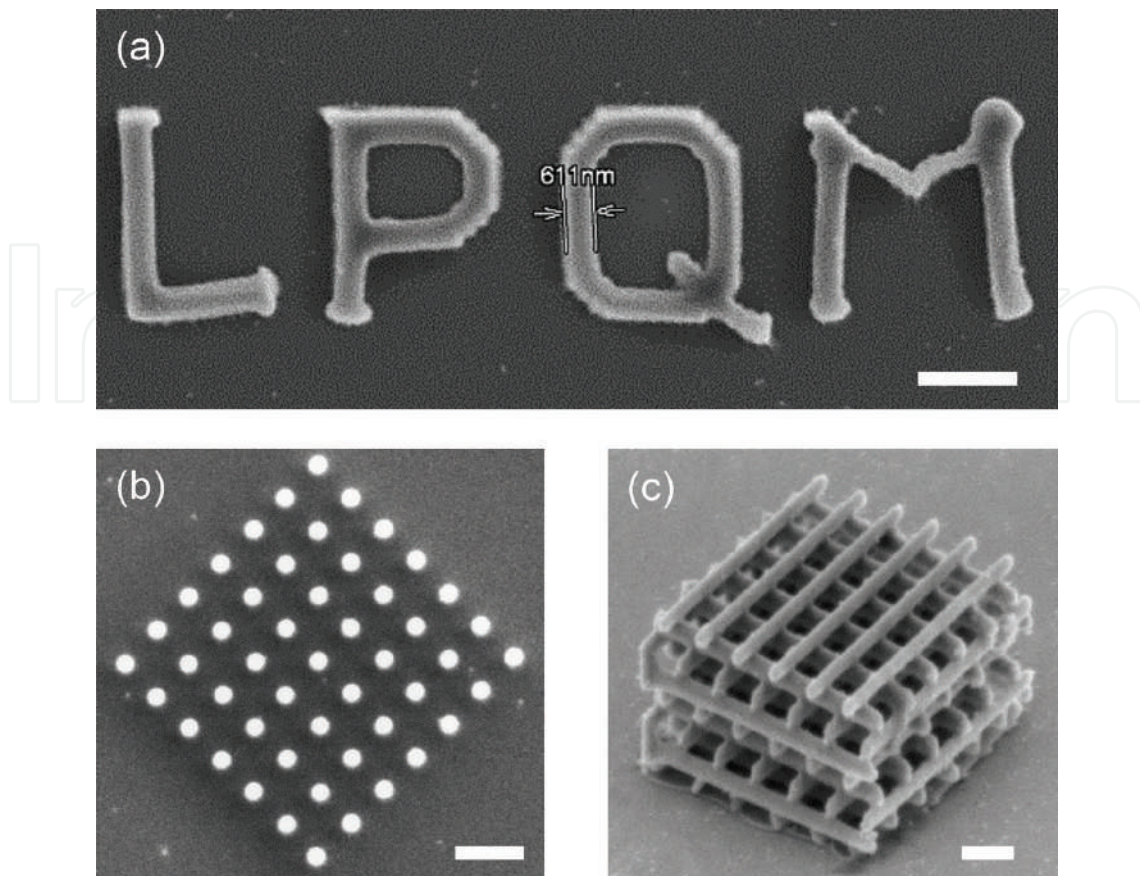


Figure 13. (a) SEM image of letter LPQM, fabricated at a laser power $P = 15$ mW, writing speed $v = 3$ $\mu\text{m/s}$. (b) SEM image of a 2D pillar array, fabricated at $P = 12$ mW, $v = 2$ $\mu\text{m/s}$. (c) SEM image of a 3D woodpile PC. Fabrication parameters: rod spacing = 2 μm ; distance between layers = 1 μm ; number of layers = 10; laser power $P = 12$ mW and scanning speed $v = 2$ $\mu\text{m/s}$. Scale bars: 2 μm .

a laser power of 12 mW and a writing speed of 2 $\mu\text{m/s}$. Similarly, various 3D structures have also been realized, with a laser power of about 12 mW. **Figure 13(c)** shows an SEM image of a woodpile structure, which consists of 10 alternating layers separated from each other by 1 μm . The rod spacing in x - and y -directions is 2 μm . These experimental results confirm that the LOPA-based DLW allows the fabrication of any magneto-photonic sub-micrometer structure or device on this magneto-polymer nanocomposite, which is very promising for a wide range of applications using magnetic microdevices and micro-robotic tools.

Indeed, magneto-photonic structures for remote actuation have attracted a great deal of attention recently [40]. With the aid of an external magnetic field, the displacement in three dimensions of magnetic structures can be controlled as desired. As shown previously, small magneto-photonic structures, which are adaptable to small targets, have been created. In order to prove the response of magnetic structures to a magnetic field, arrays of micro-pillars were fabricated as an example for demonstration [39]. To release the structures from the substrate, before coating the nanocomposite layer, an extra sacrificial layer of PMMA, which can be dissolved with acetone to release the structures into solution, was added. A magnetic field

(only 8 mT) generated by a permanent magnet was then applied to examine the magnetic field response of the magnetic micro-swimmers. The whole process from structural development to the movement toward higher gradient of the external magnetic field was observed via optical microscope, in which all of the micro-pillars quickly moved toward the magnetic tip, confirming the presence of Fe_3O_4 MNPs inside the structures and their strong response to the applied magnetic field. The magnetic structures responded strongly to the external magnetic field, opening many promising applications, such as tunable photonic structures based on magneto-optical effect and development of microrobotic tools for transport in biological systems.

6. Conclusions and prospects

In this chapter, a new technique based on an already-well-known mechanism, one-photon absorption (OPA) direct laser writing (DLW), for fabrication of low-cost, high-quality 3D PCs was introduced. This technique was demonstrated through both theory and experiment on the ultra-low absorption regime (LOPA) of photosensitive material. It was pointed out that DLW based on LOPA microscopy enables 3D fabrication in any kind of photoresist material with flexible defect engineering.

Some additional methods, such as dose compensation and local PEB, have been also proposed and applied to optimize the structures fabricated by LOPA DLW. In particular, by using the optically induced thermal effect, the fabrication of accumulation-free sub-micrometer and uniform polymeric 2D and 3D structures was realized. Also, the multi-anchor supporting method was employed to reduce the deformation caused by the non-uniform shrinkage of 3D polymeric microstructures.

As a proof of the versatility of the LOPA-based DLW technique, the capability to fabricate magneto-photonic microstructures using a $\text{SU8}/\text{Fe}_3\text{O}_4$ nanocomposite has been demonstrated. The fabricated micro-swimmers showed strong response to an applied external magnetic field, which emphasizes the importance of free-floating structures as a robotic technology for magnetic devices such as sensors, actuators, magnetic labeling, and drug targeting. 3D magneto-photonic structures have also been successfully fabricated, potentially aiding the development of magnetic nanodevices and micro-robotic tools for a wide range of applications.

Author details

Dam Thuy Trang Nguyen, Mai Trang Do, Qinggle Li, Quang Cong Tong, Thi Huong Au and Ngoc Diep Lai*

*Address all correspondence to: nlai@lpqm.ens-cachan.fr

Laboratoire de Photonique et Moléculaire, Ecole Normale Supérieure de Cachan, CentraleSupélec, CNRS, Université Paris-Saclay, Cachan, France

References

- [1] Lin SY, Fleming JG, Hetherington DL, Smith BK, Biswas R, Ho KM, et al. A three-dimensional photonic crystal operating at infrared wavelengths. *Nature*. 1998;**394**(6690):251-253
- [2] Cumpston BH, Ananthavel SP, Barlow S, Dyer DL, Ehrlich JE, Erskine LL, et al. Two-photon polymerization initiators for three-dimensional optical data storage and micro-fabrication. *Nature*. 1999;**398**:51-54
- [3] Strickler JH, Webb WW. Three-dimensional data storage in refractive media by two-photon point excitation. *Optics Letters*. 1991;**16**:1780-1782
- [4] Denk W, Strickler JH, Webb WW. Two-photon laser scanning fluorescence microscopy. *Science*. 1990;**248**:73-76
- [5] Alkaisi MM, Blaikie RJ, McNab SJ, Cheung R, Cumming DRS. Sub-diffraction-limited patterning using evanescent near-field optical lithography. *Applied Physics Letters*. 1999;**75**(22):3560-3562
- [6] Mata A, Fleischman A, Roy S. Fabrication of multi-layer SU-8 microstructures. *Journal of Micromechanics and Microengineering*. 2006;**16**:276-284
- [7] Campbell M, Sharp DN, Harrison MT, Denning RG, Turberfield AJ. Fabrication of photonic crystals for the visible spectrum by holographic. *Nature*. 2000;**404**(6773):53-56
- [8] Lai ND, Liang WP, Lin JH, Hsu CC, Lin CH. Fabrication of two- and three-dimensional periodic structures by multi-exposure of two-beam interference technique. *Optics Express*. 2005;**13**(23):9605-9611
- [9] Lai ND, Zheng TS, Do DB, Lin JH, Hsu CC. Fabrication of desired three-dimensional structures by holographic assembly technique. *Applied Physics A*. 2010;**100**(1):171-175
- [10] Seet KK, Mizeikis V, Juodkazis S, Misawa H. Three-dimensional horizontal circular spiral photonic crystals with stop gaps below 1 μm . *Applied Physics Letters*. 2006;**88**(22):221101-221103
- [11] Sun HB, Matsuo S, Misawa H. Three-dimensional photonic crystal structures achieved with two-photon absorption photopolymerization of resin. *Applied Physics Letters*. 1999;**74**(6):786-788
- [12] Gissibl T, Thiele S, Herkommer A, Giessen H. Two-photon direct laser writing of ultra-compact multi-lens objectives. *Nature Photonics*. 2016;**10**:554-560
- [13] Straub M, Gu M. Near-infrared photonic crystals with higher-order bandgaps generated by two-photon photopolymerization. *Optics Letters*. 2002;**27**(20):1824-1826
- [14] Rensch C, Hell S, Schickfus MV, Hunklinger S. Laser scanner for direct writing lithography. *Applied Optics*. 1989;**28**(17):3754-3758
- [15] Bratton D, Yang D, Dai J, Ober CK. Recent progress in high resolution lithography. *Polymers for Advanced Technologies*. 2006;**17**:94-103

- [16] Li Q, Do MT, Ledoux-Rak I, Lai ND. Concept for three-dimensional optical addressing by ultralow one-photon absorption method. *Optics Letters*. 2013;**38**(22):4640-4643
- [17] Do MT, Nguyen TTN, Li Q, Benisty H, Ledoux-Rak I, Lai ND. Submicrometer 3D structures fabrication enabled by one-photon absorption direct laser writing. *Optics Express*. 2013;**21**(18):20964-20973
- [18] Wolf E. Electromagnetic diffraction in optical systems I. An integral representation of the image field. *Proceedings of the Royal Society A*. 1959;**253**(1274):349-357
- [19] Helseth LE. Focusing of atoms with strongly confined light potentials. *Optics Communication*. 2002;**212**(4-6):343-352
- [20] Sun HB, Tanaka T, Kawata S. Three-dimensional focal spots related to two-photon excitation. *Applied Physics Letters*. 2002;**80**(20):3673-3675
- [21] Lee CH, Chang TW, Lee KL, Lin JY, Wang J. Fabricating high-aspect-ratio sub-diffraction-limit structures on silicon with two-photon photopolymerization and reactive ion etching. *Applied Physics A*. 2004;**79**(8):2027-2031
- [22] Do MT, Li Q, Ledoux-Rak I, and Lai ND. Optimization of LOPA-based direct laser writing technique for fabrication of submicrometric polymer two- and three-dimensional structures. *Proc. SPIE 9127, Photonic Crystal Materials and Devices XI*. 2014
- [23] Matta JA, Outwater JO. The nature, origin and effects of internal stresses in reinforced plastic laminates. *Polymer Engineering and Science*. 1962;**2**(4):314-319
- [24] Scott TF, Kloxin CJ, Forman DL, McLeod RR, Bowman CN. Principles of voxel refinement in optical direct write lithography. *Journal of Materials Chemistry*. 2011;**21**:14150-14155
- [25] Chen KS, Lin IK, Ko FH. Fabrication of 3D polymer microstructures using electron beam lithography and nanoimprinting technologies. *Journal of Micromechanics and Microengineering*. 2005;**15**(10):1894-1903
- [26] Correa DS, Boni LD, Otuka AJG, Tribuzi V, Mendonça CR. Two-photon polymerization fabrication of doped microstructures. In: De Souza Gomes A, editor. *Polymerization*. Rijeka: InTech; 2012
- [27] Li L, Gattass RR, Gershgoren E, Hwang H, Fourkas JT. Achieving $\lambda/20$ resolution by one-color initiation and deactivation of polymerization. *Science*. 2009;**324**(5929):910-913
- [28] Nguyen DTT, Tong QC, Ledoux-Rak I, Lai ND. One-step fabrication of submicrostructures by low one-photon absorption direct laser writing technique with local thermal effect. *Journal of Applied Physics*. 2016;**119**(1):013101-013106
- [29] Carslaw HS, Jaeger JC. *Conduction of Heat in Solids*. 2nd ed. United Kingdom: Oxford University Press; 2000
- [30] Ovsianikov A, Shizhou X, Farsari M, Vamvakaki M, Fotakis C, Chichkov BN. Shrinkage of microstructures produced by two-photon polymerization of Zr-based hybrid photosensitive materials. *Optics Express*. 2009;**17**(4):2143-2148

- [31] Sun Q, Ueno K, Misawa H. In situ investigation of the shrinkage of photopolymerized micro/nanostructures: The effect of the drying process. *Optics Letters*. 2012;**37**(4):710-712
- [32] Sun HB, Suwa T, Takada K, Zaccaria RP, Kim MS, Lee KS, et al. Shape precompensation in two-photon laser nanowriting of photonic lattices. *Applied Physics Letters*. 2004;**85**(17):3708-3710
- [33] Maruo S, Hasegawa T, Yoshimura N. Single-anchor support and supercritical CO₂ drying enable high-precision microfabrication of three-dimensional structures. *Optics Express*. 2009;**17**(23):20945-20951
- [34] Lim TW, Son Y, Yang SY, Pham TA, Kim DP, Yang BI, et al. Net shape manufacturing of three-dimensional SiCN ceramic microstructures using an isotropic shrinkage method by introducing shrinkage guiders. *International Journal of Applied Ceramic Technology*. 2008;**5**(3):258-264
- [35] Sun Q, Juodkazis S, Murazawa N, Mizeikis V, Misawa H. Freestanding and movable photonic microstructures fabricated by photopolymerization with femtosecond laser pulses. *Journal of Micromechanics and Microengineering*. 2010;**20**(3):035004
- [36] Mao F, Tong QC, Nguyen DTT, Huong AT, Odessey R, Saudrais F, et al. LOPA-based direct laser writing of multi-dimensional and multi-functional photonic submicrostructures. *Proceedings of SPIE 10115, Advanced Fabrication Technologies for Micro/Nano Optics and Photonics X*. 2017;1011509
- [37] Tong QC, Luong MH, Remmel J, Do MT, Nguyen DTT, Lai ND. Rapid direct laser writing of desired plasmonic nanostructures. *Optics Letters*. 2017;**42**(12):2382-2385
- [38] Do MT, Nguyen DTT, Ngo HM, Ledoux-Rak I, Lai ND. Controlled coupling of a single nanoparticle in polymeric microstructure by low one-photon absorption-based direct laser writing technique. *Nanotechnology*. 2015;**26**(10):105301
- [39] TH A, Trinh DT, Tong QC, Do DB, Nguyen DP, Phan MH. Direct laser writing of magneto-photonic sub-microstructures for prospective applications in biomedical engineering. *Nanomaterials*. 2017;**7**(5):105
- [40] Markides H, Rotherham M, El Haj AJ. Biocompatibility and toxicity of magnetic nanoparticles in regenerative medicine, biocompatibility and toxicity of magnetic nanoparticles in regenerative medicine. *Journal of Nanomaterials*. 2012;**2012**:614094

We are IntechOpen, the world's leading publisher of Open Access books Built by scientists, for scientists

6,300

Open access books available

171,000

International authors and editors

190M

Downloads

Our authors are among the

154

Countries delivered to

TOP 1%

most cited scientists

12.2%

Contributors from top 500 universities



WEB OF SCIENCE™

Selection of our books indexed in the Book Citation Index
in Web of Science™ Core Collection (BKCI)

Interested in publishing with us?
Contact book.department@intechopen.com

Numbers displayed above are based on latest data collected.
For more information visit www.intechopen.com



One-Photon Absorption-Based Direct Laser Writing of Three-Dimensional Photonic Crystals

Dam Thuy Trang Nguyen, Mai Trang Do, Qinggle Li,
Quang Cong Tong, Thi Huong Au and
Ngoc Diep Lai

Additional information is available at the end of the chapter

<http://dx.doi.org/10.5772/intechopen.71318>

Abstract

A simple and low-cost technique called low one-photon absorption (LOPA) direct laser writing (DLW) is demonstrated as an efficient method for structuration of multidimensional submicrostructures. Starting from the diffraction theory of the electromagnetic field distribution of a tightly focused beam, the crucial conditions for LOPA-based DLW are theoretically investigated, and then experimentally demonstrated using a simple optical confocal microscope. Various 1D, 2D, and 3D submicrostructures were successfully fabricated in different materials, such as commercial SU8 photoresist and magnetic nanocomposite. The advantages and drawbacks of this LOPA-based DLW technique were also studied and compared with the conventional two-photon absorption based DLW. Several methods were proposed to overcome the existing problem of the DLW, such as the dose accumulation and shrinkage effect, resulting in uniform structures with a small lattice constant. The LOPA-based DLW technique should be useful for the fabrication of functionalized structures, such as magneto-photonic and plasmon photonic crystals and devices, which could be interesting for numerous applications.

Keywords: direct laser writing, one-photon absorption, photonic crystal, magnetic nanocomposite, magneto-photonic microstructures

1. Introduction

In recent years, various fabrication techniques have been proposed and implemented to realize structures at micro- and nanoscales, opening numerous applications such as micro-machining, optical data storage, nanophotonics, plasmonics, and bio-imaging, etc. [1–4]. Among those techniques, optical lithography, which includes mask lithography [5, 6], interference

or holography photolithography [7–9], and direct laser writing [10–13], is the most popular because of its simplicity, flexibility and capability of producing different kinds of microstructures, addressing a variety of applications.

The fundamental working principle of the optical lithography involves the use of a photoresist, a light-sensitive material, which changes its chemical property when exposed to light. Based on the reactions of photoresists to light, they are classified into two types: positive photoresist and negative photoresist. With positive photoresists, the areas exposed to the light absorb one or more photons and become more soluble in the photoresist developer. These exposed areas are then washed away with the photoresist developer solvent, leaving the unexposed material. With negative resists, exposure to light causes the polymerization of the photoresist chemical structure, which is just the opposite of positive photoresists. The unexposed portion of the photoresist is then dissolved by the photoresist developer. Light sources of different wavelengths are used based on the purposes of the fabrication, which involve the absorption mechanisms of the used photoresist. There are two types of absorption mechanisms, namely one-photon absorption (OPA) and two-photon absorption (TPA). The OPA excitation method is an ideal way to fabricate one- and two-dimensional (1D and 2D) thin structures [14]. In this technique, a simple and low-cost continuous-wave (CW) laser operating at a wavelength located within the absorption band of the thin film material is used as the excitation source. Wavelengths in the UV range or shorter are commonly used to achieve high resolution [15]. This method is usually applied in mask lithography and interference techniques, where an entire pattern over a wide area is created in seconds. All structures are often realized at the same time; therefore, these techniques are called parallel processes. However, due to the strong absorption effect, light is dramatically attenuated from the input surface. Thus, it is impossible for OPA to address thick film materials or 3D optical structuring.

The TPA (or multi-photon absorption) technique presents a better axial resolution. In this case, two low energy photons are simultaneously absorbed inducing the optical transition from the ground state to the excited state of the material, equivalent to the case of linear absorption (OPA). Two-photon absorption is a nonlinear process, which is several orders of magnitude weaker than linear absorption, thus very high light intensities are required to increase the number of such rare events. In practice, the process can be achieved using a pulsed (picosecond or femtosecond) laser. The TPA method is commonly applied for the technique called direct laser writing (DLW), in which a pulsed laser beam is focused into a sub-micrometer spot, resulting in a dramatic increase of the laser intensity at the focusing spot. Hence, TPA-based 3D imaging or fabrication can be achievable [4, 11, 12] with high spatial resolution.

Indeed, DLW has been proved to be an ideal way to fabricate sub-micrometric arbitrary structures, offering flexibility, ease of use, and cost effectiveness. As opposed to mask lithography and interference techniques, DLW is a serial process in which a structure is realized by scanning the focusing spot following a desired pattern. Thus, any arbitrary 1D, 2D, and 3D periodic or non-periodic pattern can be fabricated on demand.

However, as mentioned above, the TPA-based DLW requires the use of a femtosecond or picosecond laser and a complicated optical system, making it a rather expensive fabrication technique. Recently, an original method called LOPA (low one-photon absorption) DLW has

been demonstrated [16, 17], allowing one to combine the advantages of both OPA and TPA methods. Indeed, the LOPA method employs a simple, CW and low power laser, as in the case of conventional OPA, but it allows the optical addressing of 3D objects, as what could be realized by the TPA method, by using a combination of an ultralow absorption effect and a tightly focusing spot. The illustration of an absorption spectrum of photoresist shown in **Figure 1(a)** represents three absorption mechanisms, which are shown in **Figure 1(b)**: conventional OPA (solid ring), LOPA (dashed ring) and TPA (dash-dotted ring), respectively. If a laser beam, whose wavelength is positioned at the edge of the absorption band where the absorption is ultralow, is applied, the light intensity distribution remains almost the same as in the absence of material. In short, by tightly focusing an optical beam inside a thick material with a very low absorption at the operating wavelength, it is possible to address 3D imaging and 3D fabrication, as what realized by TPA method. As compared to the latter one, this LOPA-based DLW is very simple and inexpensive and it allows one to achieve very similar results.

This chapter presents theoretically and experimentally this original fabrication method, LOPA-based DLW technique, which allows the realization of multidimensional sub-micrometer photonic crystals. The advantages of this fabrication method will also be presented and compared with other fabrication techniques.

In Section 2, the theory of the LOPA-based DLW method and experimental conditions to realize 3D sub-microstructures are presented. In this case, the vectorial diffraction theory of a laser beam, tightly focused by a high numerical aperture objective lens, is extended taking into account the very low absorption of the propagating medium. Numerical calculations will also be shown.

In Section 3, it will be demonstrated experimentally that any sub-micrometer 1D, 2D, and 3D structures can be realized by the LOPA-based DLW technique, by choosing appropriate photoresist and excitation laser wavelength.

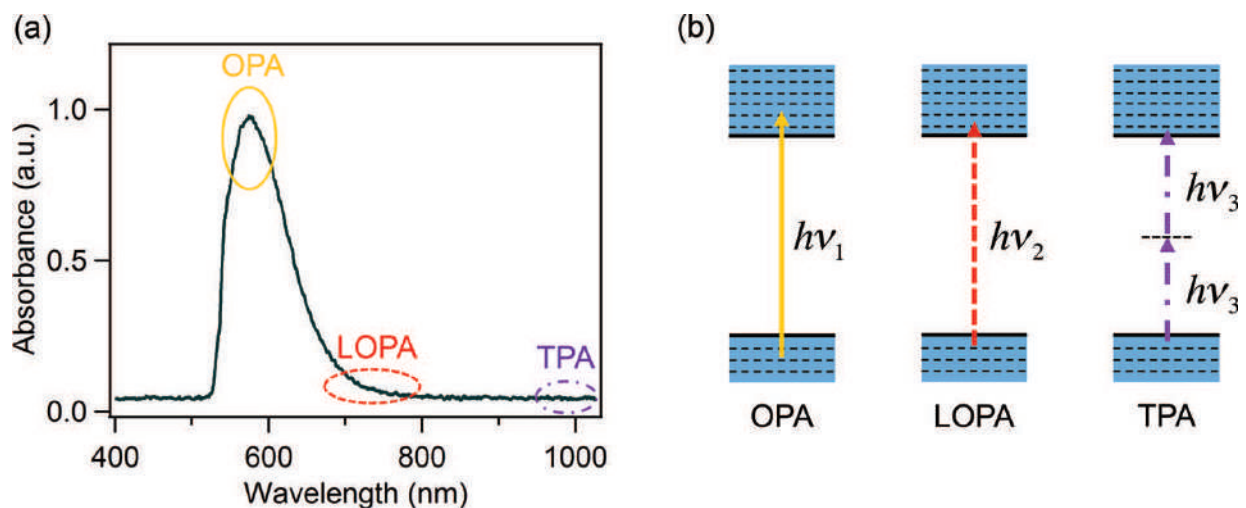


Figure 1. (a) Illustration of the absorption spectrum of a photoresist. The three rings illustrate three ranges of wavelength corresponding to (b) three absorption mechanisms: standard one-photon absorption (OPA), low one-photon absorption (LOPA), and two-photon absorption (TPA).

In Section 4, different additional methods to optimize the LOPA-based DLW are demonstrated in order to obtain sub-microstructures, which show high uniformity, less shrinkage, and with a lattice constant smaller than the diffraction limit.

To demonstrate the versatility of the LOPA-based DLW, in Section 5, the fabrication of magneto-photonic sub-microstructures for biomedical engineering realized by the LOPA-based DLW technique is presented. This opens many promising applications, such as tunable photonic structures based on magneto-optical effect and development of microrobotic tools for transport in biological systems.

In the last section, some conclusions of the newly developed LOPA-based DLW technique, advantages this technology brings to the photonic crystal field, as well as some prospects will be discussed.

2. Theory of LOPA-based DLW technique

In this section, the vectorial Debye approximation is presented, based on which a new mathematics representation is further established, where the absorption effect of the material is taken into account when a light beam propagates through an absorbing medium. Based on the new evaluation form of vectorial Debye theory, the influence of absorption coefficient of the studied material, the numerical aperture (NA) of the objective lens (OL), and the penetration depth of light beam on the formation of a tight focusing spot are investigated. From that, the crucial conditions for the realization of LOPA microscope and LOPA DLW are established.

2.1. Electromagnetic field distribution of a tight focused beam in an absorbing medium

The mathematical representation of the electromagnetic field distribution in the focal region of an OL was proposed by Wolf in the 1950s [18]. This theory based on the vectorial Debye approximation allows the calculation and prediction of the intensity and polarization distributions of a light beam focused inside a material by a high NA OL. Nonetheless, the influence of material absorption on the intensity distribution and the focused beam shape of a propagating optical wave have not been systematically investigated yet. In this section, the mathematical representation proposed by Wolf [18] will be employed, taking into account the absorption effect of the material when a focused light beam propagates through it, in order to investigate the intensity distribution, especially in the focal region.

The schematic representation of light focusing in an absorption medium is shown in **Figure 2**. D is the interface between the transparent material, such as a glass substrate or air, and the absorbing material. To simplify the problem, it is assumed that the refractive index mismatch problem arising at any interface is negligible. d represents the distance between the D interface and the focal plane. The electromagnetic field near the focal plane in Cartesian coordinates (x, y, z) [16, 19] is represented by,

$$\mathbf{E} = -\frac{ikC}{2\pi} \iint_{\Omega} \mathbf{T}(s)A(s) e^{[ik(s_x x + s_y y + s_z z)]} ds_x ds_y \quad (1)$$

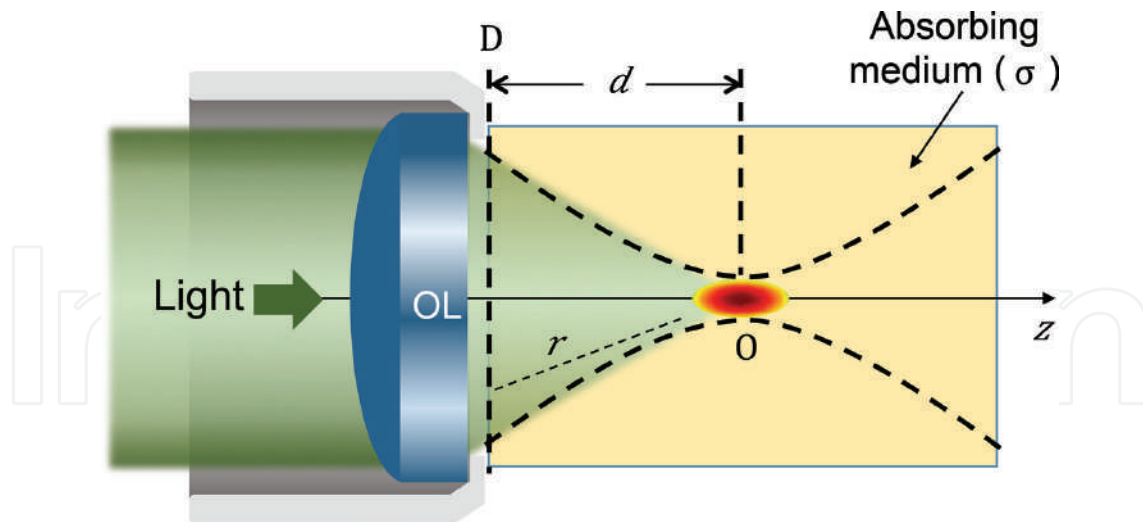


Figure 2. Schematic representation of a tightly focused light beam inside an absorbing medium. σ is the absorption coefficient of the medium, O is the focal point, D is the interface between the transparent and the absorbing media, r is the distance from an arbitrary point on the D plane to the focal point, and d is the distance between the D plane and the focal plane of the objective lens.

where C is a constant, k is the wave number ($k = 2\pi n/\lambda$), n is the refractive index of the absorbing medium, λ is the excitation wavelength, Ω is a solid angle corresponding to the objective aperture, $\mathbf{S} = (s_x, s_y, s_z)$ is the vector of an arbitrary optical ray, and $\mathbf{T}(s) = \mathbf{P}(s)\mathbf{B}(s)$ is a transmission function where $\mathbf{P}(s)$ is the polarization distribution and $\mathbf{B}(s)$ is the amplitude distribution at the exit pupil. $A(s)$ represents the absorption effect of the material, which is expressed as $A(s) = \exp(-\sigma r)$, where σ is the absorption coefficient and r indicates the optical path of each diffracted light ray in the absorbing medium, which is defined as the distance from a random point located in the D plane to the focal point, as shown in **Figure 2**. For calculations, r is determined by

$$r = \sqrt{(x'-x)^2 + (y'-y)^2 + (d-z)^2}, \quad (2)$$

where (x', y', d) gives the position of an arbitrary diffracted light ray located on the D plane. Theoretically, Eq. (1) allows calculation of the light distribution resulting from the interference of all light rays diffracted by the exit pupil of the OL. However, in practice, the light intensity and the focus shape at the focus region depend strongly on the absorption term $A(s)$ since light is absorbed by the material in which it propagates and its amplitude decreases along the propagation direction.

The light intensity distribution, also called point spread function (PSF), in the focal region of the OL is defined as

$$I_{PSF} = \mathbf{E}\mathbf{E}^* \quad (3)$$

This theory is applicable for any cases, OPA, LOPA, or TPA. It can be seen that the EM field distribution in the focal region depends on various parameters, such as the polarization of

incident light, the NA of OL, the absorption coefficient of the material, etc. It is impossible to have an analytical solution of the light field at the focusing spot of a high NA OL. However, it can be numerically calculated, which will be shown in the next part.

2.2. Numerical calculation of point spread function

In order to numerically calculate the light intensity distribution, the I_{PSF} equation was programmed by a personal code script based on Matlab software, with the influence of different input parameters including the absorption coefficient of the studied material, the NA of the OL, and the penetration depth of the light beam.

First, the influence of the absorption effect of the SU8 material, which will be used later for experimental demonstration in the next sections, was investigated. Based on the absorption spectrum of SU8 shown in **Figure 5(b)**, three typical wavelengths to calculate the intensity distribution in the focal region were chosen, representing three cases of interest: conventional OPA (308 nm), LOPA (532 nm) and TPA (800 nm), respectively. The corresponding absorption coefficients in each case are: $\sigma_1 = 240,720 \text{ m}^{-1}$ ($\lambda_1 = 308 \text{ nm}$), $\sigma_2 = 723 \text{ m}^{-1}$ ($\lambda_2 = 532 \text{ nm}$), and $\sigma_3 = 0 \text{ m}^{-1}$ ($\lambda_3 = 800 \text{ nm}$). The absorption interface (D) was arbitrarily assumed to be separated from the focal point O by a distance of 25 μm , the NA of the OL was chosen to be 0.6, the refractive index (n) of SU8 is 1.58. As seen in **Figure 3(a₁)**, the incoming light is totally attenuated at the interface D because of the strong absorption of SU8 at 308 nm, which explains why it is not possible to optically address 3D object with the conventional OPA method. However, when using an excitation light source emitting at 800 nm, the absorption coefficient is zero, thus light can penetrate deeply inside the material, resulting in a highly resolved 3D intensity distribution. The numerical calculation result derived from the quadratic dependence of the EM field is shown in **Figure 3(a₃)**. The size of the focusing spot (full width at half maximum, FWHM) is quite large due to the use of a long wavelength. However, in practice, two photons can only be simultaneously absorbed at an intensity above the polymerization threshold. Therefore, a small effective focusing spot below the diffraction limit can be achieved with the TPA method by controlling the excitation intensity.

The case where the linear absorption is very low (LOPA) was considered. At the wavelength $\lambda = 532 \text{ nm}$, the absorption coefficient is only 723 m^{-1} , which is much smaller than that at 308 nm. Simulation results show that light can penetrate deeply inside the absorbing material without significant attenuation thanks to this very low linear absorption. As shown in **Figure 3(a₂)**, the light beam can be tightly confined at the focusing spot, which can then be moved freely inside the thick material, exactly as in the case of TPA. Furthermore, LOPA requires a shorter wavelength as compared with TPA, the focusing spot size (FWHM) is therefore smaller. The diagram depicted in **Figure 3(a₄)** shows clearly the difference of the intensity distribution along the optical axis of three excitation mechanisms. It is important to note that there is no intensity threshold in the case of LOPA, because it is a linear absorption process. Therefore, LOPA requires a precise control of light dose in order to achieve high resolution optical addressing.

The NA of OL is also an important parameter to be taken into account for LOPA case. It was demonstrated that the use of a high NA OL is a crucial condition. The intensity distributions at the focusing spot obtained with OLs of different NA values (with the same low absorption

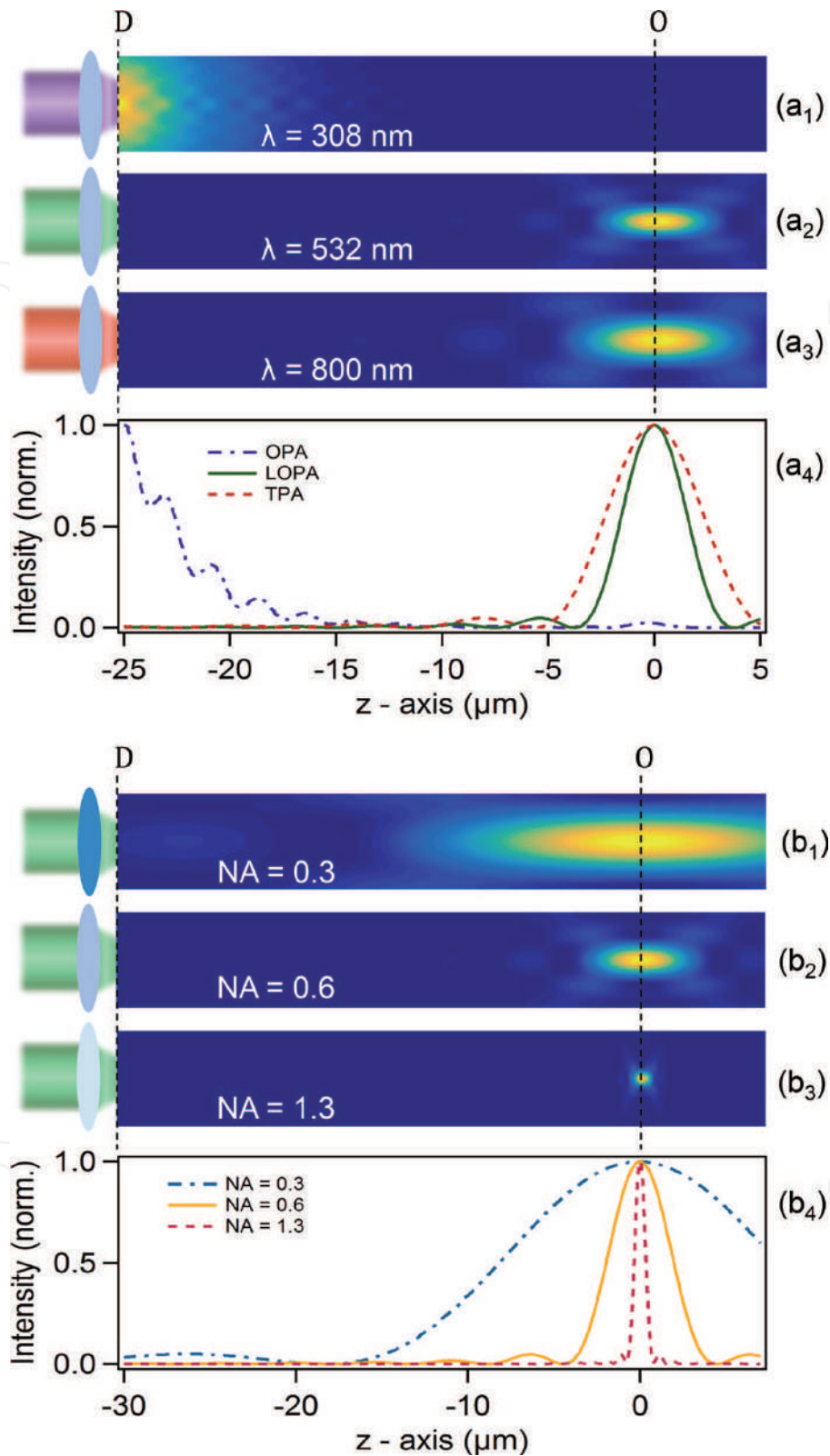


Figure 3. (a) Numerical calculations of light propagation inside SU8, by using different wavelengths, (a₁) 308 nm, (a₂) 532 nm, and (a₃) 800 nm, respectively. (a₄) Intensity distributions along z -axis of the light beams shown in (a₁₋₃). In this calculation, NA = 0.6, refractive index $n = 1.58$, and $d = 25$ μm . (b) Propagation of light ($\lambda = 532$ nm) inside SU8, with (b₁) NA = 0.3, (b₂) NA = 0.6, and (b₃) NA = 1.3, respectively, $d = 30$ μm . (b₄) Intensity distributions along z -axis of the light beams shown in (b₁₋₃).

coefficient $\sigma_2 = 723 \text{ m}^{-1}$) are shown in **Figure 3(b)**. It is clearly seen that with an OL of low NA (NA = 0.3), the light beam is not well focused, resulting in low contrast intensity distribution between the focal region and its surrounding. Therefore, the LOPA-based microscopy using a low NA OL cannot be applied for 3D optical addressing. However, in the case of tight focusing (for example, NA = 1.3), the light intensity at the focusing spot is a million time larger than that at out of focus, resulting in a highly resolved focusing spot (**Figure 3(b₃)**).

For all the above calculations, it can be concluded that the LOPA-based microscopy is promising for the realization of 3D imaging and 3D fabrication, similarly to what could be realized by TPA microscopy. By using the LOPA technique, 3D fluorescence imaging or fabrication of 3D structures can be realized by moving the focusing spot inside the material since fluorescence (for imaging) or photopolymerization (for fabrication) effects can be achieved efficiently within the focal spot volume only.

It is worth noting that in LOPA technique, the absorption exists, even if the probability is very small, the penetration depth is therefore limited to a certain level. This effect exists also in the case of TPA, but it is more important for LOPA. **Figure 4** represents the maximum intensity at the focusing spot as a function of the penetration length, d . For this calculation, the ultralow absorption coefficient of SU8 at $\lambda = 532 \text{ nm}$, $\sigma = 723 \text{ m}^{-1}$ was considered. At the distance of $390 \text{ }\mu\text{m}$, the intensity was found to decrease by half with respect to that obtained at the input of absorbing material (D interface). This penetration depth of several hundred micrometers is fully compatible with the scanning range of piezoelectric stage (typically, $100 \text{ }\mu\text{m}$ for a high resolution), or with the working distance of microscope OL (about $200 \text{ }\mu\text{m}$ for a conventional high NA OL).

In summary, in order to realize the LOPA-based microscopy, two important conditions are required: (i) ultralow absorption of the studied material at the chosen excitation wavelength, and (ii) a high NA OL for tight focusing of the excitation light beam. To experimentally demonstrate the application of LOPA in DLW, in the next chapter, SU8 will be used as the material and a CW laser at $\lambda = 532 \text{ nm}$ as the excitation source.

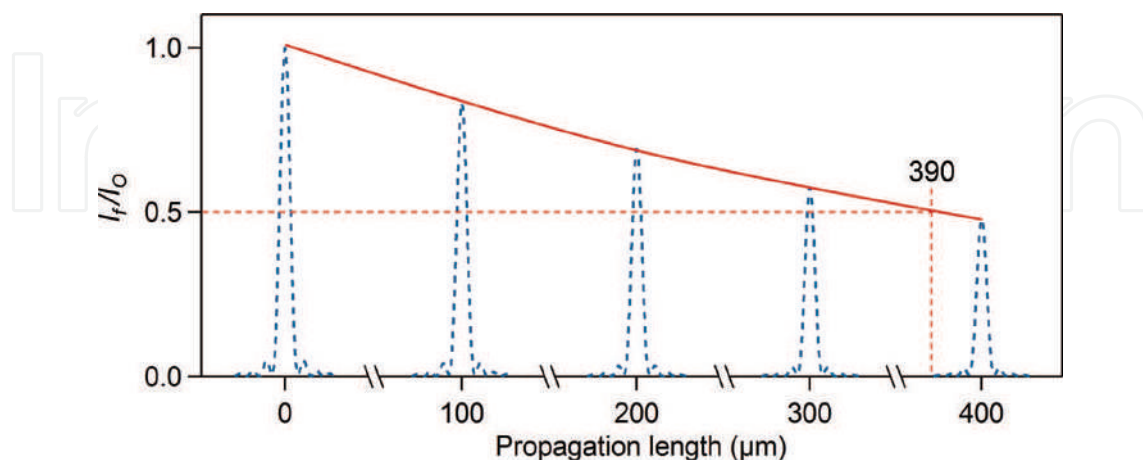


Figure 4. Red curve: normalization of intensity (I_f/I_0) at the focusing spot as a function of the propagation length. I_f and I_0 are the intensities obtained with and without absorption medium, respectively. Dot curves: zoom on intensity profiles of the focusing spot along the optical axis, calculated at different d . The results are simulated with: $\sigma = 723 \text{ m}^{-1}$; $\lambda = 532 \text{ nm}$; NA = 1.3 ($n = 1.58$).

3. Experimental demonstration of LOPA-based 3D microfabrication

3.1. Experimental setup and fabrication procedure

The LOPA technique can obviously be used for all 3D applications, including 3D imaging and 3D fabrication. As mentioned in section 2, two conditions are required: a photoresist that presents an ultralow absorption at the wavelength of the excitation laser, and a high focusing confocal laser scanning (CLSM) system. For the first condition, SU8 photoresist is an excellent candidate, thanks to its ultralow absorption in the visible range, for example at 532 nm (Figure 5(b)), which is the wavelength of a very popular and low-cost laser. By using a high NA oil-immersion OL of NA = 1.3 to focus a laser beam into the photoresist, the second condition is then satisfied.

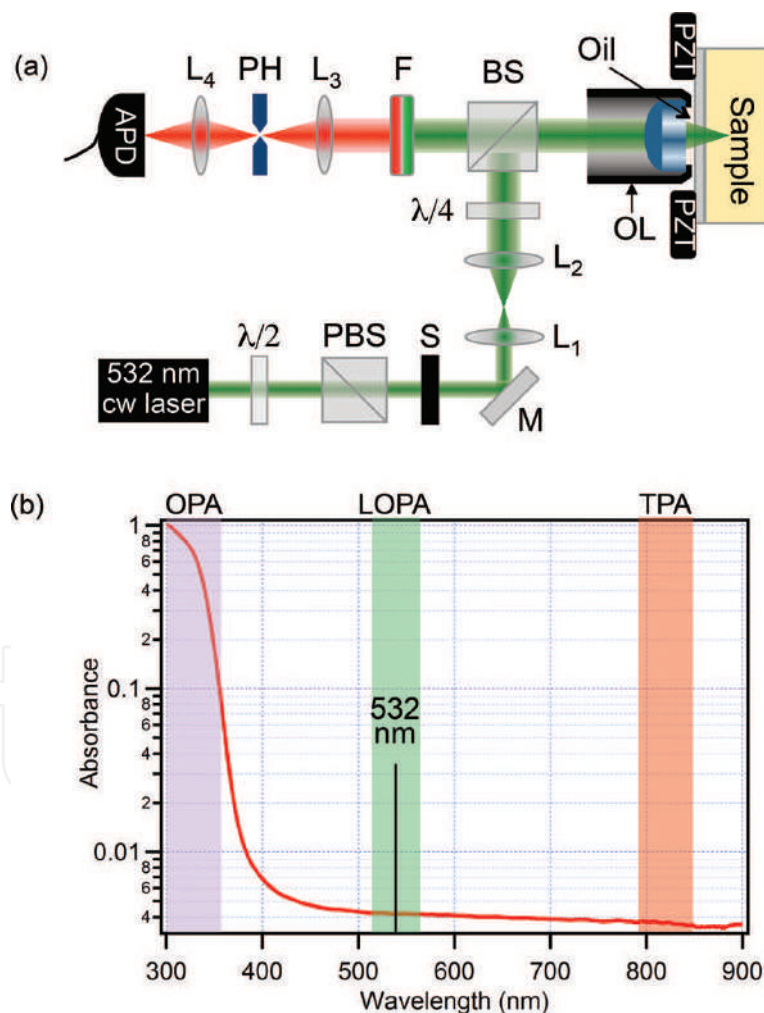


Figure 5. (a) A sketch of the experimental setup. PZT: piezoelectric translator, OL: oil immersion microscope objective, $\lambda/4$: quarter-wave plate, $\lambda/2$: half-wave plate, BS: beam splitter, PBS: polarizer beam splitter, M: mirror, S: electronic shutter, L_{1-4} : lenses, PH: pinhole, F: 580 nm long-pass filter, APD: avalanche photodiode. (b) Absorption spectrum of SU8 photoresist. The color bars indicate three cases: OPA (purple bar), LOPA (green bar), and TPA (red bar). To demonstrate LOPA DLW, a laser operating at 532 nm is used.

In order to demonstrate the LOPA DLW technique, a confocal optical system illustrated in **Figure 5(a)** was built. In this system, a CW laser operating at 532 nm is used. The laser power is monitored by a combination of a half-wave plate ($\lambda/2$) and a polarizer. The laser beam is directed and collimated by a set of lenses and mirrors. In order to realize mapping or fabrication, samples are mounted on a 3D piezoelectric actuator stage (PZT), which is controlled by a LabVIEW program. A quarter-wave plate ($\lambda/4$) placed in front of the OL is inserted and oriented to generate a circularly polarized beam for mapping and fabrication. The high NA oil-immersion objective (NA = 1.3) placed beneath the glass coverslip is used to focus the excitation laser beam. The fluorescence signal emitted by the samples is collected by the same objective, filtered by a 580 nm long-pass filter, and detected by an avalanche photodiode (APD).

For fabrication, SU8 photoresist is coated on a glass substrate. In order to remove all contamination on the surface, glass substrates must be treated with acetone and an ultra-sonication prior to the spin coating. After the cleaning process, SU8 of different viscosities (SU8 2000.5, SU8 2005, or SU8 2025) is spin coated on the glass substrates, depending on the types of the desired structure. For 1D and 2D structures, SU8 2000.5 and 2002, which give a layer thickness of 0.5 and 2 μm , are used. For 3D structures, other types of SU8 at higher viscosity, for example SU8 2005 or 2025, are required. The spin coating step is followed by a soft baking step at 65°C and 95°C, the soft baking time depends on the types of SU8 used.

Before writing the structure on the photoresist, the interface between the glass substrate and the photoresist layer must be determined. To determine the interface, the focusing spot is scanned along xz or yz plane at very low laser power to prevent polymerization, and the fluorescence signal can be collected by the APD. This step allows one to precisely write the structure at the desired position. Then the laser power is increased to several mW to fabricate any desired structures by scanning the focusing spot along a path programmed with Labview. Post exposure bake (PEB) is carried out after the fabrication, and followed by a development step.

3.2. Verification of LOPA-based fabrication

It has been demonstrated, by analyzing fluorescence emission, that the SU8 photoresist linearly absorbs the excitation laser at 532 nm-wavelength [17]. For the LOPA CLSM, the intensity at the focusing region (of the order of 10^7 W/cm^2) is much higher than that at the input of the optical system (10^{-2} W/cm^2), allowing the excitation and fluorescence detection of the focal spot volume only. The fluorescence measurements in which the emission is quite low are enabled by the use of an avalanche photodiode (APD).

By using the standard fabrication process described in the previous part, it was demonstrated that polymerization is achieved only at the focusing spot of the microscope objective, where the excitation intensity is sufficiently high to compensate the low linear absorption of the resist. In the case of TPA, there are two thresholds: the first one related to light intensity, above which two photons are simultaneously absorbed, and the second one related to dose, above which complete photopolymerization is achieved. However, in the case of LOPA, there exists only one threshold related to dose. Thanks to a high intensity at the focusing spot, the complete photopolymerization is only achieved in this region. **Figure 6** shows SEM images of experimental results. For each exposure, a solid structure, called “voxel,” corresponding to

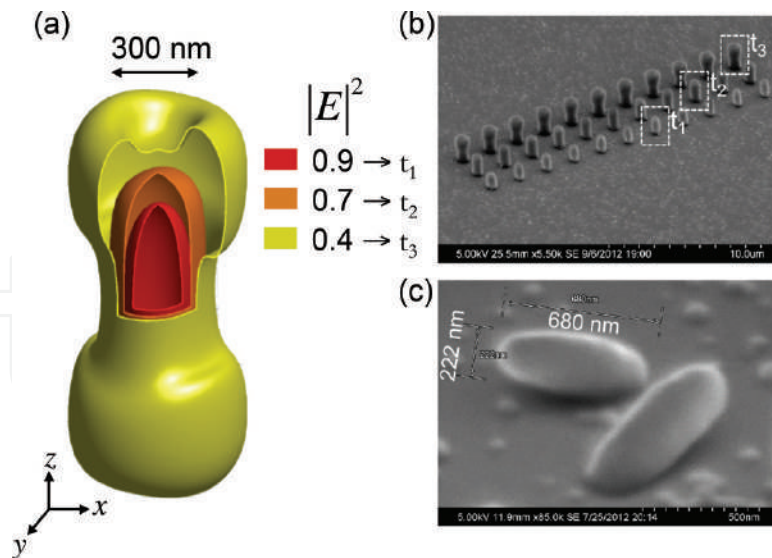


Figure 6. Fabrication of voxels by single-shot exposure. (a) Theoretical calculation of the contour plot of light intensity at the focusing region ($NA = 1.3$, $n = 1.518$, $\lambda = 532$ nm). (b) SEM image of a voxels array obtained by different exposure doses. Three ranges of voxels are fabricated correspondingly to the exposure time t_1 , t_2 and t_3 whose corresponding doses are 0.9, 0.7 and 0.4 as indicated in (a). These experimental results explain the OPA nature where the formed voxel shape is determined by the exposure dose. (c) Complete voxel lying on the substrate indicated an ellipsoidal form (exposure time t_1 was applied). This form is similar to that obtained by the TPA method.

a focusing spot, was obtained. By changing either the excitation power or the exposure time, i.e. the dose, the voxel size and shape can be adjusted, as shown in **Figure 6(b)**. A CW green laser power of only 2.5 mW and an exposure time of about 1 second per voxel were required to create these structures. **Figure 6(b)** shows, for example, a voxel array realized with three different exposure times. The dose dependence can be explained theoretically by calculating the iso-intensity of the focusing spot at different levels. Three kinds of voxels obtained with t_1 , t_2 and t_3 in **Figure 6(b)** correspond to three different iso-intensities illustrated in **Figure 6(a)**, namely 0.9, 0.7 and 0.4, respectively. The operation in the OPA regime is fully confirmed by the evolution of voxel size and shape observed experimentally. Indeed, in the case of TPA, the creation of bone-like voxel shape requires very high excitation intensity and could not be easily realized due to the TPA intensity threshold. In the case of LOPA, all these voxels shapes were obtained by simply adjusting the exposure time while the laser power is kept at a low value. Smaller voxels as shown in **Figure 6(c)** require shorter exposure times. Certainly, the exposure time required to create sub-micrometer structures varies as a function of the laser power.

Pillar arrays were also fabricated by scanning the focusing spot of the laser along the thickness of a 1 μm SU8 film with different writing speeds. **Figure 7** shows the pillar size as a function of writing velocity for three values of laser power, $P = 7.5$, 6, and 4.5 mW. The fabrication of smaller pillars down to 190 nm is possible [17]. The size of individual pillars is quite small when considering the wavelength (532 nm) used for the writing process. As for the linear dependence with intensity (OPA vs. TPA) [20, 21], the diameter-dose relationship agreement confirms this behavior, as the intensity I_0 is used for the fit, instead of I_0^2 in the case of TPA. This result confirms the fabrication of sub-microstructures by LOPA-based DLW method.

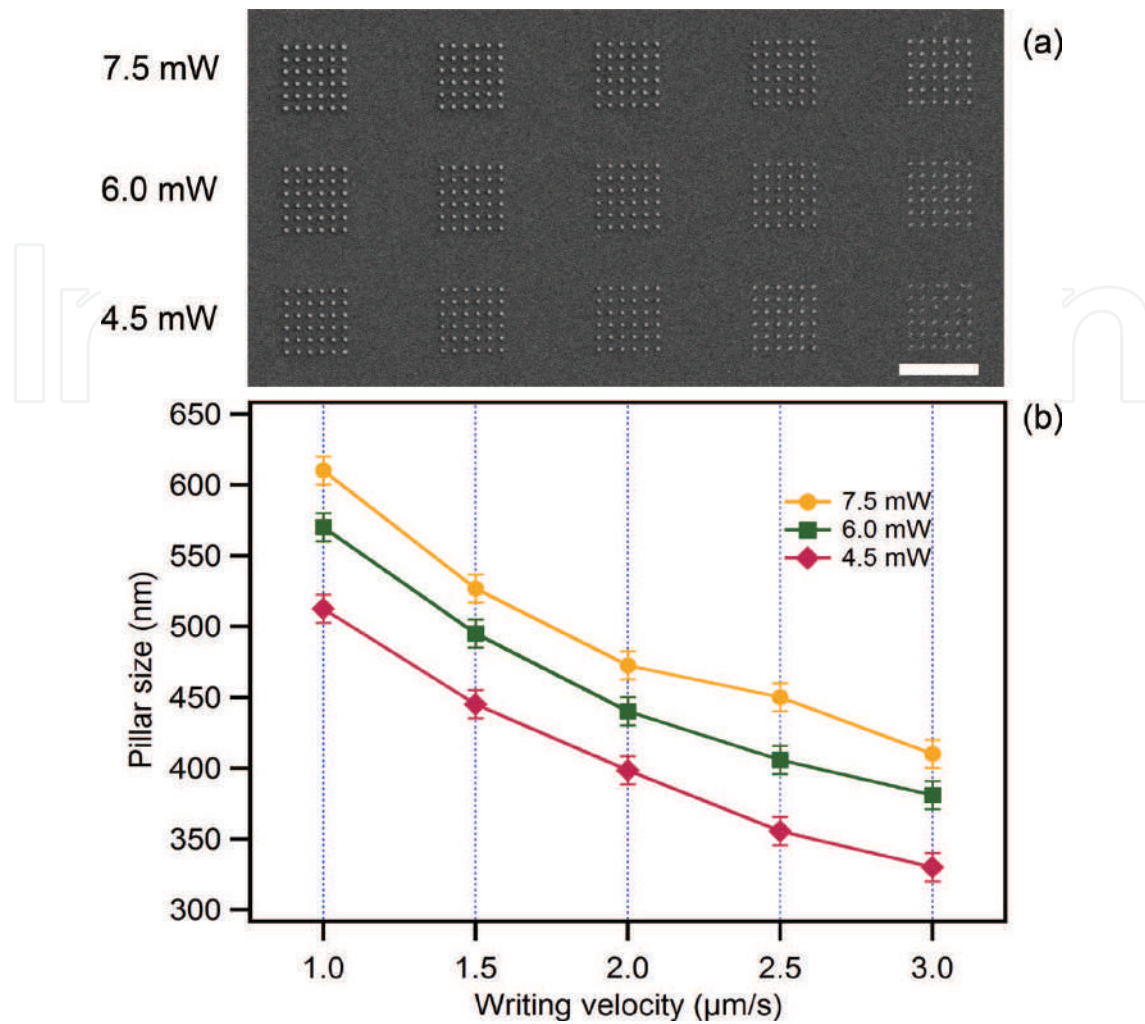


Figure 7. (a) SEM image of a pillar arrays fabricated at different writing velocity and laser powers. (b) Dose dependence of size of pillars shown in (a), with different laser power values, $P=7.5, 6, 4.5$ mW, and different writing velocities, $v=1.0, 1.5, 2.0, 2.5,$ and 3.0 $\mu\text{m/s}$. Scale bar: 10 μm .

3.3. LOPA-based DLW for 3D microstructure fabrication

In order to demonstrate 3D fabrication, 3D arbitrary photonic crystals (PCs) have been realized. In the fabrication process, the dose was adjusted by changing the velocity of the PZT movement while the input power is fixed. The doses were varied from structure to structure depending on the size and separation (periodicity of PC). In the first experiment, a series of different size 3D woodpile PC structure on glass substrate was fabricated. It is noted that, SU-8 exhibits a strong shrinkage effect, which results in the distortion of the fabricated structure. After a number of experiments, acceptable parameters for woodpile, which are an input power of 2.5 mW and a velocity of 1.4 $\mu\text{m/s}$, were found. Applying these parameters, 3D diamond lattice-like-based PC structures such as woodpile, twisted chiral and circular spiral can be realized.

Figure 8(a–f) shows SEM images of 3D woodpile, spiral and chiral PCs fabricated with these optimum fabrication parameters. The woodpile structure (**Figure 8(a and b)**) consists

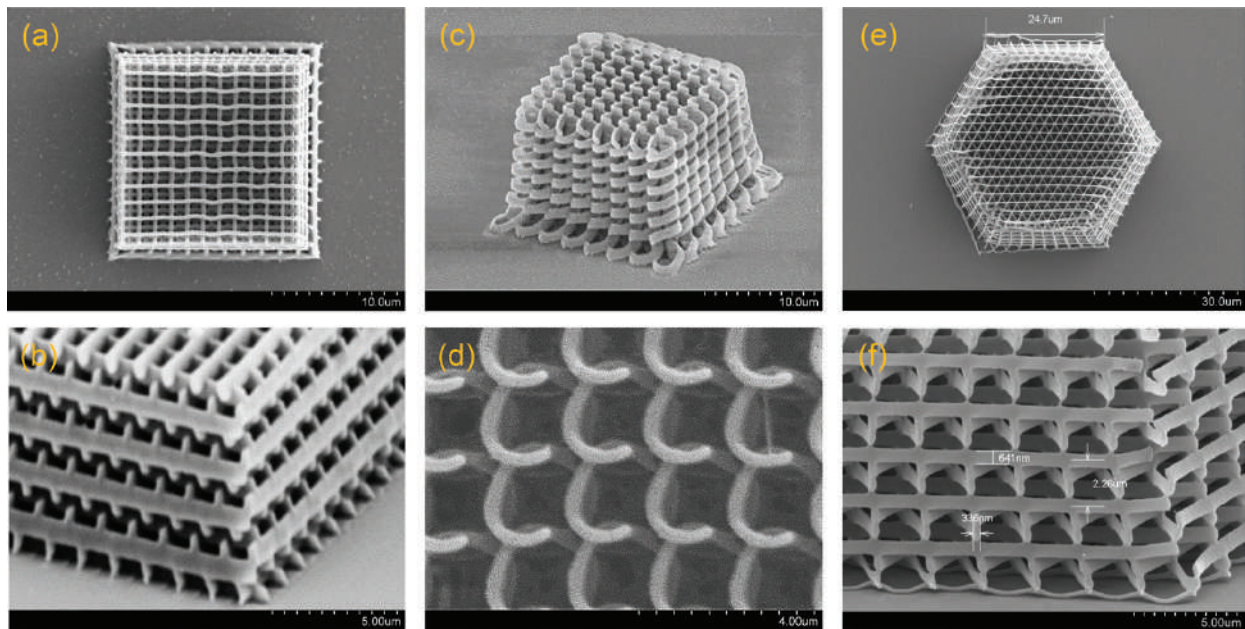


Figure 8. (a–b) SEM images of a woodpile structure fabricated with the following parameters: distance between rods = 1.5 μm ; distance between layers = 0.7 μm ; number of layers = 20; laser power $P = 2.5$ mW and scanning speed $v = 1.4$ $\mu\text{m}/\text{s}$. (c and d) SEM images of a chiral structure. Structure and fabrication parameters: distance between rods $a = 2$ μm ; distance between layers $c/3 = 0.75$ μm ; number of layers = 28; line width $r = 300$ nm; laser power $P = 2.8$ mW and scanning speed $v = 1.34$ $\mu\text{m}/\text{s}$. (e–f) SEM images of a spiral structure (shown in inset). Fabrication parameters: diameter of a spiral $D = 2$ μm ; spiral pitch $C = 2$ μm ; lattice constant $a = 3$ μm ; spiral height equals to film thickness = 15 μm ; laser power $P = 2.6$ mW and scanning speed $v = 1.34$ $\mu\text{m}/\text{s}$.

of stacked 20 layers. Each layers consists of parallel rods with period $a = 1.5$ μm . Rods in successive layers are rotated by an angle of 90° relative to each other. Second nearest-neighbor layers are displaced by $a/2$ relative to each other. Four layers form a lattice constant $c = 2.1$ μm . SEM measurement shows that the line width of rods on the top layer is about 320 nm, which is 1.5 times of the voxel standard size. This means that the size of the rod can be minimized further. Woodpile structure with measured separation between rods on the top layer of only 800 nm and the measured line width of 180 nm was also successfully fabricated. This result shows evidently that separation of rods and layers are comparable to the wavelength of visible light. **Figure 8(c–f)** shows, as examples, two other kinds of sub-micrometer 3D structures. Clearly, 3D chiral or spiral structures are well created, which are as good as those obtained by TPA DLW. The structures features are well separated, layer by layer, in horizontal and in vertical directions. The feature sizes are about 300 nm (horizontal) and 650 nm (vertical).

Experimental realization of LOPA-DLW in fabrication of 1D, 2D and 3D photonic crystal showed evidently the advantage of LOPA idea in combining with regular DLW. With a few milliwatts of a CW laser and in a moderate time, any kind of sub-micrometer structure with or without designed defect could be fabricated. However, some fabricated structures are not uniform or distorted. The physical causes of the distortion can be attributed to two main effects: dose accumulation effect [22] and shrinkage effects [23]. In the next section, some techniques to overcome those effects will be experimentally demonstrated.

4. Optimization of LOPA-based DLW technique

4.1. Dose accumulation effect

As a consequence of linear behavior of absorption mechanism, the dose accumulation effect is the inherent nature of linear absorption material [24, 25]. In contrast to a conventional TPA method, a photoresist operated in OPA regime does not have any threshold of polymerization [26], hence the voxel size can be controlled by adjusting the exposure dose. In principle, polymerization occurs at the focusing spot with a single-shot exposure resulting in a very small voxel (smaller than the diffraction limit) [27]. However, when two voxels are built side-by-side with a distance of about several hundred nanometers, two resulting voxels are no longer separated [17]. This issue evidently originates from the dose accumulation effect in OPA process.

Similar to OPA microscopy where the microscopy image cannot resolve two small objects which localize at about several hundred nanometers from each other, the fabricated voxels in DLW also cannot be separated. Abbe's criterion states that, the minimum resolving distance of two objects is defined as $0.61\lambda/\text{NA}$, where λ is the wavelength of incident light. This diffraction barrier thus imposes the minimum distance between different voxels, created by different exposures. Moreover, when multiple exposures are applied, although isolated voxel fabrication is ideally confined to the focal volumetric spot, the superposition of many out-of-focus regions of densely-spaced voxels leads to undesired and unconfined reaction. This results in the larger effective voxel size, even with a distance far from the diffraction limit. Indeed, in the case of OPA, photons could be absorbed anywhere they are, with an efficiency depending on the linear absorption cross-section of the irradiated material. The absorbed energy is gradually accumulated as a function of exposure time.

Figure 9 shows the theoretical calculations and experimental results of the dependence of the voxels size on distance. When two voxels are separated by a distance shorter than $1\ \mu\text{m}$, a clear accumulation effect is observed, resulting in a voxel of larger size. When the separation changes from 2 to $0.5\ \mu\text{m}$, the FWHM of each voxel is increased from 190 to $300\ \text{nm}$. Moreover, for a short separation, the voxels array is not uniform from the center to the edge part, as can be seen in case of a separation of $0.5\ \mu\text{m}$. In the parts below, two strategies to get rid of this accumulation effect are discussed.

4.1.1. Dose compensation strategy

According to the structures fabricated by LOPA DLW and the theoretical calculation, the dose accumulation effect should be compensated in order to get superior structure uniformity. The compensation technique idea is based on a balance of the exposure doses over the structure. In other words, a certain amount of the exposure dose should be reduced at the region (or a part or a division) where the dose accumulation effect strongly occurs and should be added to the region where the dose is lacking.

As demonstrated above, the accumulation effect depends on the separation distance, s . 2D micropillars array was fabricated by scanning the focusing spot along the z -axis to demonstrate

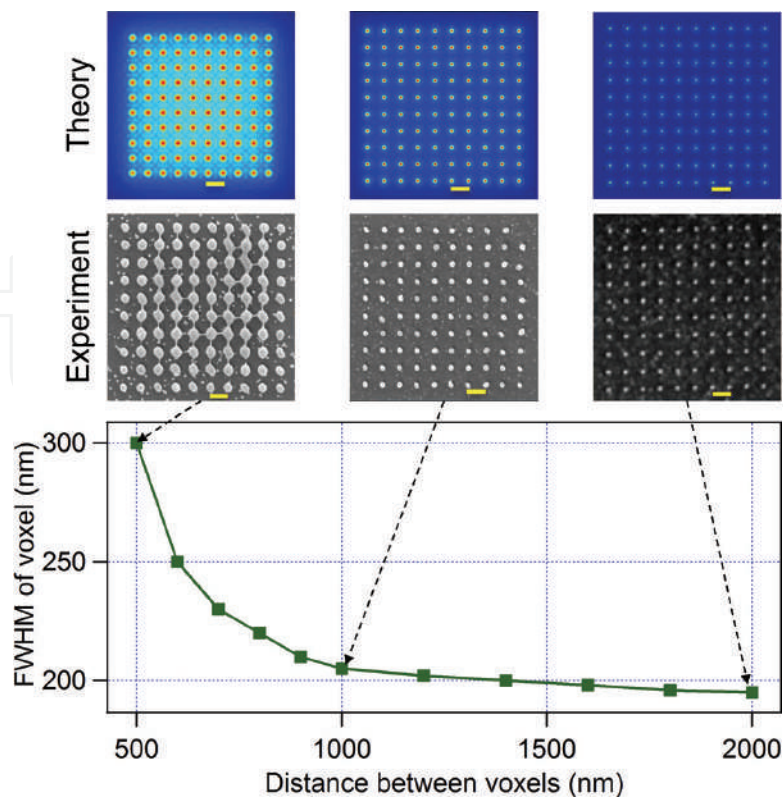


Figure 9. Dependence of voxel sizes on separation between voxels calculated at the iso-intensity = 0.5 ($I = I_0/2$), showing the influence of energy accumulation from one focusing spot to another. Insets show simulated images (blue background) and SEM images (gray background) of 2D voxel arrays fabricated with different distances between two voxels: 2, 1, and 0.5 μm . Scale bar (from left to right): 0.5, 1, and 2 μm .

the accumulation effect and the dose compensation technique. The variation of the pillars size as a function of s distance, from 0.3 to 3 μm , has been systematically investigated [22]. According to the pillars size variation, from the center to the edge of the structure, the size difference could be compensated by gradually increasing the exposure doses for outer pillars. The intensity distribution of a pillar array and the dose compensation strategy are shown in **Figure 10(a)**. Different dose compensation ratios have been experimentally applied, indicated by letters A, B, C, and D. Two sets of structures have been fabricated on the same sample in order to maintain the same experimental conditions: one without and the other with dose compensation. The accumulation effect in the case of $s = 0.4 \mu\text{m}$, obtained without compensation, is shown in **Figure 10(b)**. It can be seen that the structure is not uniform, and the outmost voxels collapse into central pillars. With dose compensation, i.e. the doses for outer pillars are increased, 2D micropillars arrays become uniform. Structures realized with different dose ratios, corresponding to A, B, C, and D schemes depicted in **Figure 10(a)**, are shown in **Figure 10(c–f)**. With high dose compensation amplitude, the size of outer pillars becomes even larger than those in the center. By using an appropriate dose compensation ratio, perfectly uniform 2D micropillars array is obtained, as shown in **Figure 10(c)**. The structure period is only 400 nm, the height of pillars is about 700 nm, and pillar's diameter is about 160 nm. Structures with periods of several hundred nanometers are very suitable for photonic applications in visible range.

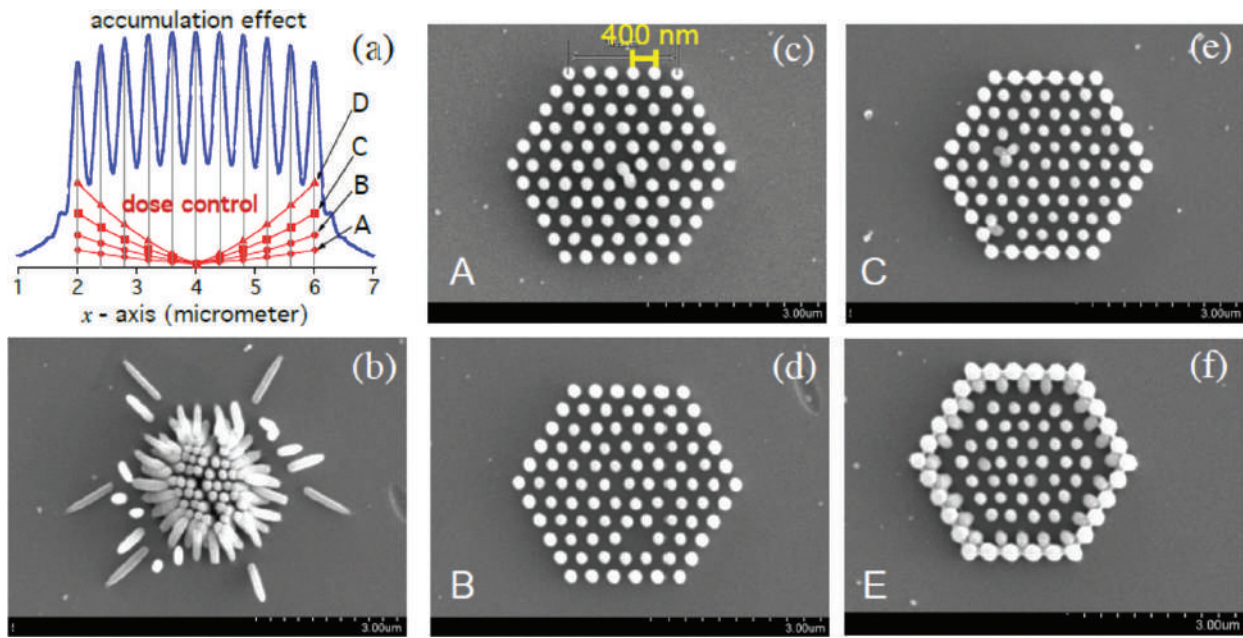


Figure 10. Compensation of dose accumulation for $s = 0.4 \mu\text{m}$. (a) Theoretical calculation of the intensity distribution as a function of x -position (blue color), and proposition of different doses, indicated by A, B, C, and D (red color) to compensate the dose accumulation effect. (b–f) SEM images of 2D hexagonal structures realized without compensation (b), and with compensation with different doses: A (c); B (d); C (e), and D (f). The excitation power was fixed at 2.5 mW and the dose was adjusted by changing the writing velocity.

4.1.2. Local PEB for small and uniform microstructures

The dose compensation techniques are presented above and proved to be able to compensate the size difference in the structures. Nonetheless, this technique requires numerous calculations and tests in order to find out the appropriate dose compensation parameters. For example, for the fabrication of other 2D structures with a sub-micrometer period containing an arbitrary defect, such as a microcavity or a waveguide of arbitrary shape, the dose should be controlled for individual voxel (or pillar) as a function of its position in the structure and with respect to the defect. This requires many attempts to find out the optimized parameters since the dose compensation is different for different structures.

In this part, the thermal effect induced by a CW green laser in the LOPA-based DLW technique has been investigated, which plays a role as a heat assistant for completing the crosslinking process of the photopolymerization of SU8 [28]. The fabrication of sub-microstructures using LOPA DLW with a laser-induced thermal effect, also called local PEB, was demonstrated, and it was also shown to alter the traditional PEB on a hot plate and help overcome the accumulation effect existing in standard LOPA DLW.

For the demonstration of local PEB, two sets of 2D structures were fabricated, each set contains pillar arrays written at different doses (by varying the laser power and the writing speed). One set was realized following the traditional process, i.e., after exposure, the sample was post-baked for 1 min at 65°C and then 3 min at 95°C using a hot plate. For the other set, the PEB step was skipped, which means that the exposure process was followed directly by the

development process. It has been observed that for the same dose, the pillars fabricated without PEB are smaller than those fabricated with PEB [28]. Due to the fact that the structures are not formed at low power (low light intensity), it is assumed that the applied laser power or intensity must be above a threshold in order to induce enough heat for the crosslinking process, and this threshold should be higher than that of standard LOPA (with PEB) for a complete photopolymerization.

Figure 11(a) shows the accumulation effect observed in the structures fabricated using traditional PEB process at different doses. The distance between two pillars is 500 nm, which is considered as a sufficiently short separation to induce noticeable accumulation effect. It can be observed that the pillar size decreases from the center to the edge, with a variation of 10–20%, resulting in non-uniform structures. **Figure 11(b)** shows the SEM images of structures obtained using local PEB. In this case, in order to induce sufficiently high temperature, the laser power (5 mW) was higher than that (3 mW) used with traditional PEB step. In contrast to the structures fabricated using traditional PEB, which shows accumulation effect (**Figure 11(a)** on the top), the structures obtained with local PEB show nearly perfect uniformity (**Figure 11(b)** on the top). Moreover, as compared to the dose compensation method, the LOPA-based DLW using local PEB does not require testing, since the dose applied is constant for all voxels and the range of applicable doses is large. In addition, the PEB step is skipped, which is a great advantage in terms of fabrication time. Furthermore, comparing to structures realized by TPA-based DLW, the period of these fabricated structures is much shorter (only 500 nm or even 400 nm) thanks to the use of short laser wavelength, which can be an additional advantage of this LOPA technique.

The heat equation [29] was also solved using finite element model realized by Matlab to demonstrate that the heat induced by high excitation intensity of a 532 nm CW laser confines the crosslinking reaction in the local region where the temperature is higher than the PEB temperature. This resulted in fine and uniform structures, since only the material within the effective temperature region was properly polymerized. Temperature-depth dependence calculation shows that this technique allows the fabrication of uniform 3D sub-micro structures with large thickness. This is then evident by an experimental demonstration of fabrication of a uniform 3D woodpile structure without PEB step, with a period as small as 400 nm [28]. Compared to the commonly used TPA method, LOPA-based DLW with local PEB shows numerous advantages such as simple, low-cost setup and simplified fabrication process, while producing same high-quality structures.

4.2. Shrinkage effect

Shrinkage is a fundamental issue for photopolymerization in the photopolymer. It is difficult to avoid the non-uniformity when the conventional polymerized microstructures are attached to substrates. The origin of this effect for TPA polymerization has been investigated [30]. It was suggested that the origin of the shrinkage is the collapse of this material during the development stage owing to the polymer not being fully cross-linked when they are made at the irradiation power close to the photopolymerization threshold. At fabrication intensities slightly above the photopolymerization threshold, the photopolymerization yield is not

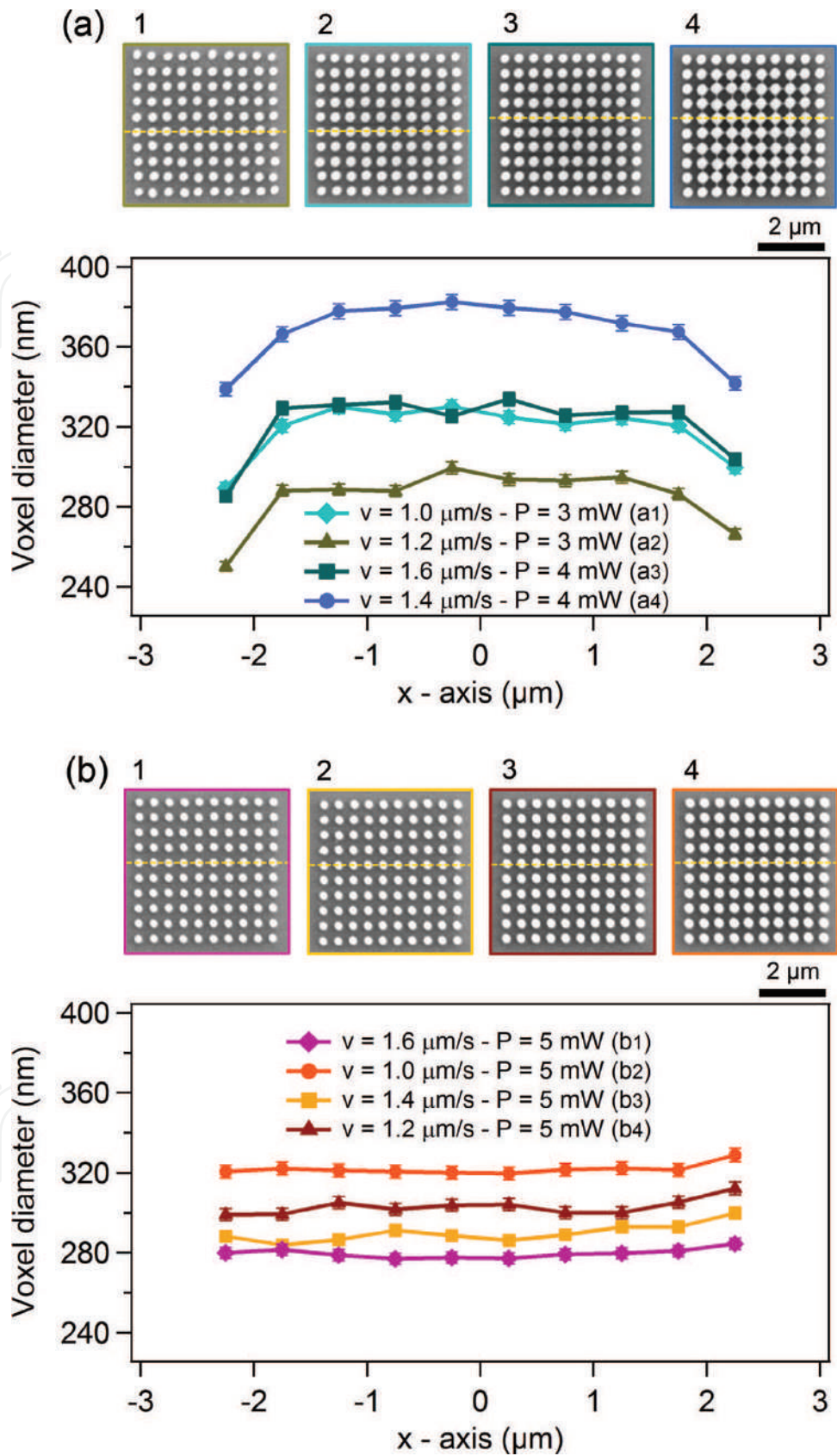


Figure 11. Comparison between structures fabricated with standard PEB (a) and local PEB (b) shows the advantage of “local PEB” in overcoming the accumulation effect. Left: SEM images of fabricated structures. Top: sizes of pillars indicated by the dashed line on SEM images plotted as a function of position. With standard PEB: the pillars are larger at center of pattern. With local PEB: pillars are very uniform. All structures are fabricated with a period of 500 nm.

100%, resulting in a sponge-like material after the development process. Hence, the structural shrinkage observed at average laser powers is the result of the collapse of this material at a molecular level [30]. However, it has also been confirmed that, although the sponge-like materials are formed during the development because of the non-full polymerization at low laser power, the shrinkage indeed occurs due to the capillary forces and the dramatic change of surface tension during the drying process [31].

For LOPA 3D fabrication, this shrinkage effect is also observed, with different levels of distortion for different exposure doses, i.e., the lower the exposure dose is the higher the shrinkage is. (Figure 12a–d) shows the shrinkage effect observed in 3D woodpile structures fabricated at different doses ($P = 9$ mW, writing speed $v = 4, 3, 2,$ and 1 $\mu\text{m/s}$, from left to right, respectively). It can be clearly seen that the degree of shrinkage at different exposure doses is different, i.e., from left to right, the writing speed decreases (the dose increases), the shrinkage decreases. This result is also in agreement with previous report on the shrinkage in the case of TPA polymerization [30], which suggests that in both cases, the shrinkage effect might have a similar origin.

Non-uniform shrinkage might destroy the structural periodicity of a photonic crystal, resulting in the degradation of its optical quality. While shrinkage is an intrinsic problem, which cannot be avoided, non-uniform shrinkage problem can be positively resolved. Several approaches have been reported on how to overcome this non-uniform shrinkage, including pre-compensation for deformation [32], single [33] and multi-anchor supporting method [30, 34], or freestanding microstructures trapped in cages [35]. All the above methods are investigated for the TPA case. In this work, the multi-anchor supporting method was employed to reduce the deformation caused by the non-uniform shrinkage of 3D microstructures by LOPA DLW. To demonstrate this idea, instead of fabricating woodpile structures directly on glass substrate, four “legs” at four corners of structures were created in order to avoid the attachment of the structures to the glass substrate, which is the direct cause of the non-uniform

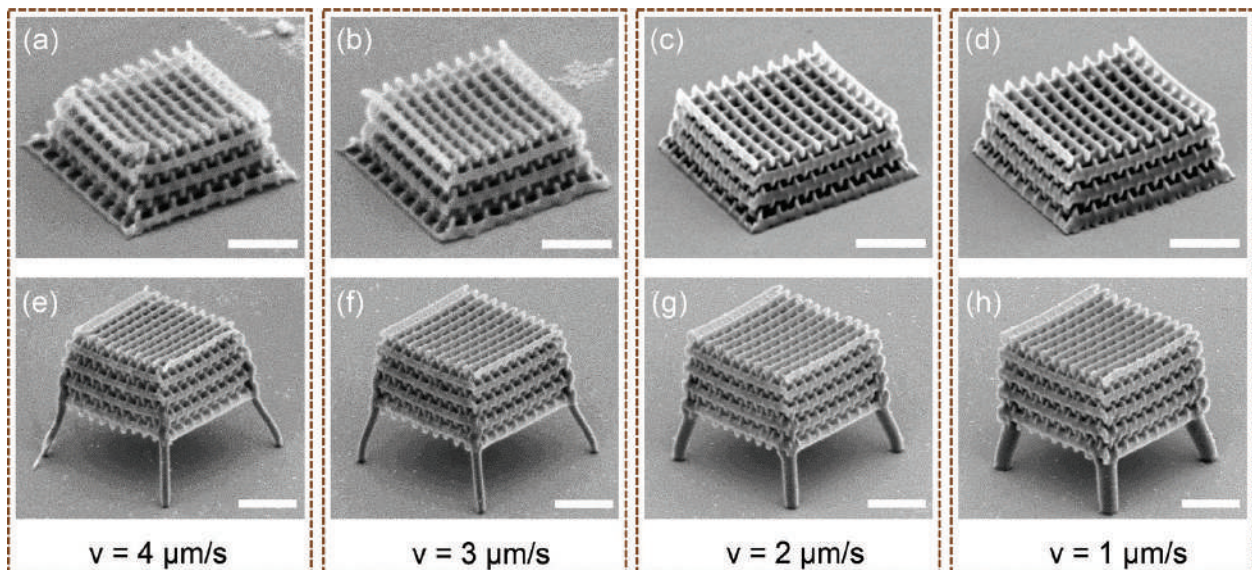


Figure 12. 3D woodpile structures (number of layers =16, rod spacing = 1.5 μm and layer spacing = 0.65 μm) fabricated without (a–d) and with “legs” (e–h), at laser power of 9 mW and different writing speeds: $v = 4, 3, 2,$ and 1 $\mu\text{m/s}$, from left to right. Scale bars: 5 μm .

shrinkage. These anchors were designed and fabricated as rods of several hundred nanometers and did not affect the main structure. (**Figure 12e–h**) shows woodpile structures with anchors fabricated at different doses. It can be seen that at low dose, the non-uniform shrinkage still remains as shown in **Figure 12(e)**. However, when the dose is increased by a small amount, the distortion decreases and disappears. In this case, a laser power of 9 mW and a writing speed of 3 $\mu\text{m/s}$ were sufficient for a considerable uniform structure. Compared to the non-anchored structures, the fabrication speed is reduced by three times to obtain a nearly deformation-free PC, which is remarkable especially for the fabrication of large structures. The shrinkage effect can also be exploited to produce PCs with small lattice constant.

To conclude, the multi-anchor supporting method was successfully applied to reduce the non-uniform deformation of 3D microstructure caused by attachment to the substrate. Since the support with four anchors allows uniform shrinkage of a polymeric microstructure by releasing it from the substrate, the fabricated microstructure shrinks isotropically. The combination of LOPA with local PEB and this supporting method is a promising way of producing small lattice constant photonic structures, which possess a photonic bandgap in the visible range.

5. Realization of magneto-photonic microstructures by LOPA-based DLW

LOPA-based DLW has been demonstrated to be not only applicable for SU8 but also other materials [36, 37], and be capable of fabricating structures incorporated with nanoparticles (NPs), such as plasmonic [38] or magnetic NPs [39]. In this section, as a proof of the versatility of LOPA DLW, the fabrication of 2D and 3D sub-microstructures from nanocomposite consisting of magnetite (Fe_3O_4) NPs and a commercial SU8 photoresist by employing LOPA DLW technique is presented [39]. The nanocomposite was synthesized by incorporating magnetic nanoparticles (MNPs) into SU8 matrix. Due to the magnetic force (mainly inter-particle interactions), MNPs tend to form large agglomerations, causing difficulties in achieving a homogeneous distribution of MNPs in polymer matrix. Hence, different concentrations of Fe_3O_4 MNPs and various types of SU8 with different viscosities have been investigated to obtain the best dispersion of MNPs in the polymer environment. Finally, the best compromise was achieved between SU8 2005, with moderate viscosity, and a MNP concentration of 2 wt%, which is low enough to achieve a homogeneous nanocomposite and high enough to give strong response to external magnetic field.

Arbitrary magnetic structures from magneto-polymer nanocomposite have been realized using LOPA DLW. **Figure 13(a)** shows an SEM image of an arbitrary 2D structure, the letter "LPQM," fabricated at the power of 15 mW with a writing speed of 3 $\mu\text{m/s}$. For this fabrication, a point matrix technique was used to shape the letter. The distance between pillars was set at 150 nm, which resulted in a continuous line due to the accumulation of exposure energy at the vicinity of each point. An SEM image of a 2D pillar array magneto-photonic structure, with a period of 1.5 μm is shown in **Figure 13(b)**. This structure was fabricated at

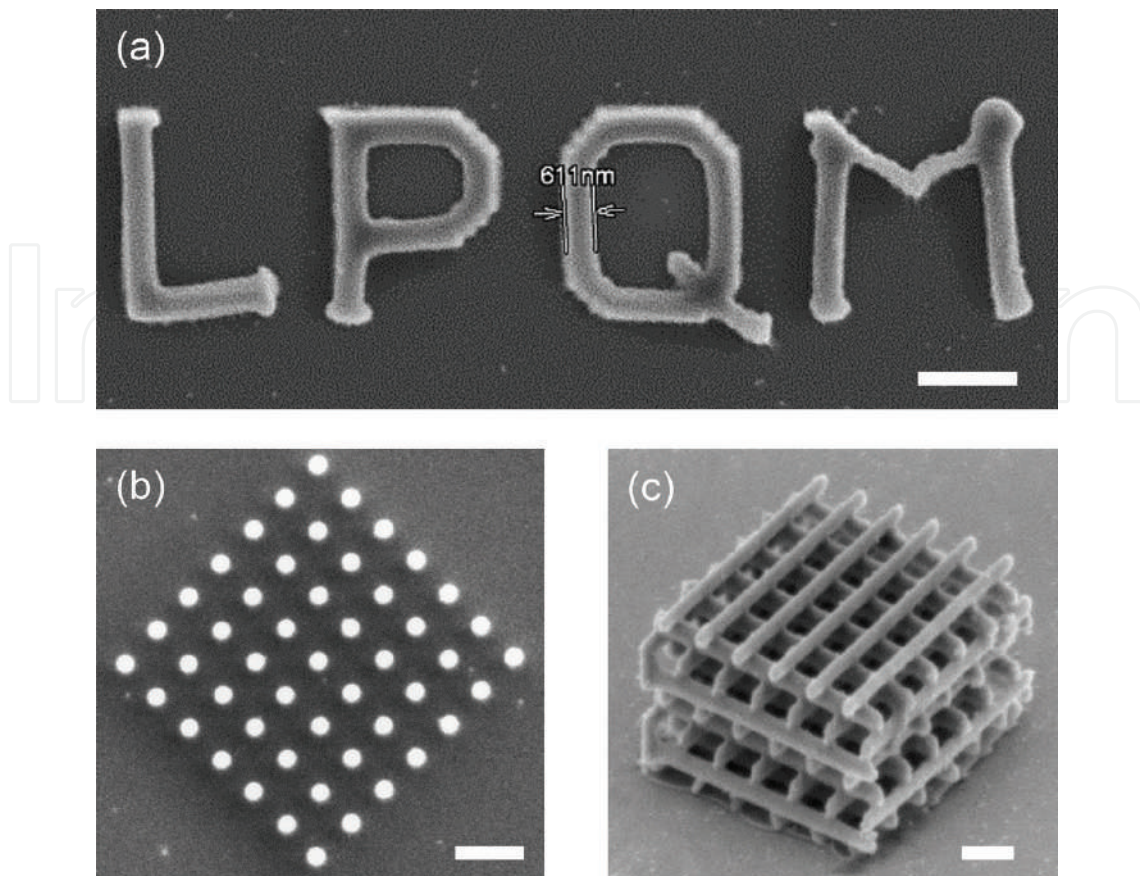


Figure 13. (a) SEM image of letter LPQM, fabricated at a laser power $P = 15$ mW, writing speed $v = 3$ $\mu\text{m/s}$. (b) SEM image of a 2D pillar array, fabricated at $P = 12$ mW, $v = 2$ $\mu\text{m/s}$. (c) SEM image of a 3D woodpile PC. Fabrication parameters: rod spacing = 2 μm ; distance between layers = 1 μm ; number of layers = 10; laser power $P = 12$ mW and scanning speed $v = 2$ $\mu\text{m/s}$. Scale bars: 2 μm .

a laser power of 12 mW and a writing speed of 2 $\mu\text{m/s}$. Similarly, various 3D structures have also been realized, with a laser power of about 12 mW. **Figure 13(c)** shows an SEM image of a woodpile structure, which consists of 10 alternating layers separated from each other by 1 μm . The rod spacing in x - and y -directions is 2 μm . These experimental results confirm that the LOPA-based DLW allows the fabrication of any magneto-photonic sub-micrometer structure or device on this magneto-polymer nanocomposite, which is very promising for a wide range of applications using magnetic microdevices and micro-robotic tools.

Indeed, magneto-photonic structures for remote actuation have attracted a great deal of attention recently [40]. With the aid of an external magnetic field, the displacement in three dimensions of magnetic structures can be controlled as desired. As shown previously, small magneto-photonic structures, which are adaptable to small targets, have been created. In order to prove the response of magnetic structures to a magnetic field, arrays of micro-pillars were fabricated as an example for demonstration [39]. To release the structures from the substrate, before coating the nanocomposite layer, an extra sacrificial layer of PMMA, which can be dissolved with acetone to release the structures into solution, was added. A magnetic field

(only 8 mT) generated by a permanent magnet was then applied to examine the magnetic field response of the magnetic micro-swimmers. The whole process from structural development to the movement toward higher gradient of the external magnetic field was observed via optical microscope, in which all of the micro-pillars quickly moved toward the magnetic tip, confirming the presence of Fe_3O_4 MNPs inside the structures and their strong response to the applied magnetic field. The magnetic structures responded strongly to the external magnetic field, opening many promising applications, such as tunable photonic structures based on magneto-optical effect and development of microrobotic tools for transport in biological systems.

6. Conclusions and prospects

In this chapter, a new technique based on an already-well-known mechanism, one-photon absorption (OPA) direct laser writing (DLW), for fabrication of low-cost, high-quality 3D PCs was introduced. This technique was demonstrated through both theory and experiment on the ultra-low absorption regime (LOPA) of photosensitive material. It was pointed out that DLW based on LOPA microscopy enables 3D fabrication in any kind of photoresist material with flexible defect engineering.

Some additional methods, such as dose compensation and local PEB, have been also proposed and applied to optimize the structures fabricated by LOPA DLW. In particular, by using the optically induced thermal effect, the fabrication of accumulation-free sub-micrometer and uniform polymeric 2D and 3D structures was realized. Also, the multi-anchor supporting method was employed to reduce the deformation caused by the non-uniform shrinkage of 3D polymeric microstructures.

As a proof of the versatility of the LOPA-based DLW technique, the capability to fabricate magneto-photonic microstructures using a $\text{SU8}/\text{Fe}_3\text{O}_4$ nanocomposite has been demonstrated. The fabricated micro-swimmers showed strong response to an applied external magnetic field, which emphasizes the importance of free-floating structures as a robotic technology for magnetic devices such as sensors, actuators, magnetic labeling, and drug targeting. 3D magneto-photonic structures have also been successfully fabricated, potentially aiding the development of magnetic nanodevices and micro-robotic tools for a wide range of applications.

Author details

Dam Thuy Trang Nguyen, Mai Trang Do, Qinggle Li, Quang Cong Tong, Thi Huong Au and Ngoc Diep Lai*

*Address all correspondence to: nlai@lpqm.ens-cachan.fr

Laboratoire de Photonique et Moléculaire, Ecole Normale Supérieure de Cachan, CentraleSupélec, CNRS, Université Paris-Saclay, Cachan, France

References

- [1] Lin SY, Fleming JG, Hetherington DL, Smith BK, Biswas R, Ho KM, et al. A three-dimensional photonic crystal operating at infrared wavelengths. *Nature*. 1998;**394**(6690):251-253
- [2] Cumpston BH, Ananthavel SP, Barlow S, Dyer DL, Ehrlich JE, Erskine LL, et al. Two-photon polymerization initiators for three-dimensional optical data storage and micro-fabrication. *Nature*. 1999;**398**:51-54
- [3] Strickler JH, Webb WW. Three-dimensional data storage in refractive media by two-photon point excitation. *Optics Letters*. 1991;**16**:1780-1782
- [4] Denk W, Strickler JH, Webb WW. Two-photon laser scanning fluorescence microscopy. *Science*. 1990;**248**:73-76
- [5] Alkaisi MM, Blaikie RJ, McNab SJ, Cheung R, Cumming DRS. Sub-diffraction-limited patterning using evanescent near-field optical lithography. *Applied Physics Letters*. 1999;**75**(22):3560-3562
- [6] Mata A, Fleischman A, Roy S. Fabrication of multi-layer SU-8 microstructures. *Journal of Micromechanics and Microengineering*. 2006;**16**:276-284
- [7] Campbell M, Sharp DN, Harrison MT, Denning RG, Turberfield AJ. Fabrication of photonic crystals for the visible spectrum by holographic. *Nature*. 2000;**404**(6773):53-56
- [8] Lai ND, Liang WP, Lin JH, Hsu CC, Lin CH. Fabrication of two- and three-dimensional periodic structures by multi-exposure of two-beam interference technique. *Optics Express*. 2005;**13**(23):9605-9611
- [9] Lai ND, Zheng TS, Do DB, Lin JH, Hsu CC. Fabrication of desired three-dimensional structures by holographic assembly technique. *Applied Physics A*. 2010;**100**(1):171-175
- [10] Seet KK, Mizeikis V, Juodkazis S, Misawa H. Three-dimensional horizontal circular spiral photonic crystals with stop gaps below 1 μm . *Applied Physics Letters*. 2006;**88**(22):221101-221103
- [11] Sun HB, Matsuo S, Misawa H. Three-dimensional photonic crystal structures achieved with two-photon absorption photopolymerization of resin. *Applied Physics Letters*. 1999;**74**(6):786-788
- [12] Gissibl T, Thiele S, Herkommer A, Giessen H. Two-photon direct laser writing of ultra-compact multi-lens objectives. *Nature Photonics*. 2016;**10**:554-560
- [13] Straub M, Gu M. Near-infrared photonic crystals with higher-order bandgaps generated by two-photon photopolymerization. *Optics Letters*. 2002;**27**(20):1824-1826
- [14] Rensch C, Hell S, Schickfus MV, Hunklinger S. Laser scanner for direct writing lithography. *Applied Optics*. 1989;**28**(17):3754-3758
- [15] Bratton D, Yang D, Dai J, Ober CK. Recent progress in high resolution lithography. *Polymers for Advanced Technologies*. 2006;**17**:94-103

- [16] Li Q, Do MT, Ledoux-Rak I, Lai ND. Concept for three-dimensional optical addressing by ultralow one-photon absorption method. *Optics Letters*. 2013;**38**(22):4640-4643
- [17] Do MT, Nguyen TTN, Li Q, Benisty H, Ledoux-Rak I, Lai ND. Submicrometer 3D structures fabrication enabled by one-photon absorption direct laser writing. *Optics Express*. 2013;**21**(18):20964-20973
- [18] Wolf E. Electromagnetic diffraction in optical systems I. An integral representation of the image field. *Proceedings of the Royal Society A*. 1959;**253**(1274):349-357
- [19] Helseth LE. Focusing of atoms with strongly confined light potentials. *Optics Communication*. 2002;**212**(4-6):343-352
- [20] Sun HB, Tanaka T, Kawata S. Three-dimensional focal spots related to two-photon excitation. *Applied Physics Letters*. 2002;**80**(20):3673-3675
- [21] Lee CH, Chang TW, Lee KL, Lin JY, Wang J. Fabricating high-aspect-ratio sub-diffraction-limit structures on silicon with two-photon photopolymerization and reactive ion etching. *Applied Physics A*. 2004;**79**(8):2027-2031
- [22] Do MT, Li Q, Ledoux-Rak I, and Lai ND. Optimization of LOPA-based direct laser writing technique for fabrication of submicrometric polymer two- and three-dimensional structures. *Proc. SPIE 9127, Photonic Crystal Materials and Devices XI*. 2014
- [23] Matta JA, Outwater JO. The nature, origin and effects of internal stresses in reinforced plastic laminates. *Polymer Engineering and Science*. 1962;**2**(4):314-319
- [24] Scott TF, Kloxin CJ, Forman DL, McLeod RR, Bowman CN. Principles of voxel refinement in optical direct write lithography. *Journal of Materials Chemistry*. 2011;**21**:14150-14155
- [25] Chen KS, Lin IK, Ko FH. Fabrication of 3D polymer microstructures using electron beam lithography and nanoimprinting technologies. *Journal of Micromechanics and Microengineering*. 2005;**15**(10):1894-1903
- [26] Correa DS, Boni LD, Otuka AJG, Tribuzi V, Mendonça CR. Two-photon polymerization fabrication of doped microstructures. In: De Souza Gomes A, editor. *Polymerization*. Rijeka: InTech; 2012
- [27] Li L, Gattass RR, Gershgoren E, Hwang H, Fourkas JT. Achieving $\lambda/20$ resolution by one-color initiation and deactivation of polymerization. *Science*. 2009;**324**(5929):910-913
- [28] Nguyen DTT, Tong QC, Ledoux-Rak I, Lai ND. One-step fabrication of submicrostructures by low one-photon absorption direct laser writing technique with local thermal effect. *Journal of Applied Physics*. 2016;**119**(1):013101-013106
- [29] Carslaw HS, Jaeger JC. *Conduction of Heat in Solids*. 2nd ed. United Kingdom: Oxford University Press; 2000
- [30] Ovsianikov A, Shizhou X, Farsari M, Vamvakaki M, Fotakis C, Chichkov BN. Shrinkage of microstructures produced by two-photon polymerization of Zr-based hybrid photosensitive materials. *Optics Express*. 2009;**17**(4):2143-2148

- [31] Sun Q, Ueno K, Misawa H. In situ investigation of the shrinkage of photopolymerized micro/nanostructures: The effect of the drying process. *Optics Letters*. 2012;**37**(4):710-712
- [32] Sun HB, Suwa T, Takada K, Zaccaria RP, Kim MS, Lee KS, et al. Shape precompensation in two-photon laser nanowriting of photonic lattices. *Applied Physics Letters*. 2004;**85**(17):3708-3710
- [33] Maruo S, Hasegawa T, Yoshimura N. Single-anchor support and supercritical CO₂ drying enable high-precision microfabrication of three-dimensional structures. *Optics Express*. 2009;**17**(23):20945-20951
- [34] Lim TW, Son Y, Yang SY, Pham TA, Kim DP, Yang BI, et al. Net shape manufacturing of three-dimensional SiCN ceramic microstructures using an isotropic shrinkage method by introducing shrinkage guiders. *International Journal of Applied Ceramic Technology*. 2008;**5**(3):258-264
- [35] Sun Q, Juodkazis S, Murazawa N, Mizeikis V, Misawa H. Freestanding and movable photonic microstructures fabricated by photopolymerization with femtosecond laser pulses. *Journal of Micromechanics and Microengineering*. 2010;**20**(3):035004
- [36] Mao F, Tong QC, Nguyen DTT, Huong AT, Odessey R, Saudrais F, et al. LOPA-based direct laser writing of multi-dimensional and multi-functional photonic submicrostructures. *Proceedings of SPIE 10115, Advanced Fabrication Technologies for Micro/Nano Optics and Photonics X*. 2017;1011509
- [37] Tong QC, Luong MH, Remmel J, Do MT, Nguyen DTT, Lai ND. Rapid direct laser writing of desired plasmonic nanostructures. *Optics Letters*. 2017;**42**(12):2382-2385
- [38] Do MT, Nguyen DTT, Ngo HM, Ledoux-Rak I, Lai ND. Controlled coupling of a single nanoparticle in polymeric microstructure by low one-photon absorption-based direct laser writing technique. *Nanotechnology*. 2015;**26**(10):105301
- [39] TH A, Trinh DT, Tong QC, Do DB, Nguyen DP, Phan MH. Direct laser writing of magneto-photonic sub-microstructures for prospective applications in biomedical engineering. *Nanomaterials*. 2017;**7**(5):105
- [40] Markides H, Rotherham M, El Haj AJ. Biocompatibility and toxicity of magnetic nanoparticles in regenerative medicine, biocompatibility and toxicity of magnetic nanoparticles in regenerative medicine. *Journal of Nanomaterials*. 2012;**2012**:614094

We are IntechOpen, the world's leading publisher of Open Access books Built by scientists, for scientists

6,300

Open access books available

171,000

International authors and editors

190M

Downloads

Our authors are among the

154

Countries delivered to

TOP 1%

most cited scientists

12.2%

Contributors from top 500 universities



WEB OF SCIENCE™

Selection of our books indexed in the Book Citation Index
in Web of Science™ Core Collection (BKCI)

Interested in publishing with us?
Contact book.department@intechopen.com

Numbers displayed above are based on latest data collected.
For more information visit www.intechopen.com



1D Photonic Crystals: Principles and Applications in Silicon Photonics

Liangshun Han

Additional information is available at the end of the chapter

<http://dx.doi.org/10.5772/intechopen.71753>

Abstract

One-dimension (1D) photonic crystals have been widely used in silicon photonics due to its simple structure and multiple working regimes: diffraction, Bragg reflection, and sub-wavelength regimes. Thanks to recent development of photonic technologies and high-resolution lithography, many 1D photonic crystal-assisted silicon integrated devices have been proposed and demonstrated to further increase integration density and improve device performance. This chapter first presents some fundamentals of 1D photonic crystals. An overview of the applications of 1D photonic crystals in silicon photonics is then given including grating couplers, waveguide crossings, multimode interference couplers, polarization-independent directional couplers, hybrid lasers, polarizers, and high-order mode filters, among others. Particular attention is paid to providing insight into the design strategies for these devices.

Keywords: photonic crystals, diffractive gratings, sub-wavelength gratings, Bragg gratings, silicon photonics

1. Introduction

Extensive research has been performed to realize large-scale integration of silicon photonics for optical communication networks [1, 2], optical computing [3, 4], and biosensing [5, 6]. The impetus of this research lies in the fact that silicon-on-insulator (SOI) technology is fully compatible with complementary metal oxide semiconductor (CMOS) technology and possesses high refractive index contrast enabling compact devices. Recent efforts in silicon photonic devices, such as III-V/silicon hybrid lasers [7–9], modulators [10, 11], photodetectors [12], and switches [13, 14], have all paved a path toward realizing silicon-based high-density electronic and photonic integration circuits (EPICs) [15]. However, due to high-index contrast, photonic

devices based on SOI waveguides always suffer from some issues including high polarization sensitivity, limited bandwidth, severe phase errors caused by fabrication, thermal sensitivity, and relatively large loss. Those issues greatly limit application range of silicon-based photonic devices. There has been considerable effort by the international community to improve device performances by designing new structures, introducing new materials, combining different effects, developing new fabrication processes, discovering new functionalities, etc. The application of 1D photonic crystals in silicon photonics is a representative example.

1D photonic crystals are the simplest structure in photonic crystal family [16]. Interestingly, 1D photonic crystals still possess many exciting properties such as adjustable dispersion and birefringence, acting as homogeneous materials. Compared with 2D or 3D photonic crystals, the simple structure of 1D photonic crystals makes them easy to be integrated with the existing photonic devices without changing fabrication procedures. Consequently, many high-performance silicon-based devices have been proposed and demonstrated by exploiting those exciting properties of 1D photonic crystals. This chapter aims to provide the readers with some fundamentals of 1D photonic crystals and present an extensive overview of their applications in silicon photonics. The chapter is organized as follows. Section 2 describes the fundamentals of 1D photonic crystals. For the sake of clarity, the overview of their applications is divided into three sections (Sections 3–5) on the basis of three operating regimes.

2. Fundamentals of 1D photonic crystals

In silicon photonics, the 1D photonic crystals can be formed by periodic strip structures as shown in **Figure 1**. Normally, those strips are high-index crystal silicon layer which is optical waveguide core layer as well. The high-index strips are surrounded by low-index material such as air, silicon oxide, and polymer to form a periodically modulated refractive index distribution. In general, the incident direction of light could be any direction relative to photonic crystals. In practical terms, two special cases are widely employed: (a) light propagates crosswise through the 1D photonic crystal (propagation along the y - or z -axis in **Figure 1**), and (b) light propagates lengthwise through the 1D photonic crystal (propagation along the x -axis in **Figure 1**). In this chapter, we will focus on lengthwise periodic structures since lengthwise structures can be easily integrated with sub-micrometer

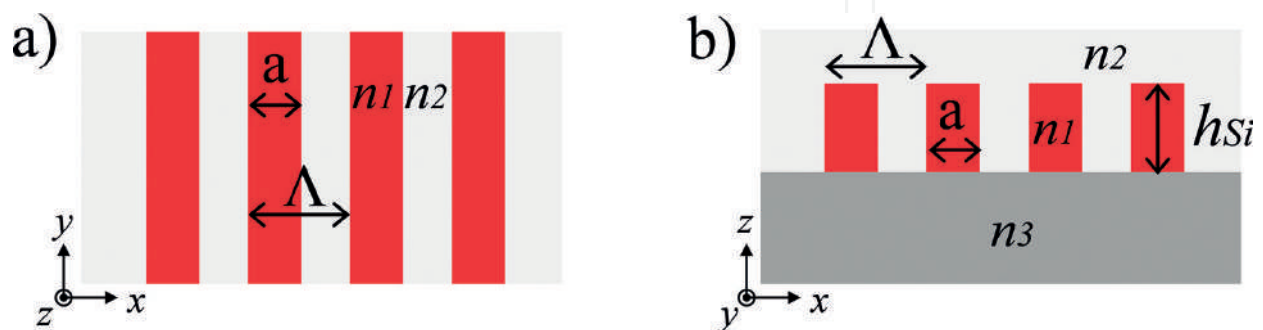


Figure 1. (a) Top view and (b) cross section of a 1D photonic crystal.

silicon waveguides and provide more flexibilities than that of crosswise periodic structures. Nowadays, extensive review papers and books are available for fully understanding the specific electromagnetic properties of the periodic structures considered here [16]. However, to provide intuitive guidelines for the design process, a much simpler theory will be used in this chapter.

A lengthwise 1D photonic crystal shown in **Figure 1** generally operates in the following three regimes, depending on the ratio between the structure's pitch (Λ) and the operating free-space wavelength (λ):

- i. Diffraction regime. The incoming beam is scattered in different orders.
- ii. Bragg reflection regime. The incoming beam is reflected backward.
- iii. Sub-wavelength regime. The diffraction and reflection effects due to the periodicity of the structure are suppressed.

Figure 2 shows a schematic k - ω diagram of a 1D periodic structure with lengthwise propagation (along the x -axis) [16]. One can see that, for a given pitch periodic structure, the working regime is strongly related to free-space operating wavelength λ or operating frequency ω . When $\omega > \omega_2$ (above the first photonic bandgap), the waveguide becomes lossy for Bloch mode, and the light will be radiated out of the waveguide. This character has been utilized to design fiber-to-chip surface couplers (grating couplers). In the frequency range of $\omega_2 > \omega > \omega_1$ (the first photonic bandgap), light cannot propagate through the periodic structure and is reflected, and this is Bragg reflection regime. The propagation constant in this regime is

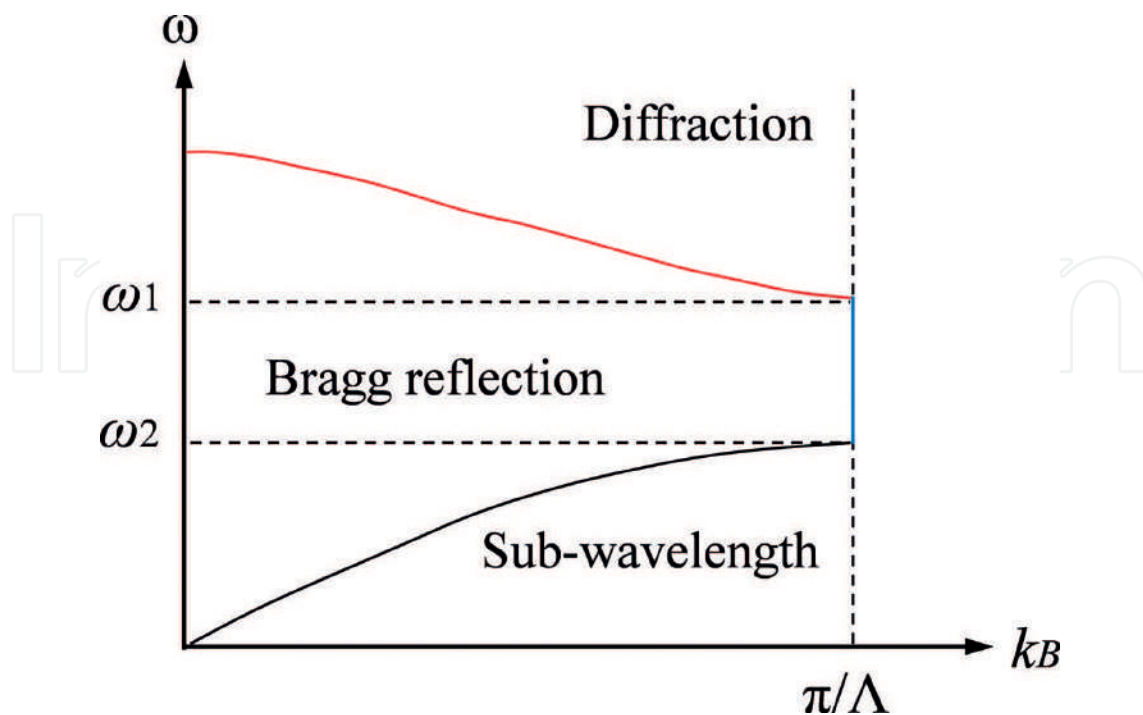


Figure 2. The schematic band diagrams a 1D photonic crystals with lengthwise propagation (along the x -axis).

constant: $k_B = \pi/\Lambda$. The bandgap has been extensively exploited to design distributed Bragg reflectors (DBRs) on different photonic platforms.

The last regime is located below the first photonic bandgap where the operating frequency is smaller than ω_1 . From **Figure 2**, one can find that the propagation constant k_B grows monotonically as operating frequency increases, indicating that the periodic waveguide behaves as a conventional waveguide. Thus, in sub-wavelength regime, periodic structures work as homogeneous media. Consider a general case, light propagates (along the x-axis) through the structure (shown in **Figure 1**), with a linear polarization either parallel (E_{\parallel}) or perpendicular (E_{\perp}) to the interfaces between the two media. The equivalent effective index of the structure can be expressed with the zeroth-order approximation [17]:

$$n_{\parallel}^2 = \frac{w}{\Lambda} n_1^2 + \frac{\Lambda-w}{\Lambda} n_2^2 \quad (1)$$

$$\frac{1}{n_{\perp}^2} = \frac{w}{\Lambda} \frac{1}{n_1^2} + \frac{\Lambda-w}{\Lambda} \frac{1}{n_2^2} \quad (2)$$

where w/Λ is duty cycle of the structure. Thus, both effective index and effective birefringence can be engineered by adjusting the geometry of the structure. This allows for completely new design approaches and can be exploited in a variety of devices. Eqs. (1) and (2) also apply to crosswise structures.

3. Applications of diffraction regime

For the sake of clarity, the discussion on the applications of 1D photonic crystals in silicon photonics is divided into three parts. Hereinafter, we will use the general expression “diffractive gratings” and “sub-wavelength gratings (SWG)” to indicate the 1D photonic crystals operating in diffraction regime and in sub-wavelength regime, respectively. This section is devoted to applications of the diffraction regime. Applications of sub-wavelength regime and Bragg reflection regime are discussed in Sections 4 and 5, respectively. This section focuses on the key components in silicon photonics: grating couplers. To further improve the performance, combination of diffractive gratings and crosswise sub-wavelength structures is also presented.

A grating coupler is a 1D periodic structure that can diffract light from propagation in the waveguide (in plane) to free space (out of plane). By placing an optical fiber above the chip, part of the radiated light is collected. It is normally used as an I/O device to couple light between fiber and sub-micrometer silicon waveguides. And, grating couplers are defined lithographically and can be placed anywhere on the chip surface to enable inputs and outputs, which are particularly useful for massive production. **Figure 3** shows the cross section view of a shallow-etched grating coupler on a SOI wafer. The thickness of the core silicon layer and the thickness of the buried oxide (BOX) layer are determined by the wafer type. Normally, the thickness of core silicon layer (h_{Si}) is 150–300 nm. The cladding material is usually air ($n_2 = 1$), silicon dioxide, or an index-matching liquid ($n_2 \sim 1.45$).

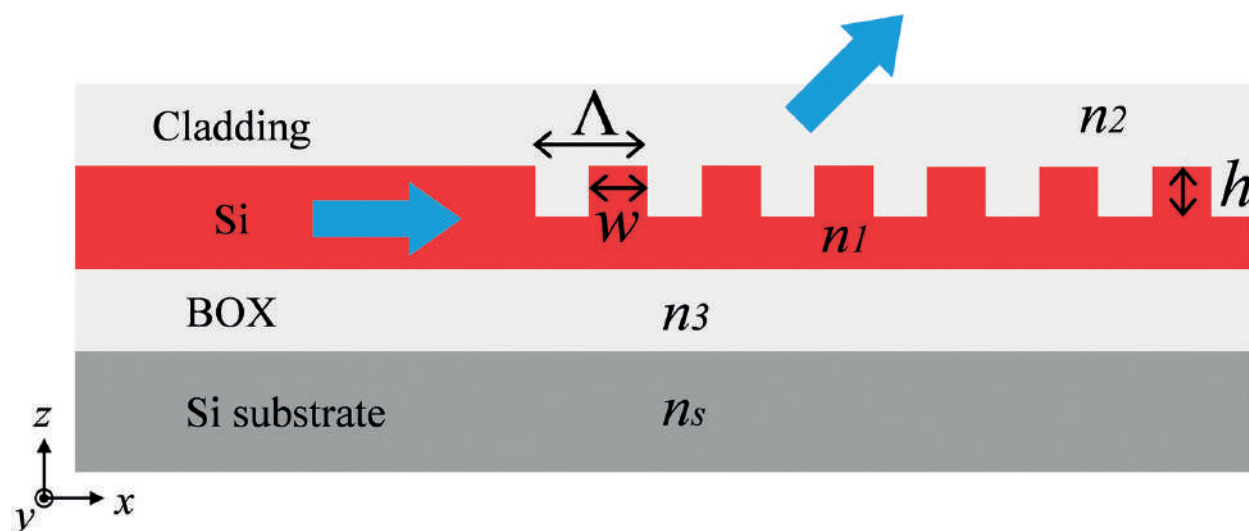


Figure 3. The cross section view of a shallow-etched grating coupler.

Figure 4 illustrates the concept of a grating coupler working as an output coupler. The operation of a grating coupler can be understood by the constructive and destructive interference arising from the wave fronts generated by the diffraction of light from the grating strips [18, 19]. First, we can check Figure 4a. In this case, the operating wavelength matches the pitch of the gratings. The first-order diffraction will vertically propagate, and the second-order diffraction will be back to the waveguide. However, the back-traveling light will be considered as reflection for the silicon waveguide, which is undesired since the light path between two grating couplers can form a Fabry-Perot oscillation cavity. This oscillation will modulate the transmission of other components. One efficient way to address this issue is detuning the grating and tilting the fiber (see Figure 4b) with a small angle to the grating surface. When the wavelength inside waveguide is smaller than the pitch of the gratings, the diffracted light waves will propagate at an angle, and reflection caused by second-order diffraction will be strongly suppressed.

The grating coupler could be well described by Bragg Law. If the grating parameters are fixed as constants (such as pitch and refractive indices of layers), then the radiation angle is given by the equation [18]:

$$n_2 \sin \theta_k = n_{eff} + \frac{k\lambda}{\Lambda} \quad (3)$$

where n_2 is the refractive index of the cladding material (see Figure 3) and k is an integer which represents the diffraction order. In some literatures, the effective index n_{eff} is substituted by Bloch-Floquet mode index (n_B). The main reason is that the relatively short light extraction length between a fiber and a grating coupler generally causes a strong perturbation in the waveguide. But for preliminary design process, using effective index is enough to qualitatively understand the property. In Ref. [18], only when $\sin \theta_k$ is real, the gratings diffract light from the waveguide. Consequently, we can play with the pitch of gratings so that only the order $k = -1$ occurs or dominates.

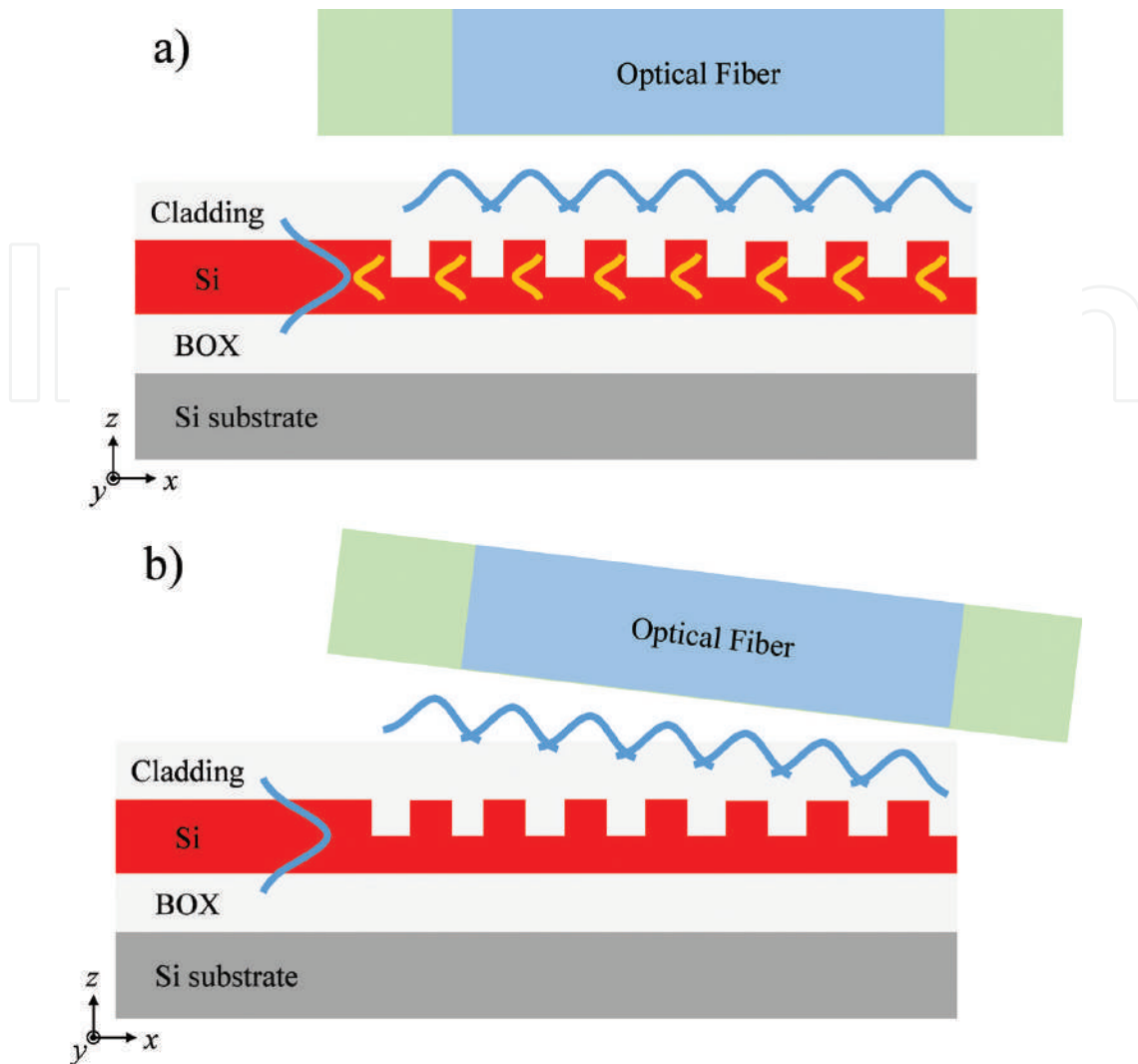


Figure 4. Diagrams describing the concept of a grating coupler working as an output coupler. (a) Vertical first-order diffraction and backward second-order diffraction and (b) tilted first-order diffraction without second-order diffraction.

A straightforward way to realize a grating coupler is using straight gratings connected to a taper to convert the fiber mode to a narrow waveguide mode. To obtain high conversion efficiency, the taper length needs to be more than $100\ \mu\text{m}$ [19–21], which is undesirable for compact and high-density integration schemes. Alternatively, confocal gratings enable more compact designs. The whole grating is shaped to an ellipse with a common focal point, which coincides with the optical focusing point where the single-mode silicon waveguide is connected [22, 23].

One vital property of grating couplers is coupling efficiency. There are three main factors that contribute to a reduced efficiency of a grating coupler:

- i. Penetration loss, that is, the fraction of waveguide power that escapes into the substrate. For a shallow-etch structure, there is about 30% of power lost in the substrate; and the penetration loss can be more than 50% in a full-etch structure [19]. This can be improved by using reflectors imbedded in the substrate [24–26]. As a result, the upward radiated

optical power is improved, and radiation downward the substrate is reduced. Those reflectors can be a metal layer or multiple-layer-distributed Bragg reflector.

- ii. Back reflection, that is, the optical power reflected from the coupler into the waveguide. For a well-designed shallow-etched grating coupler, the back reflection is less than -20 dB, so this does not contribute a significant loss to the coupler. However, this loss can be much higher in a full-etched grating coupler. Coupling the light under a small angle also helps to eliminate the first-order Bragg reflection, which is another reason why grating couplers are often designed with a coupling angle.
- iii. Mode mismatch, that is, the overlap integral between the diffracted light beam and the near-Gaussian optical fiber mode [27]. In theory, the overlap integral is determined by the fraction of waveguide power diffracted from each pitch of the gratings. Approximately, this fraction is in direct proportion to refractive index difference between the strips of the gratings and the grooves. Therefore, in comparison with full-etched structures, a shallow-etched structure possesses a lower index difference which produces a relative wide radiated light beam. Consequently, conventional grating couplers with shallow-etched gratings help enhancing the field overlap.

It should be noted that the power loss caused by mode mismatch can be further improved by apodizing or chirping the gratings [20, 28, 29] in which the index difference is varied along the structure to obtain a radiated beam that resembles the optical fiber mode. Duty cycle varied crosswise SWG structures can also enable the design of apodized grating couplers fabricated by a single, full-etch step. Consider a crosswise SWG structure enabled grating coupler shown in **Figure 5**. x direction is the in plane propagation direction of a conventional grating coupler, and the original grooves are occupied by crosswise SWG structures acting as artificial homogeneous media. The equivalent index of SWG can also be approximately estimated by Eqs. (1) and (2). Thereby, a grating can be apodized by varying the duty cycle (w_y/Λ_y) of the SWG structure located in each groove. However, the introduction of crosswise SWG structures also causes a variation of the radiation angle θ along the grating. To compensate

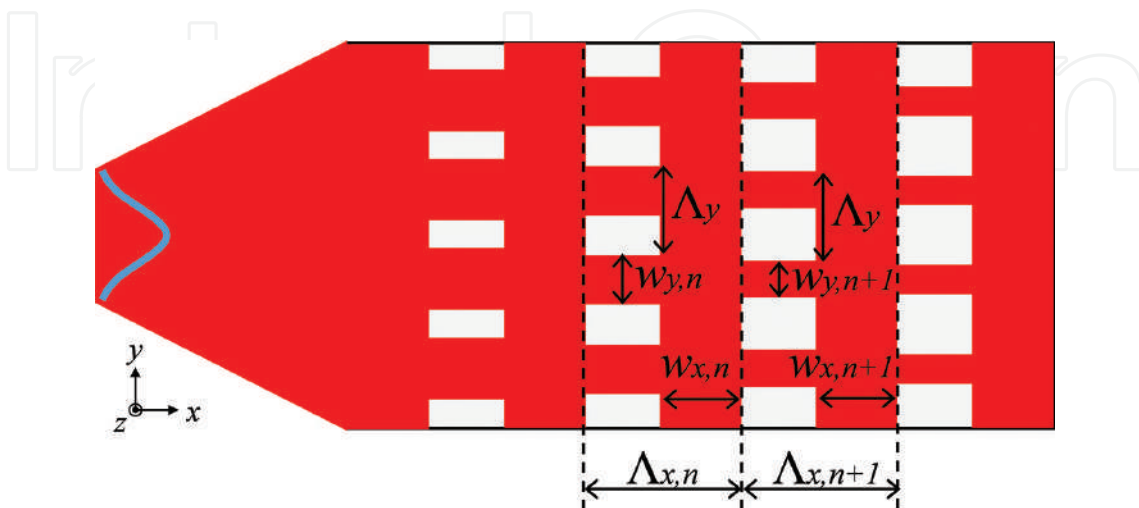


Figure 5. Top view of an apodized grating coupler with crosswise SWG structures.

this variation, chirping the grating along x direction is necessary. An apodized grating coupler with focusing design exhibiting a coupling efficiency of -1.8 dB was reported in Ref. [30].

The combination of diffractive gratings and crosswise SWG structures is also exploited to obtain polarization-independent grating couplers [31, 32]. Conventional grating couplers are highly polarization sensitive, which can be used as polarization filters or polarizers. The effective index in the grating region is highly birefringent, causing different radiation angles for TE and TM polarization states. When we consider a grating coupler with SWG structures shown in **Figure 5**, the effective index of the TE (z -polarized) mode will be much larger than that of the TM (y -polarized) mode in the silicon slab regions. However, in the sub-wavelength regions, from Eqs. (1) and (2), it was found that the effective index of the TE mode n_{\perp} is smaller than that the TM mode n_{\parallel} . It is possible to design grating region so that these two effects cancel each other resulting in an identical Bloch mode effective index for both polarization states. Consequently, the grating coupler becomes polarization independent. Ref. [32] demonstrated a similar design possessing a coupling efficiency of -6.5 dB for both polarization states.

Broadband grating couplers with SWG structures were also proposed and demonstrated. A grating coupler with a bandwidth of ~ 100 nm and a coupling efficiency of -5.6 dB was presented in Ref. [33]. A simulated bandwidth of ~ 300 nm and a coupling efficiency of -2.8 dB were obtained by employing fully etched triangular holes in Ref. [34].

4. Applications of sub-wavelength regime

This section further presents applications of lengthwise SWG structures in which light propagates perpendicularly to the interfaces of the structure (along the x direction in **Figure 1**). As mentioned in Section 2, it is possible to engineer both effective index and effective birefringence which can be exploited in many silicon photonic devices for optical bandwidth and polarization-sensitivity improvement. In this section, we first discuss the mode convertor between SWG-based waveguides and conventional waveguides, which is the basic component for integration of these two kinds of technologies. Then, we move to some other key components such as waveguide crossings, multimode interference (MMI) couplers, and wide-band and polarization-independent directional couplers.

4.1. Mode converters

To fully utilize the properties afforded by SWG-based waveguides and other components, integration and interconnect with conventional waveguides are needed. There are two key points to design such mode converters: low loss and low reflection. To attain both targets, several works have been done in theories and experiments [35, 36]. **Figure 6** shows the schematic diagram of a mode converter which contains three parts: conventional waveguide section, transition section between conventional waveguide and SWG-based waveguide, and SWG-based waveguide section. The transition section determines the performance of this mode converter; a clear approach is chirping the pitch and duty cycle and incorporating bridging

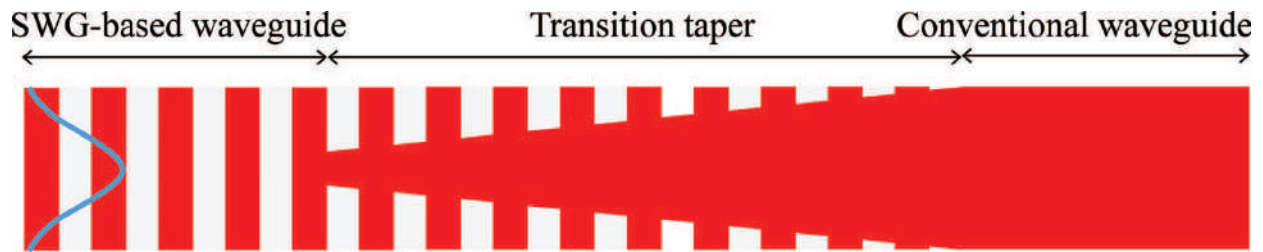


Figure 6. Top view of a SWG-based mode converter with section indications.

elements between the two waveguide sections [36]. Similar to conventional inverse taper, the mode effective index in transition section also gradually changes along propagation; thus, particular care should be taken for avoiding Bragg reflection regime within target operating optical bandwidth.

Mode converters can also be used for fiber-to-chip coupling [35, 37] and coupling between continuous fields and discretized fields [38]. For fiber-to-chip coupling applications, mode converter is carefully designed to match the on-chip waveguide mode size, shape, and effective index to that of a single-mode fiber, thereby increasing coupling efficiency. The insertion loss of such mode converter was extracted from experiments: -0.23 dB for TE mode and -0.47 dB for TM mode [38]. The application for coupling between continuous fields and discretized fields can be found in arrayed waveguide grating (AWG). In an AWG, the main loss and backward reflection are from transition between the slab waveguide (where continuous fields are from) and the array waveguides (where discretized fields appear). The loss is from the gap between arrayed waveguides, and reflection is caused by high-index difference between slab region and free propagation region. By placing well-designed SWG structures between arrayed waveguides, the index difference and fields coupling can be further optimized. Ref. [39] shows some experimental results about AWGs with SWG-based mode converters.

4.2. Waveguide crossings

An efficient waveguide crossing is highly desired to materialize the full potential of silicon photonics for on-chip optical interconnects. Due to the high-index contrast of the silicon platform such as SOI, the insertion loss of a conventional waveguide crossing is around 0.15 dB. To reduce optical loss, waveguide crossing designed by using particle swarm optimization has been proposed and demonstrated, with a loss of -0.028 ± 0.009 dB for 1550 nm operating wavelength [40]. In this part, we introduce some waveguide crossing designs assisted by SWG structures. The experimentally confirmed insertion loss is comparable with or even lower than that of particle swarm-optimized designs. A further advantage of using SWG structures is improving optical bandwidth and polarization sensitivity.

First, we go through some fundamentals of conventional waveguide crossings. **Figure 7a** gives the top view of a conventional waveguide crossing, and cross section of the multimode waveguide region is shown in **Figure 7b**. A conventional design is composed of MMI regions, single-mode access waveguides, and a crossing section. It was found that the intrinsic loss of such design is attributed to three aspects:

- i. Phase error in the MMI region. When wide multimode waveguides are utilized, it is possible to find more than two modes excited in MMI regions. Some phase errors will appear, and the perfect self-imaging position cannot be found by adjusting MMI length. To avoid exciting high-order modes, narrow multimode waveguides supporting three modes (fundamental, first order, and second order) are applicable. Among these modes, only fundamental and second-order modes are excited in an symmetric interference MMI structure. Then, the self-imaging length is only related to two modes, and high-order mode phase errors could be thoroughly eliminated.
- ii. Loss caused by sharp transitions between single-mode waveguides and MMI regions. As suggested by [41], a linear or nonlinear taper can be applied to reduce the transition loss. It is worth to underline that the taper also affects the power portion in the second-order mode in MMI regions [42]. Through simulation, we can find the optimal power ratio between fundamental mode and second-order mode. If the power ratio is too small, the MMIs even lose the capability of focusing light beam at the center of the crossing section, causing mode mismatch between the diverged beam after passing through the crossing section and the guided modes of the multimode waveguide. When the power ratio is larger than the optimal value, a large amount of the second-order mode possessing a wide angular spectrum scatters through the crossing section, and some of it radiates into the orthogonal MMI regions, resulting in substantial loss and crosstalk. Consequently, when choosing the length of the taper, a trade-off between modal transition loss and two-mode power ratio needs to be found.
- iii. Mode mismatching between multimode waveguides and the crossing section. The crossing section is much wider than the multimode waveguide width, which can be considered as a slab waveguide that supports pure TE modes. However, the mode in the single-mode access waveguide and the second-order mode in the multimode waveguide are both quasi-TE modes with a considerable amount of TM polarization. Then, the TM mode power will be dissipated in the crossing section. It is found that the power portion of TM polarization can be effectively suppressed by increasing the lateral cladding index (n_{lc}) in MMI regions. One straightforward way is depositing a high-index material such

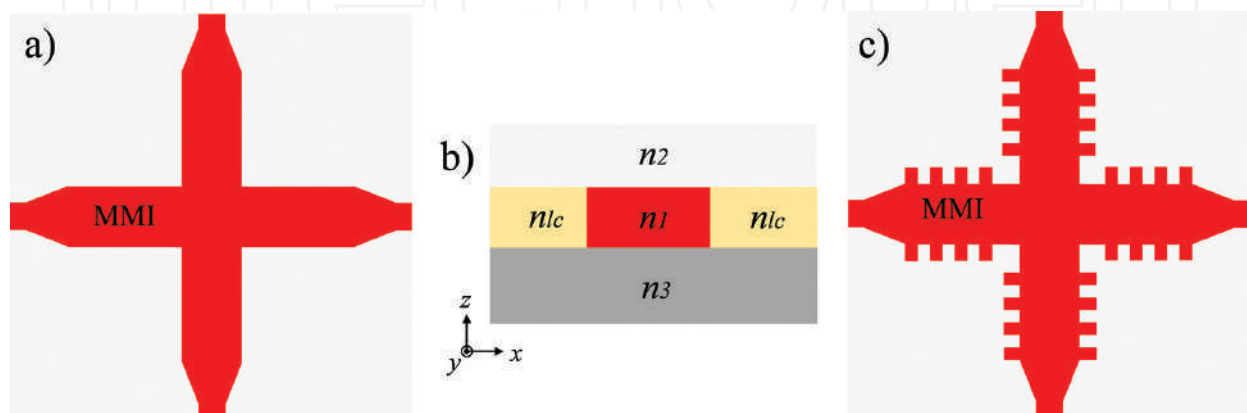


Figure 7. (a) Top view of a conventional waveguide crossing, (b) cross section view of MMI sections, and (c) top view of a SWG-assisted waveguide crossing design.

as $\text{Si}_x\text{N}_{1-x}$. Also, using a tightly controlled shallow-etched structure is feasible. Both approaches complicate the fabrication process.

In Ref. [42], researchers developed a new waveguide crossing assisted by SWG structures to engineer the lateral cladding index, simplifying fabrication procedures. **Figure 7c** gives the schematic of such design. A 101×101 MMI crossing matrix was demonstrated on the SOI platform. An insertion loss of 0.019 dB and a crosstalk lower than -40 dB at 1550 nm operating wavelength were obtained for each crossing. It is worth to note that the optical bandwidth (90 nm) is wider than that of conventional designs.

Figure 8 shows another waveguide crossing design that lies on SWG-based waveguides [43]. In comparison with the designs shown in **Figure 7a** and **7c** this waveguide crossing has no multimode waveguides. At the center of the crossing, a squared segment is used to enable a symmetrical structure. Loss per crossing was measured as 0.023 dB with polarization dependent loss of <0.02 dB and crosstalk below -40 dB [43]. An improvement from this design is polarization insensitivity. More discussions can be found in Ref. [43].

4.3. MMI couplers

MMI couplers are widely used as basic building blocks in many advanced photonic devices including MZ modulators [10], polarization-handling devices [44], mode handling devices [45, 46], etc. Before reviewing some high-performance MMI coupler assisted by SWG structures, we will briefly recall the fundamental limitations of conventional MMI couplers.

A MMI coupler consists of single-mode in-/output waveguides and a multimode waveguide section, as shown in **Figure 9**. The input light beam excites multiple modes in the central section with different excitation coefficients. The coefficients are determined by input mode profile and the structure of the central section (MMI section). Those modes propagate through the central section with different propagation constants (β_m) and interfere with each other to form the N -fold self-imaging of the input mode [47]. Placing output waveguides at the imaging position, beam splitting and combining function can be achieved. The MMI or central section length (L_{MMI}) has a certain relationship with beat length (L_π) of the two lowest excited modes in the central section. The beat length at operating wavelength is given by

$$L_\pi = \frac{\pi}{\beta_1(\lambda) - \beta_2(\lambda)} \quad (4)$$

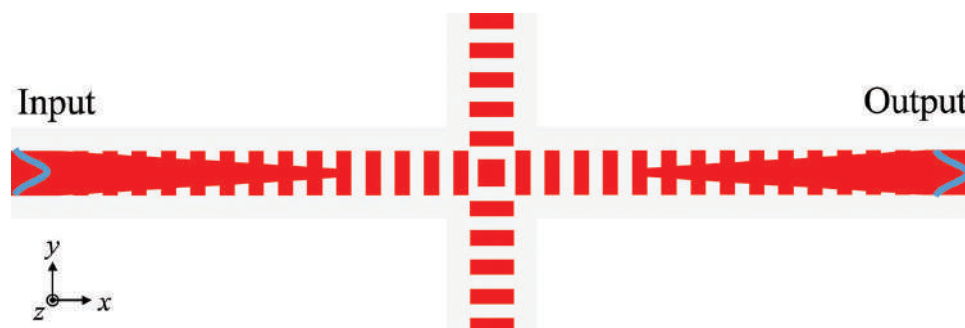


Figure 8. Top view of a SWG-based waveguide crossing.

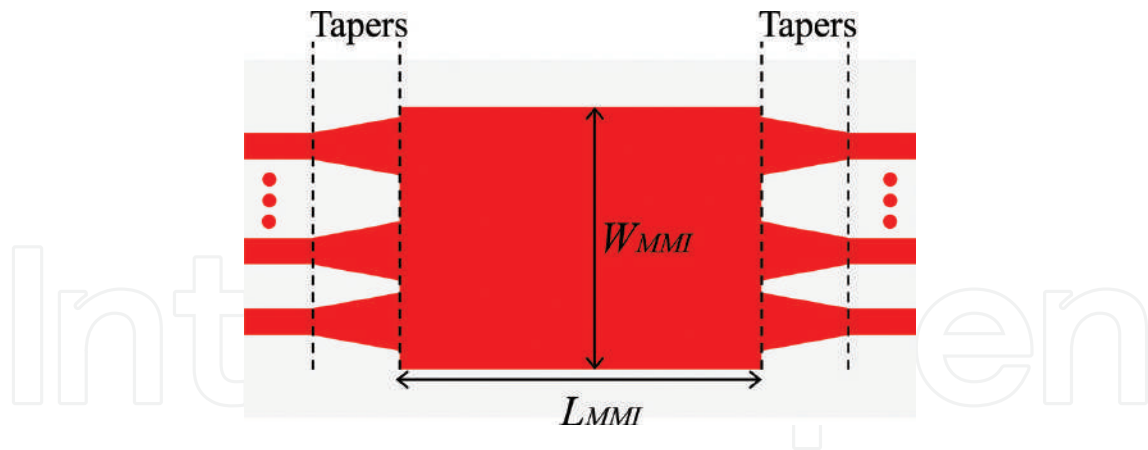


Figure 9. Schematic of a MMI coupler with indications.

Furthermore, to obtain clear images for low loss and power imbalance of MMI couplers, the propagation constant of each excited mode needs to meet the following relation:

$$\beta_m = \beta_1 - \frac{(m^2 - 1)}{3L_\pi} \pi \quad (5)$$

where m is the mode order and β_1 is the propagation constant of the lowest-order mode. Unfortunately, this condition is only satisfied for the lower order modes, which causes MMI's phase error and excess loss. An obvious approach is to suppress excitations of higher order modes, which can be done by increasing modal width of input mode and reducing the number of modes that MMI supports. Inserting tapered input waveguides between single-mode waveguides and the central section (as shown in **Figure 9**) in return increases modal width ratio between input mode and the excited fundamental mode, resulting in a limited number of (the lower order) modes excited. About reducing supported modes in the central section, reducing the width of MMI section (same effect as that of the use of tapered input) and increasing lateral cladding index (decrease core-cladding refractive index contrast) are feasible methods.

In Eq. (4), the beat length is described only for a certain wavelength. We rewrite the equation as

$$L_\pi = \frac{\lambda}{2(n_1(\lambda) - n_2(\lambda))} \quad (6)$$

It can be seen that the beat length decreases with increasing wavelength. This is the major limitation of the bandwidth of a MMI coupler. To achieve broadband MMI couplers, we need to find a way to suppress high-order modes excited in MMI section and keep $(n_1(\lambda) - n_2(\lambda))$ increasing as wavelength increases.

Now, we review two high-performance MMI couplers assisted by SWG structures. The first case is 4×4 MMI coupler serving as a 90° hybrid for coherent detections. One vital parameter of this MMI coupler is phase error. As discussed before, the use of input taper is a common practice to obtain small phase errors. But for SOI platform, only using input taper is not enough to meet the target since the large core-cladding index contrast in SOI waveguides

leads higher-order modes to not properly fulfill Eq. (4). The large lateral index contrast can be tailored by an (some) extra shallow-etch step(s) to define shallow-etched multimode region. This was experimentally confirmed as an efficient way [48]. However, extra etch steps and tightly controlled etching depth are required, complicating the fabrication process and not suitable for massive production. Instead of introducing shallow-etch process, laterally integrating SWG structures also allows for lateral cladding index engineering with single full-etch step. The design process is straightforward: (1) calculate the equivalent effective index of SWG structures under different pitch and duty cycles; (2) sweep the cladding index of a 4×4 MMI coupler to find an optimum value; (3) use the data calculated in Step 1 as a lookup table and, then, geometry parameters of the sub-wavelength structure that yields the desired value of lateral cladding index can be found; and (4) use FDTD to further verify the structure. The schematic diagram is depicted in **Figure 10a**. Simulated common mode rejection ratio and phase error of less than 24 dBe and 2° , respectively, are presented in Ref. [49]. This technology can be also exploited in any $N \times N$ MMI coupler.

The second case is broadband 2×2 MMI coupler. In practices, broadband MMI couplers are demanded to simplify system and reduce cost. Similar to the above case, optimization of tapered input broadens the bandwidth. In Ref. [50], researchers proposed a broadband 2×2 MMI coupler in which the conventional multimode section is replaced with a length-wise SWG-based waveguide of $6.0 \mu\text{m}$ width, 198.0 nm pitch, and 50% duty cycle. The schematic diagram is shown in **Figure 10b**. To fully understand how the SWG structures can be exploited to significantly increase the bandwidth of MMI couplers, it is useful to replot the sub-wavelength regime in **Figure 2** in an equivalent way as shown in **Figure 11**. One can see that the sub-wavelength regime can be divided into two regions: high dispersion region (λ is close to Bragg wavelength) and low dispersion region ($\lambda \gg \Lambda$). The exciting part is that the dispersion value is adjustable through changing pitch, which can be utilized to design broadband MMI couplers. In results, the bandwidth of the MMI coupler in **Figure 10b** is determined by the pitch. To connect with conventional waveguide structures, mode converters similar as the one described in Section 4.1 were placed at in-/output ports as shown in **Figure 10b**. The mode converters also help to expand mode field to excite only lower-order modes. Due to the relatively low equivalent refractive index of the SWG-based multimode section, the MMI length is also shortened in return. Additionally, this technology can be applied to design broadband directional couplers [51].

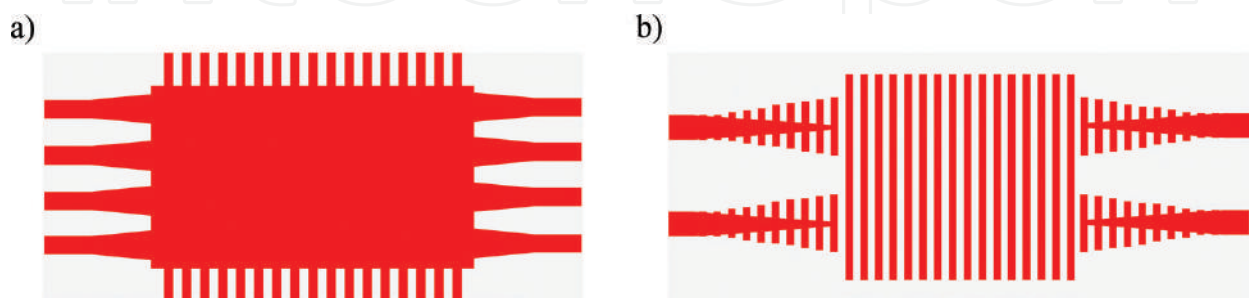


Figure 10. Schematics of MMI couplers: (a) a 4×4 MMI coupler with lateral SWG structures and (b) a 2×2 MMI couplers with SWG-based multimode section.

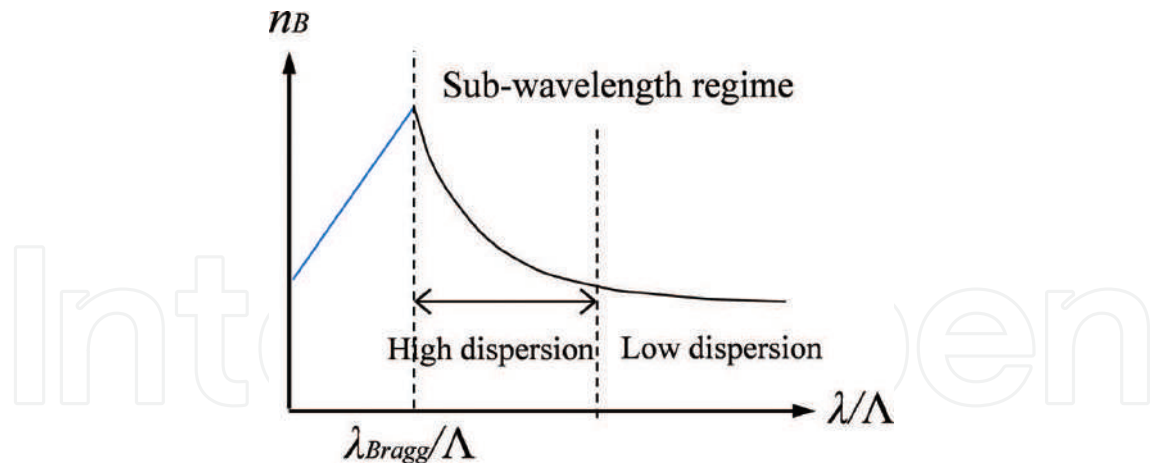


Figure 11. Dispersion in sub-wavelength regime.



Figure 12. Schematic of a polarization-independent directional coupler based on slot waveguides with SWG structures.

4.4. Polarization-independent directional couplers

With its superior performances, directional coupler (DC) has attracted considerable attentions and been widely used in many applications, including on-chip sensors, filters, switches, and polarization beam splitters. In comparison with other couplers, such as MMI couplers and Y-branch couplers, DCs process valuable properties in terms of ultra-low loss, low reflection, and arbitrary power coupling ratio obtained by adjusting the length and gap of the coupling region. However, by using sub-micrometer SOI waveguides, the beat length of TE mode greatly differs from that of TM mode due to the high birefringence of silicon waveguides, resulting in power ratio sensitivity to polarization states. Polarization-independent DC is useful for some applications where the amount of collected or split optical power is concerned. Some techniques have been proposed and experimentally confirmed to address this issue. One solution is to use polarization diversity schemes where polarization splitting and rotating devices are needed, which increases system size and complexity. Another approach is to make the directional coupler inherently polarization insensitive [52–54].

Recently, a SWG-assisted slot waveguide polarization-independent DC with relatively large fabrication tolerance has been demonstrated on SOI chip [55]. **Figure 12** describes the schematic diagram of this design. The SWG structures are extended into the gap between two parallel slot

waveguides. The SWG structures are considered as homogenous media. By calculating the relation between beat length of both polarization states and refractive index of SWG structures (n_k), it was found that the two curves are of different slopes. By adjusting the duty cycle, if the effective indices of the TE mode n_{\perp} and TM mode n_{\parallel} in SWG structures meet the n_{kTE} and n_{kTM} for same beat length for TE and TM modes, then the optimum duty cycle is attained. FDTD simulations for further confirmation are necessary. The measured coupling efficiency is 97.4 and 96.7% for TE and TM modes, respectively, at a wavelength of 1550 nm. It is worth noting that an additional advantage of this design is its wide bandwidth over 120 nm (1475–1595 nm) theoretically and exceeding the entire C-band (1525–1570 nm) experimentally. To interconnect such design with a conventional waveguide, a slot-to-strip waveguide converter is required.

5. Applications of Bragg reflection regime

This section is devoted to applications of Bragg reflection regime of 1D photonic crystals. For the sake of clarity (unless otherwise stated), hereinafter we will use the general expression “Bragg gratings” to indicate the 1D photonic crystals operating in Bragg reflection regime as shown in **Figure 2**. One prominent feature of Bragg gratings is the linear relation $n_{Bragg} \sim \lambda/\Lambda$ within the photonic bandgap ($\omega_1 > \omega > \omega_2$). The bandgap has been extensively exploited to design DBRs on different photonic platforms as key elements of DBR lasers [56, 57], distributed feedback (DFB) lasers [58, 59], fiber Bragg gratings (FBGs) [60], VCSELs [61], etc. On silicon platform, silicon waveguide-based Bragg gratings have been integrated with III–V gain elements to provide optical feedback for lasers on a silicon chip.

This section starts with a brief discussion of Bragg gratings serving as mirrors in hybrid lasers on a silicon chip (Section 5.1). Section 5.2 is dedicated to Bragg gratings designed as a polarizer and higher-order mode pass filter.

5.1. Hybrid lasers with Bragg gratings

The realization of an efficient, reliable, and electrically pumped laser on a silicon wafer is still a scientific challenge. In Ref. [15], researchers first demonstrated a high-performance electrically pumped quantum-dot laser through epitaxial growth of III–V materials on a silicon substrate. Another common-practice approach to realize light source on a silicon wafer is wafer bonding. Several bonding process schemes have been proposed [9, 62–66]. To fabricate a single-wavelength laser and multiwavelength laser array, prefabricated single-wavelength laser diodes can be directly bonded on a silicon wafer [62]. Alternatively, embed III–V gain sections to silicon photonic circuits and the wavelength-selections are done by some silicon-based wavelength-sensitive devices such as ring resonator, slotted feedback structure, and Bragg reflector. In Ref. [66], a four-channel multiwavelength DFB evanescent laser array was designed and fabricated. Beneath each III–V gain section, Bragg gratings were fabricated on the surface of the silicon waveguide. The ASE from a gain section propagates and evanesces into a silicon waveguide and is modulated by gratings, forming a DFB laser. For realizing different channel wavelengths, the width of silicon waveguide is varied to obtain different Bragg propagation constants.

5.2. TM-pass polarizers

Photonic devices based on SOI waveguides always suffer from severe polarization-sensitivity problems due to high birefringence, which greatly limits their application range. Various polarization-handling devices have been attracting attentions, including polarization beam splitters, polarization rotators [67], and polarizers. Among them, a polarizer is used to achieve linearly polarized light with a high extinction ratio. In practices, a low loss, high extinction ratio, and compact footprint polarizer is highly desired. Many designs have been proposed and demonstrated on silicon wafers [68–70]. The basic rationale of designing a polarizer is to lose or filter unexpected polarization state out from the optical propagation paths with negligible effect on desired polarization state and maintain the device size as small as possible.

In Ref. [71], a waveguide-based TM-pass polarizer is fabricated with 1D photonic crystals. The schematic of this design is depicted in **Figure 13**. The device is composed of three parts: in-/output waveguides, 1D photonic crystal with teeth and bridges, and transition tapers. The pitch was well designed to make the waveguide supporting Bloch mode for TM polarization state, so that the incident TM-polarized light goes through the waveguide with very low excess loss. On the other hand, for TE polarization state, the waveguide works as a Bragg reflector, and consequently the incident TE-polarized light is reflected with very high efficiency. Therefore, the following conditions should be satisfied approximately [71]:

$$n_b^{TE}(\Lambda - w) + n_{ac}^{TE} w = \lambda/2 \quad (7)$$

$$n_b^{TM}(\Lambda - w) + n_{ac}^{TM} w < \frac{\lambda}{2} \quad (8)$$

where n_b and n_{ac} are the effective indices of the TE or TM modes in the narrow and wide sections, respectively. Intrinsically, for a strip waveguide well-supported TE mode, the effective index of TM mode is smaller than that of TE mode, and thereby once Eq. (1) is satisfied, Eq. (2) is also satisfied. Thus, the design process flow can be as follows: (1) use Bragg reflection regime condition to roughly estimate parameters of the photonic crystal; (2) simulate the k - ω diagrams for both TE and TM modes by the use of 3D FDTD; and (3) calculate the transmission responses for both TE and TM modes to further check the design. In Ref. [71], a measured extinction ratio of 40 dB was obtained with a period number of 40.

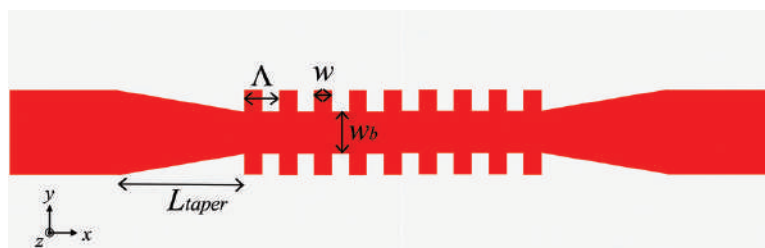


Figure 13. Schematic of a TM-pass polarizer assisted by 1D photonic crystals.

Adapting the same mechanism discussed above, higher-order mode pass filters have been demonstrated on a silicon wafer in Ref. [72], which are building blocks for mode-division multiplexing (MDM) systems. A 15.0- μm -long TE1 mode pass filter exhibits an extinction ratio of ~ 48 dB and an insertion loss of ~ 1.8 dB at 1550 nm.

6. Conclusion

1D photonic crystals have been well developed in silicon photonics and other material platforms as well. Three operating regimes allow 1D photonic crystals to be exploited in many different functional photonic devices with compact footprints. In diffraction regime, light beam can be diffracted into different directions by controlling configuration of photonic crystals in terms of pitch, duty cycle and effective index. In sub-wavelength regime, material refractive index, birefringence, and dispersion can be simply controlled by lithographic patterning to enable new design methods that lead to high-performance photonic devices. Propagation constant is proportional to operating wavelength and effective index in Bragg reflection regime. Thus, many wavelength-, mode-, and polarization-sensitive devices have been demonstrated with the assistance of Bragg gratings. In all these three regimes, when the operating wavelength range is fixed, the sub-wavelength gratings require tightest lithography process control that is high patterning resolution and is the most versatile one. Normally, sub-wavelength gratings are fabricated by electron-beam lithography which is not only expensive but also not suitable for mass production. And, the patterning resolution of DUV stepper lithography widely used in CMOS technology is not enough for accurately controlling sub-wavelength gratings. Therefore, continuing improvement in advanced lithography techniques is one important way to realize large-volume integration of sub-wavelength gratings with other electronic and photonic devices.

Author details

Liangshun Han

Address all correspondence to: liangshunhan@gmail.com

University of California, San Diego, USA

References

- [1] Pantouvaki M et al. 50Gb/s Silicon Photonics Platform for Short-Reach Optical Interconnects, in Optical Fiber Communication Conference, OSA Technical Digest (online) (Optical Society of America, 2016), paper Th4H.4
- [2] Heck MJR, Bowers JE. Energy efficient and energy proportional optical interconnects for multi-Core processors: Driving the need for on-Chip sources. IEEE Journal of Selected Topics in Quantum Electronics. Jul 2014;20(4):332-343

- [3] Yu R et al. A scalable silicon photonic chip-scale optical switch for high performance computing systems. *Optics Express*. Dec 2013;**21**(26):32655
- [4] Yang T et al. Experimental observation of optical differentiation and optical Hilbert transformation using a single SOI microdisk chip. *Scientific Reports*. Feb 2014;**4**:3960
- [5] Juan-Colás J, Parkin A, Dunn KE, Scullion MG, Krauss TF, Johnson SD. The electrophotonic silicon biosensor. *Nature Communications*. Sep 2016;**7**:12769
- [6] De Vos K, Bartolozzi I, Schacht E, Bienstman P, Baets R. Silicon-on-insulator microring resonator for sensitive and label-free biosensing. *Optics Express*. 2007;**15**(12):7610
- [7] Chen S et al. Electrically pumped continuous-wave III–V quantum dot lasers on silicon. *Nature Photonics*. Mar 2016;**10**(5):307-311
- [8] Duan G-H et al. Hybrid III–V on silicon lasers for photonic integrated circuits on silicon. *IEEE Journal of Selected Topics in Quantum Electronics*. Jul 2014;**20**(4):158-170
- [9] Huolei W, Kim D, Harfouche M, Satyan N, Rakuljic G, and Yariv A. Narrow-Linewidth Oxide-Confined Heterogeneously Integrated Si/III-V Semiconductor Laser, in Conference on Lasers and Electro-Optics, OSA Technical Digest (online) (Optical Society of America, 2017), paper AM2B.2
- [10] Thomson DJ et al. 50-Gb/s silicon optical modulator. *IEEE Photonics Technology Letters*. Feb 2012;**24**(4):234-236
- [11] Xiao X et al. High-speed, low-loss silicon Mach–Zehnder modulators with doping optimization. *Optics Express*. Feb 2013;**21**(4):4116
- [12] Novack A et al. Germanium photodetector with 60 GHz bandwidth using inductive gain peaking. *Optics Express*. Nov 2013;**21**(23):28387
- [13] Lu L et al. 16 × 16 non-blocking silicon optical switch based on electro-optic Mach-Zehnder interferometers. *Optics Express*. May 2016;**24**(9):9295
- [14] Tanizawa K et al. Ultra-compact 32 × 32 strictly-non-blocking Si-wire optical switch with fan-out LGA interposer. *Optics Express*. Jun 2015;**23**(13):17599
- [15] Sun C et al. Single-chip microprocessor that communicates directly using light. *Nature*. Dec 2015;**528**(7583):534-538
- [16] Joannopoulos JD, Johnson SG, Winn JN, Meade RD. *Photonic Crystals: Molding the Flow of Light*. Princeton, NJ: Princeton University Press; 2008
- [17] Rytov SM. Electromagnetic properties of a finely stratified medium. *Journal of Experimental and Theoretical Physics*. 1956;**2**(3):466
- [18] Tamir T, Peng ST. Analysis and design of grating couplers. *Applied Physics*. 1977;**14**(3): 235-254
- [19] Chrostowski L, Hochberg M. *Silicon Photonics Design*. United Kingdom: Cambridge University Press; 2015

- [20] Vermeulen D et al. High-efficiency fiber-to-chip grating couplers realized using an advanced CMOS-compatible silicon-on-insulator platform. *Optics Express*. Aug 2010; **18**(17):18278-18283
- [21] Taillaert D et al. Grating couplers for coupling between optical fibers and Nanophotonic waveguides. *Japanese Journal of Applied Physics*. 2006;**45**(8R):6071
- [22] Van Laere F et al. Compact focusing grating couplers for silicon-on-insulator integrated circuits. *IEEE Photonics Technology Letters*. 2007;**19**(23):1919-1921
- [23] Waldhäusl R, Schnabel B, Dannberg P, Kley E-B, Bräuer A, Karthe W. Efficient coupling into polymer waveguides by gratings. *Applied Optics*. Dec 1997;**36**(36):9383-9390
- [24] Van Laere F et al. Compact and highly efficient grating couplers between optical fiber and nanophotonic waveguides. *Journal of Lightwave Technology*. 2007;**25**(1):151-156
- [25] Alonso-Ramos C, Zavargo-Peche L, Ortega-Moñux A, Halir R, Molina-Fernández I, Cheben P. Polarization-independent grating coupler for micrometric silicon rib waveguides. *Optics Letters*. Sep 2012;**37**(17):3663-3665
- [26] Zaoui WS et al. Bridging the gap between optical fibers and silicon photonic integrated circuits. *Optics Express*. Jan 2014;**22**(2):1277-1286
- [27] Taillaert D, Bienstman P, Baets R. Compact efficient broadband grating coupler for silicon-on-insulator waveguides. *Optics Letters*. Dec 2004;**29**(23):2749-2751
- [28] Mekis A et al. A grating-coupler-enabled CMOS photonics platform. *IEEE Journal of Selected Topics in Quantum Electronics*. 2011;**17**(3):597-608
- [29] Chen X, Li C, Fung CKY, Lo SMG, Tsang HK. Apodized waveguide grating couplers for efficient coupling to optical fibers. *IEEE Photonics Technology Letters*. 2010;**22**(15):1156-1158
- [30] Ding Y, Ou H, Peucheret C. Ultrahigh-efficiency apodized grating coupler using fully etched photonic crystals. *Optics Letters*. 2013;**38**(15):2732-2734
- [31] Chen X, Tsang HK. Polarization-independent grating couplers for silicon-on-insulator nanophotonic waveguides. *Optics Letters*. 2011;**36**(6):796-798
- [32] Cheng Z, Tsang HK. Experimental demonstration of polarization-insensitive air-cladding grating couplers for silicon-on-insulator waveguides. *Optics Letters*. 2014; **39**(7):2206-2209
- [33] Chen X, Xu K, Cheng Z, Fung CKY, Tsang HK. Wideband subwavelength gratings for coupling between silicon-on-insulator waveguides and optical fibers. *Optics Letters*. 2012;**37**(17):3483-3485
- [34] Qin K et al. High efficiency and broadband two-dimensional blazed grating coupler with fully etched triangular holes. *Journal of Lightwave Technology*. 2012;**30**(14):2363-2366
- [35] Cheben P et al. Refractive index engineering with subwavelength gratings for efficient microphotonic couplers and planar waveguide multiplexers. *Optics Letters*. 2010;**35**(15): 2526-2528

- [36] Cheben P, Xu D-X, Janz S, Densmore A. Subwavelength waveguide grating for mode conversion and light coupling in integrated optics. *Optics Express*. 2006;**14**(11):4695-4702
- [37] Almeida VR, Panepucci RR, Lipson M. Nanotaper for compact mode conversion. *Optics Letters*. 2003;**28**(15):1302-1304
- [38] Bock PJ et al. Subwavelength grating periodic structures in silicon-on-insulator: A new type of microphotonic waveguide. *Optics Express*. 2010;**18**(19):20251-20262
- [39] Bock PJ et al. Sub-wavelength grating mode transformers in silicon slab waveguides. *Optics Express*. 2009;**17**(21):19120-19133
- [40] Ma Y et al. Ultralow loss single layer submicron silicon waveguide crossing for SOI optical interconnect. *Optics Express*. 2013;**21**(24):29374-29382
- [41] Chen CH, Chiu CH. Taper-integrated multimode-interference based waveguide crossing design. *IEEE Journal of Quantum Electronics*. 2010;**46**(11):1656-1661
- [42] Zhang Y, Hosseini A, Xu X, Kwong D, Chen RT. Ultralow-loss silicon waveguide crossing using Bloch modes in index-engineered cascaded multimode-interference couplers. *Optics Letters*. 2013;**38**(18):3608-3611
- [43] Bock PJ et al. Subwavelength grating crossings for silicon wire waveguides. *Optics Express*. 2010;**18**(15):16146-16155
- [44] Han L, Liang S, Zhu H, Zhang C, Wang W. A high extinction ratio polarization beam splitter with MMI couplers on InP substrate. *IEEE Photonics Technology Letters*. Apr 2015;**27**(7):782-785
- [45] Han L, Liang S, Zhu H, Qiao L, Xu J, Wang W. Two-mode de/multiplexer based on multimode interference couplers with a tilted joint as phase shifter. *Optics Letters*. Feb 2015;**40**(4):518
- [46] Han L, Liang S, Xu J, Qiao L, Zhu H, Wang W. Simultaneous wavelength- and mode-division (de)multiplexing for high-capacity on-chip data transmission link. *IEEE Photonics Journal*. Apr 2016;**8**(2):1-10
- [47] Soldano LB, Pennings ECM. Optical multi-mode interference devices based on self-imaging: Principles and applications. *Journal of Lightwave Technology*. 1995;**13**(4):615-627
- [48] Halir R, Roelkens G, Ortega-Moñux A, Wangüemert-Pérez JG. High-performance 90° hybrid based on a silicon-on-insulator multimode interference coupler. *Optics Letters*. 2011;**36**(2):178-180
- [49] Ortega-Monux A et al. High-performance multimode interference coupler in silicon waveguides with subwavelength structures. *IEEE Photonics Technology Letters*. 2011;**23**(19):1406-1408
- [50] Maese-Novo A et al. Wavelength independent multimode interference coupler. *Optics Express*. 2013;**21**(6):7033-7040

- [51] Halir R et al. Colorless directional coupler with dispersion engineered sub-wavelength structure. *Optics Express*. 2012;**20**(12):13470-13477
- [52] Cheng N-C, Ma Y-F, Fu P-H, Chin C-C, Huang D-W. Horizontal slot waveguides for polarization branching control. *Applied Optics*. 2015;**54**(3):436-443
- [53] Alam MZ, Aitchison JS, Mojahedi M. Polarization-independent hybrid plasmonic coupler for a silicon on insulator platform. *Optics Letters*. 2012;**37**(16):3417-3419
- [54] Xiao J, Liu X, Sun X. Design of polarization-independent optical couplers composed of three parallel slot waveguides. *Applied Optics*. 2008;**47**(14):2687-2695
- [55] Liu L, Deng Q, Zhou Z. Subwavelength-grating-assisted broadband polarization-independent directional coupler. *Optics Letters*. 2016;**41**(7):1648-1651
- [56] Han L et al. DBR laser with over 20 nm wavelength tuning range. *IEEE Photonics Technology Letters*. 2016:1-1
- [57] Han L et al. Electroabsorption-modulated widely tunable DBR laser transmitter for WDM-PONs. *Optics Express*. Dec 2014;**22**(24):30368
- [58] Zhang C, Liang S, Zhu H, Han L, Wang W. Multichannel DFB laser arrays fabricated by upper SCH layer SAG technique. *IEEE Journal of Quantum Electronics*. Feb 2014;**50**(2): 92-97
- [59] Hou L, Xu J, Eddie I, Han L, Zhu H, and Marsh J. DWDM Source Based on Monolithic Side-Wall Sample Grating DFB Laser Array, in Conference on Lasers and Electro-Optics, OSA Technical Digest (2016) (Optical Society of America, 2016), paper SW4M.1
- [60] Kashyap R. *Fiber Bragg Grating*. San Diego: Academic Press; 1999
- [61] Jewell JL, Harbison JP, Scherer A, Lee YH, Florez LT. Vertical-cavity surface-emitting lasers: Design, growth, fabrication, characterization. *IEEE Journal of Quantum Electronics*. 1991;**27**(6):1332-1346
- [62] Roth JE, Palermo S, Helman NC, Bour DP, Miller DA, and Horowitz M. 1550nm Optical Interconnect Transceiver with Low Voltage Electroabsorption Modulators Flip-Chip Bonded to 90nm CMOS, in Optical Fiber Communication Conference and Exposition and The National Fiber Optic Engineers Conference, OSA Technical Digest Series (CD) (Optical Society of America, 2007), paper JThA38
- [63] Kreissl J, Bornholdt C, Gaertner T, Moerl L, Przyrembel G, Rehbein W. 1550 nm flip-chip compatible electroabsorption-modulated laser with 40 Gb/s modulation capability. In: IPRM 2011 – 23rd International Conference on Indium Phosphide and Related Materials (IEEE, 2011); pp. 1-4
- [64] Roelkens G, Brouckaert J, Van Thourhout D, Baets R, Nötzel R, Smit M. Adhesive bonding of InP/InGaAsP dies to processed silicon-on-insulator wafers using DVS-bis-Benzocyclobutene. *Journal of the Electrochemical Society*. 2006;**153**(12):G1015

- [65] Liang D, Roelkens G, Baets R, Bowers JE. Hybrid integrated platforms for silicon photonics. *Materials (Basel)*. 2010;**3**(3):1782-1802
- [66] Tao L et al. 4- λ InGaAsP-Si distributed feedback evanescent lasers with varying silicon waveguide width. *Optics Express*. Mar 2014;**22**(5):5448
- [67] Dai D, Bowers JE. Novel concept for ultracompact polarization splitter-rotator based on silicon nanowires. *Optics Express*. May 2011;**19**(11):10940
- [68] Alam MZ, Aitchison JS, Mojahedi M. Compact and silicon-on-insulator-compatible hybrid plasmonic TE-pass polarizer. *Optics Letters*. 2012;**37**(1):55-57
- [69] Avrutsky I. Integrated optical polarizer for silicon-on-insulator waveguides using evanescent wave coupling to gap plasmon-polaritons. *IEEE Journal of Selected Topics in Quantum Electronics*. 2008;**14**(6):1509-1514
- [70] Dai D, Wang Z, Julian N, Bowers JE. Compact broadband polarizer based on shallowly-etched silicon-on-insulator ridge optical waveguides. *Optics Express*. 2010;**18**(26):27404-27415
- [71] Guan X, Chen P, Chen S, Xu P, Shi Y, Dai D. Low-loss ultracompact transverse-magnetic-pass polarizer with a silicon subwavelength grating waveguide. *Optics Letters*. 2014;**39**(15):4514-4517
- [72] Guan X, Ding Y, Frandsen LH. Ultra-compact broadband higher order-mode pass filter fabricated in a silicon waveguide for multimode photonics. *Optics Letters*. 2015;**40**(16):3893-3896

We are IntechOpen, the world's leading publisher of Open Access books Built by scientists, for scientists

6,300

Open access books available

171,000

International authors and editors

190M

Downloads

Our authors are among the

154

Countries delivered to

TOP 1%

most cited scientists

12.2%

Contributors from top 500 universities



WEB OF SCIENCE™

Selection of our books indexed in the Book Citation Index
in Web of Science™ Core Collection (BKCI)

Interested in publishing with us?
Contact book.department@intechopen.com

Numbers displayed above are based on latest data collected.
For more information visit www.intechopen.com



Liquid Crystals for Responsible Photonic Crystals

Sunnam Kim and Seiji Kurihara

Additional information is available at the end of the chapter

<http://dx.doi.org/10.5772/intechopen.72654>

Abstract

The photonic crystals (PCs) exhibit photonic band gap (PBG), inhibiting specific wavelength of light decided by structural periodicity. PCs are a new class of periodic dielectric media that can provide novel ways to manipulate and control light. Researchers have recently devoted extensive efforts to fabricating PCs with controlled symmetry, size, and defects on a large scale and tuning of PBG. Liquid crystalline (LC) materials exhibiting self-organization, phase transition, and molecular orientation behaviors in response to external stimuli are attracting significant attention for the bottom-up nanofabrication and tuning of advanced photonic materials and devices. Here, we will introduce self-organization of PCs from LCs and photoswitching mechanism of PBG based on phase transition and anisotropic orientation of LCs.

Keywords: self-organization, molecular orientation, liquid crystal, azobenzene, light response, photonic band gap

1. Introduction

The structural coloration is basically caused by interaction between light and periodic nanostructured-materials, and light absorption with dyes or pigments is not required for the structural coloration. One can find structural coloration of various materials in nature, and the structural colors are iridescent and very durable, for example, opal, peacock wings, and so on. Recently, there is an increasing interest in developing bioinspired nanostructures with controlled symmetry, size, and defects on a large scale for photonic crystals (PCs) [1–7]. Generally, the fabrication processes are divided into bottom-up and top-down methods. The top-down methods are mostly based on lithography-related techniques, which are expensive and requiring high technology [8–11]. The bottom-up methods are primarily about the self-assembly of component units such as emulsions, colloidal particles, and block copolymers [12–16].

Liquid crystalline (LC) materials are attracting significant interest on the bottom-up nanofabrication of advanced photonic materials and devices with unique configuration and novel tuning mechanism. LCs undoubtedly represent such a marvelous dynamic system based on molecular reorientation behavior affecting macroscopic properties [17–19]. On the other hand, the responsiveness of LCs to various stimuli such as temperature, light, mechanical force, and electric and magnetic fields as well as chemical and electrochemical reactions can attribute to fascinating tunability of photonic band gap (PBG) in the periodic nanostructure, which provides numerous opportunities in all-optical integrated circuits and next-generation communication system. Here, several examples of self-organized LC nanostructures are introduced, and fabrication of three-dimensional (3D) PCs containing azobenzene LC molecules and photoswitching of PBG are discussed.

2. Self-organized PCs and PBG tuning based on LCs

2.1. Self-organized LC nanostructures

We introduce several examples for the fabrication methods of precisely constructing of PCs using self-organized LC nanostructures of cholesteric LC (ChLC), LC blue phase, and holographic polymer-dispersed LC.

2.1.1. Cholesteric LC

Dissolving a chiral compound in a nematic LC causes helix formation, resulting in the selective reflection of circular light corresponding to the helical pitch and helical sense. The pitch, the distance over which the director field rotates by 2π radians, is sensitive to external stimuli such as temperature, light, electric field, and mechanical stress [20–25]. Kurihara et al. have reported on the photochemical change in transparency as well as the selective reflection of a cholesteric LC (ChLC) resulting from the photoisomerization of a chiral azobenzene compound doped in a host nematic LC [26–31]. It is based on the photochemical change in helical twisting power (HTP) of the chiral azobenzene compounds under irradiation of UV and visible light. A combination of a rigid chiral diol core and azobenzene group led to larger photochemical changes in HTP, resulting in a reversible change of selective reflection over whole range of visible region with faster photochemical switching as shown in **Figure 1**. HTPs of the chiral azobenzene compounds increased or decreased by UV light, and the color change of reflection light was seen even with naked eyes.

On the other hand, Mušević et al. developed ChLC microdroplets, in which the arrangement of ChLC molecules was with parallel anchoring of the LC molecules at the surface. The helical structure of the LC originates from the center of the droplet and gives rise to concentric shells of constant refractive index. The introduction of chirality in ChLCs in the spherical shape resulted in the formation of a multilayered spherical Bragg resonator with an alternating periodic refractive index [32]. This dielectric structure is optically equivalent to the well-known Bragg-onion optical microcavity. In addition, Li et al. reported photoresponsive ChLC droplets with large helical twisting power [33].

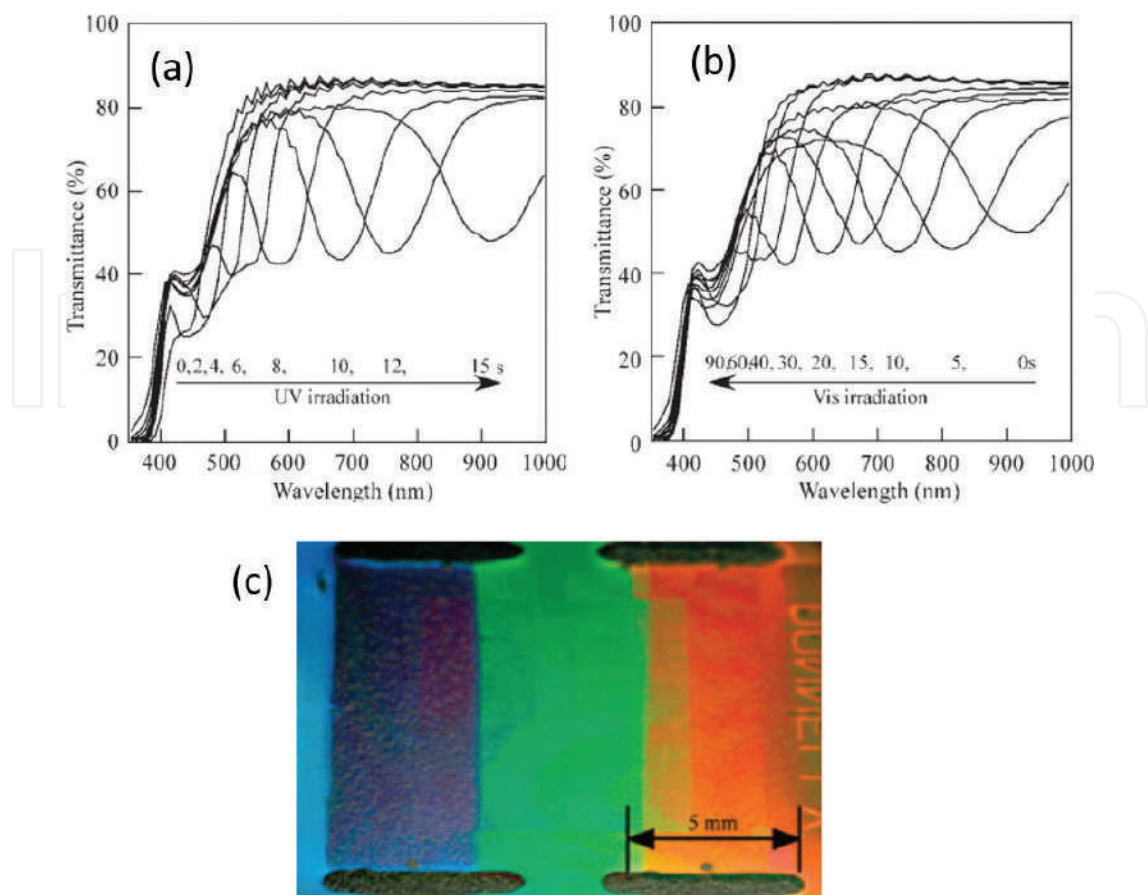


Figure 1. Changes in the selective reflection of the ChLC after UV irradiation (a) and visible light (b) irradiation at 25°C. And the photograph (c) of color change of the ChLC by varying UV irradiation time 0 s (left), 4 s (middle), and 10 s (right). [31] Copyright 2005, Wiley-VCH.

2.1.2. LC blue phase

Blue phases (BPs) are among the most fascinating photonic nanostructures in the area of LCs [34]. They are known to self-organize into the 3D frustrated nanostructures, which originate from the competition between the packing topology and chiral forces. The periodic nanostructures are self-organized from the so-called double-twisted cylinders that are usually stabilized by the formation of defects or disclinations. As the 3D PCs, BPs feature remarkable bandgap tunability over an extensive spectrum in response to various external stimuli such as temperature [35, 36], mechanical strength [37], electric field [38], and light [39–41]. The spectral band gap position of selective reflection can be readily predetermined by varying the chiral fraction of BP mixtures. However, BPs have received increasing attentions especially in recent years, but the reflection wavelength tuning is usually quite narrow. The ability to dynamically tune the photonic bandgap in cubic BPs across a wide wavelength range is highly desirable. Effort to improve the instability and irreversibility of BPs has been made with polymer-stabilized structure [18] and incorporation of unusual bent-core mesogen [42].

2.1.3. Holographic polymer-dispersed LC

Holographic polymer-dispersed liquid crystal (H-PDLC) materials belong to a phase separation material system where the LCs can form droplets, of controllable sizes, that are phase-separated from the polymer-rich regions during the photopolymerization process. Interestingly, it has enabled the in situ fast one-step fabrication of self-organized PCs. The control of the bandwidth of the reflection resonance, related to the light intensity and spatial porosity distributions, was investigated to optimize the optical performance.

For example, Cartwright et al. reported a graded reflection grating based on the H-PDLC material system [43, 44]. An obvious rainbow-colored reflection was observed from the same viewing angle by a modification to this standard configuration where the triangular prism is replaced with a cylindrical lens. Modified optical setup is based on a cylindrical lens to generate a graded holographic interference pattern along the x-axis from the incident and reflected beams. It is expected to compact graded PBG structures for linear variable optical filters.

The marriage of holography and self-organized LC materials is highly expected to produce a diverse range of novel 1D, 2D, and 3D nanostructures for various applications in electro-optical filters, wavelength division multiplexer, free-space optical switches, information display devices, and so on [45–49].

2.2. PBG tuning of 3D photonic crystals

Three-dimensional PCs such as opal and inverse opal structure can be easily prepared by colloidal self-assembly approach. The fabrication of inverse opal structure infiltrated by azobenzene LC molecules for 3D PCs and the mechanism of photoswitching of PBG are described.

For 3D PCs, the reflection wavelength (λ) under normal incident condition is expected by equation of Bragg diffraction as follows [50]

$$\lambda = 2\sqrt{\frac{2}{3}}d\sqrt{n_{\text{sphere}}^2f + n_{\text{void}}^2(1-f)} \quad (1)$$

where d is the diameter of the sphere, n_{sphere} and n_{void} are the refractive indices of the sphere and the medium in the voids of opal, respectively, and f is the volume fraction of the sphere. In this way, the peak wavelength can be roughly tuned by two approaches: either by control of the diameter of the sphere or by control of the refractive index. If one can control photochemically phase transition or birefringence of LCs in 3D PCs, they will be candidates for applications to optical devices such as display and memory.

On the other hand, light among various promising stimuli shows distinct and significant advantages due to its spatial, remote, and temporal controllability. It is also noteworthy that the light sources with different wavelength, intensity, and polarization are readily accessible. Photocontrol of chemical and physical functions of various molecular systems has been studied vigorously using photochemical configurational change of azobenzene derivatives [51–54]. The photochromism of azobenzene and its derivatives due to cis-trans isomerization has been widely investigated. For PC containing azobenzene molecules, ‘photochemical

phase transition' between the alignment phase and isotropic phase, or 'photoinduced optical anisotropy' based on photoselective reorientation behavior is very useful parameter for self-organization and optical photonic crystal switching. Here, fabrication of three-dimensional (3D) PC containing azobenzene molecules and photoswitching of PBG are discussed.

2.2.1. PBG tuning by phase transition change

Three-dimensional PCs such as opal and inverse opal structure can be infiltrated with stimuli-responsive materials, thus enabling PBG tuning. Kubo et al. reported on the drastic change in optical properties for the inverse opal structure containing low molar mass LCs, by taking advantage of the nematic-isotropic phase transition [50]. It is based on change in the light scattering intensity between LC phase and isotropic phase.

SiO₂ inverse opal template could be fabricated by infiltration of SiO₂ spheres into the voids of polystyrene (PS) opal film and calcination of PS as shown in **Figure 2**. When SiO₂ inverse opal film infiltrated with 4-cyano-4'-pentybiphenyl (5CB), the reflection spectra of the LC-infiltrated inverse opal film were changed with increase in the temperature as shown in **Figure 3**. In the initial state at 25°C, 5CB is in the nematic phase and the film is white due to light scattering. The reflection has two weak peaks. With the gradual temperature rise, the positions of the peaks shifted slowly and a distinct peak at around 610 nm, which is derived

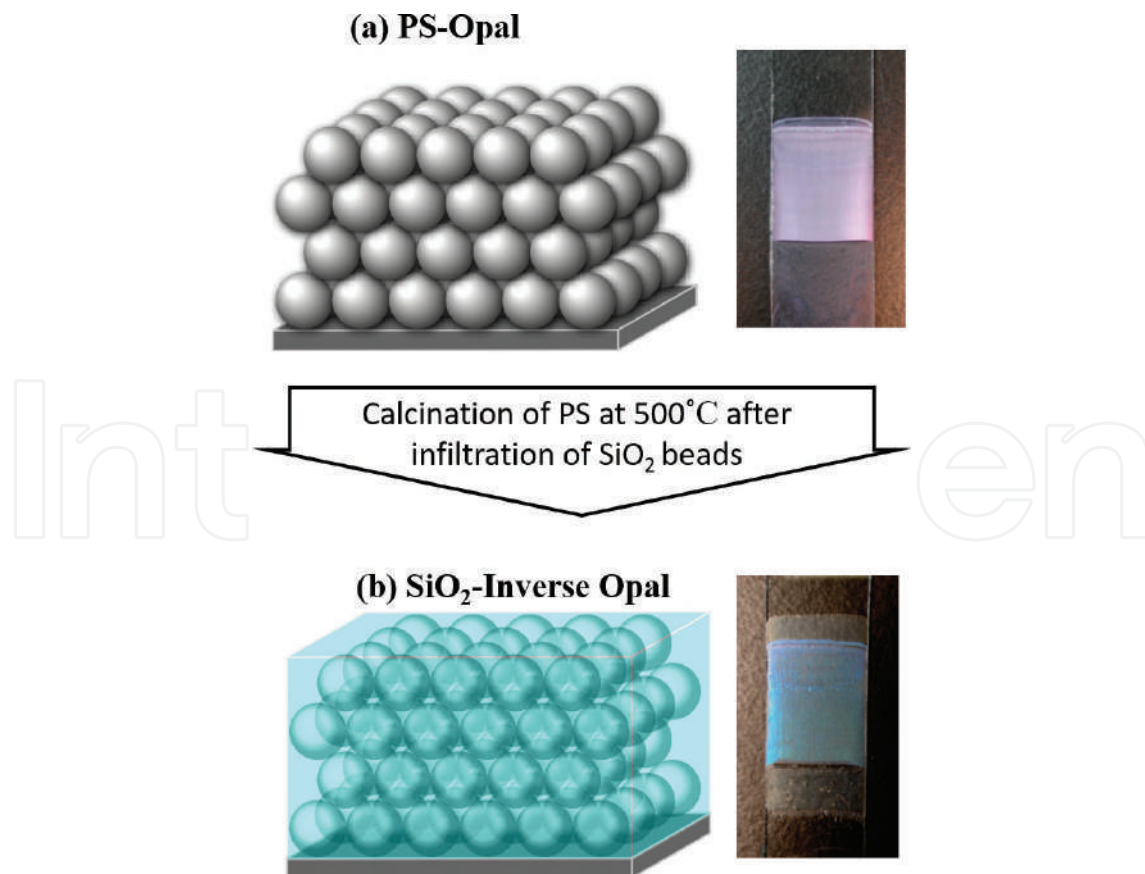


Figure 2. Schematic of PS opal (a) and SiO₂ inverse opal (b) structures and their photographs.

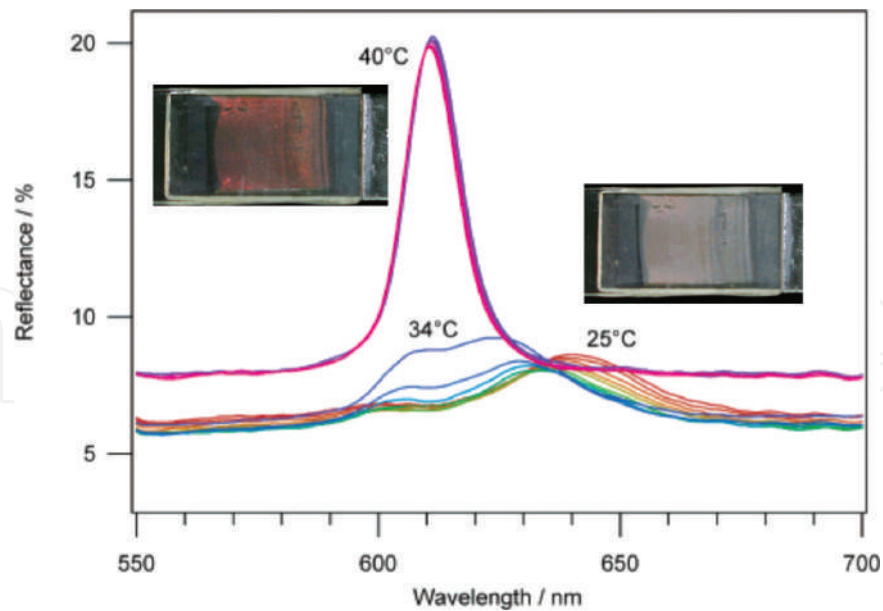


Figure 3. Reflection spectra of SiO₂ inverse opal film infiltrated with 5CB at the temperature from 25°C to 40°C [50]. Reproduced. Copyright 2004, American Chemical Society.

from PBG, appeared rapidly at the phase transition temperature into the isotropic phase at 40°C. The color of film becomes red. This result shows that switching of the optical properties can be realized due to a phase transition of the LCs, leading to thermos-tunable PCs.

Kubo et al. also reported the photoswitching of reflection for SiO₂ inverse opal film infiltrated with photo-response azobenzene containing LC mixture [55]. By UV light, a reflection peak increased rapidly and then saturated, indicating appearance of PBG. The trigger for this drastic change was the trans-cis photoisomerization of the azobenzene derivatives in the films. The excitation of the π - π^* transition of azobenzene molecules at around 360 nm results in a transformation from trans to cis isomers. The photoinduced cis form of azobenzene group has a bent shape and hence tends to disorganize the phase structure of nematic LCs.

The observed change could be reversed to the original state, decrease of reflectance, by irradiating with visible light. The recovery was induced by cis-trans photoisomerization, followed by a phase transition from the isotropic to the nematic phase under visible light (436 nm). Such a switching effect could also be observed in transmission spectra. It is supposed due to the fact that the LC molecules in the nematic phase in the spheroidal voids are aligned parallel to the void surfaces, but the orientation is completely random among spheres. It is similar to the phenomena observed for polymer-dispersed liquid crystal (PDLC). On the other hand, when the LC was transformed into an isotropic phase by UV light, the anisotropy in the dielectric constant disappeared. That is, the dielectric constant of the LC in all of the spheroidal voids became the same, and hence, a reflection peak due to Bragg diffraction appears [56–58]. On the basis of this scenario, dynamic change in the optical properties was observed repeatedly by alternating irradiation with UV and visible light. It was completely reversible, exhibiting good stability and reproducibility during the light irradiation cycle as shown in **Figure 4**.

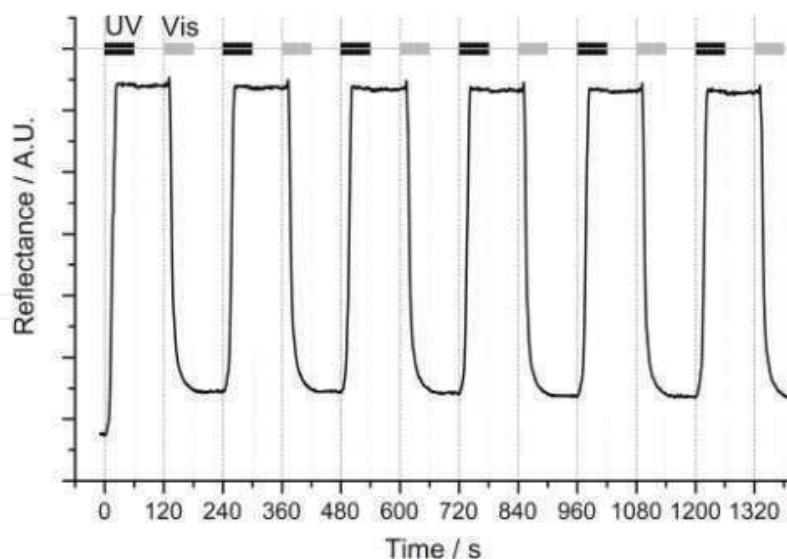


Figure 4. Time-dependent change in the reflectance of 5CB/azobenzene LC mixture-infiltrated inverse opal film at 603 nm by UV and visible light irradiation. The black bars show the periods for the irradiation of UV light (<400 nm), and the gray bars show the periods for irradiation of visible light (436 nm). For other periods, the sample was kept in the dark [58]. Copyright 2002, American Chemical Society.

2.2.2. PBG tuning by molecular reorientation

For low-molar-mass LC-infiltrated inverse opal film as mentioned in the previous section, the stability of the switched state was not enough although the photoswitching was reversible. It is due to the thermal back reaction of the azobenzene compound and fluidity of the low-molar-mass LC. In contrast with low-molar-mass LCs, polymeric LCs are well known to show excellent storage stability. Kurihara et al. reported the stable and reversible shift of the Bragg diffraction band for SiO_2 inverse opal structure infiltrated with 4,4'-methoxy hexyloxy azobenzene polymethacrylate, PAz (schematic molecular structure is shown in **Figure 5**), and reflection change were investigated when irradiation of linearly polarized light (LPL) and circularly polarized light (CPL) of Ar + laser ($\lambda = 488 \text{ nm}$) [59].

Photoisomerization behavior is demonstrated by absorption band change as shown in **Figure 6**. By UV light, trans-cis isomerization is induced, the absorption peak at 360 nm decreases, and the peak at 450 nm increases (**Figure 5(a)** and **(c)**). By irradiation of visible light, cis-trans photoisomerization is induced, and reverse changes in absorption spectra are induced (**Figure 6(b)** and **(d)**).

Anisotropic state of azobenzene compounds based on their molecular orientation can be controlled via reversible isomerization behavior by light and thermal stimuli [60–62]. Namely, alignment state of trans-form is perpendicular to the direction of polarized light (known as Weigert effect [20, 63–64]), and the alignment is destroyed by formation of cis-form.

The orientation state is evaluated by polarized absorption spectra and by birefringence, Δn , measurement. From angle dependence of absorbance at the peak of 360 nm to the polarized axis, orientation direction perpendicular to the polarized direction of induced LPL was demonstrated. When Δn is estimated by change in transmitted light of the azobenzene film

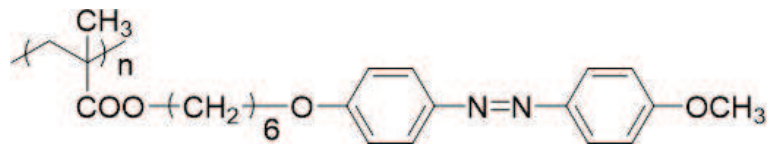


Figure 5. Schematic molecular structure of PAz.

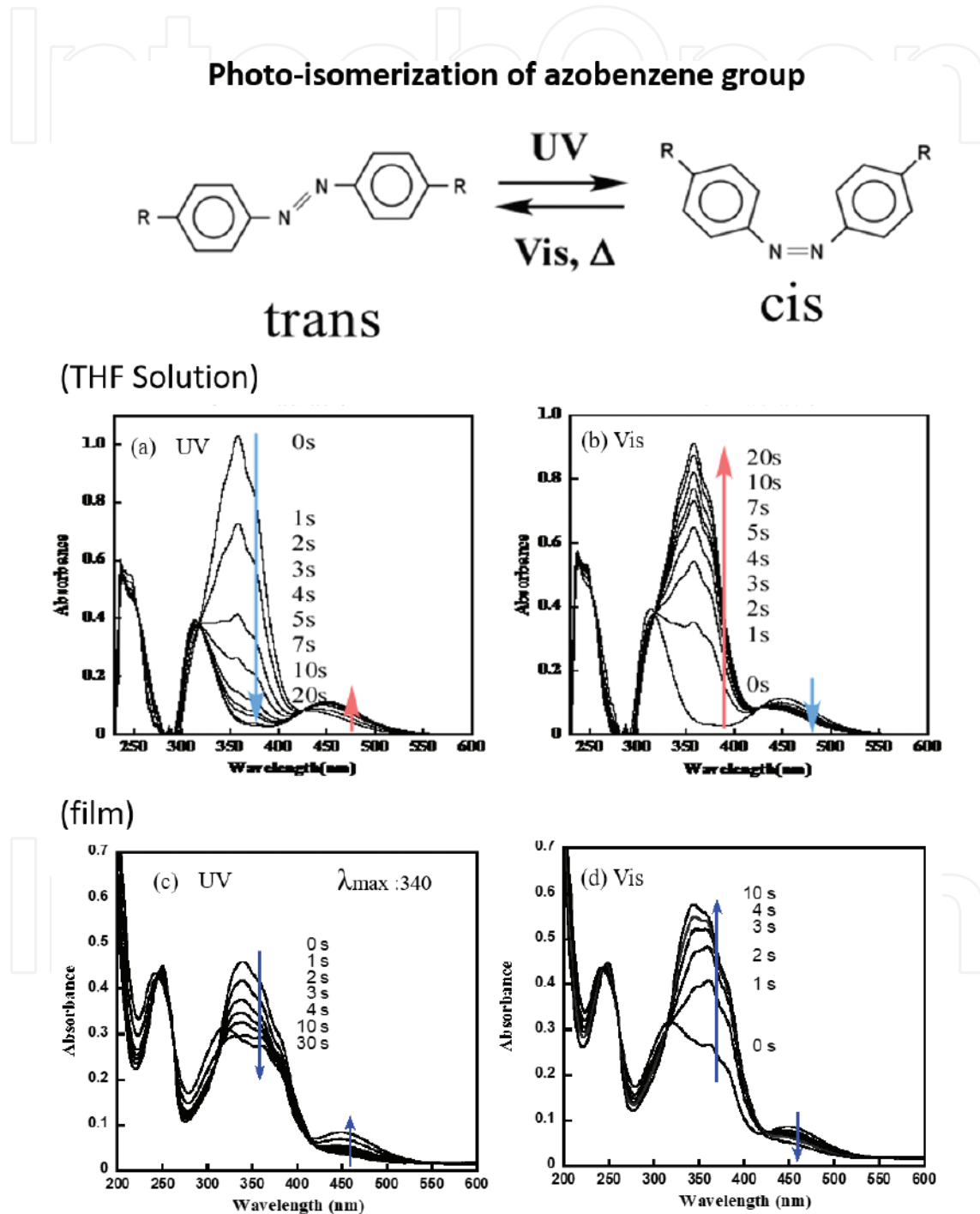


Figure 6. Changes in absorption spectra of PAz in THF after UV light (365 nm, 8 mW/cm²) (a) and visible light (436 nm, 60 mW/cm²) (b) irradiation. Changes in absorption spectra of PAz film irradiated UV light (365 nm, 10 mW/cm²) (c) and following visible light (436 nm, 58 mW/cm²) (d) at room temperature.

placed between two crossed polarizers, Δn of PAz was estimated to be 0.128, as shown in **Figure 7** [65].

Azobenzene polymer can be infiltrated into the SiO_2 inverse opal film by heating to melt. The pore diameter and volume fraction of SiO_2 inverse opal, d and f , were estimated by comparing wavelength of the reflection peaks of the SiO_2 inverse opal films infiltrated with various solvents with different refractive indices. For SiO_2 inverse opal film, $d = 278 \text{ nm}$ and $f = 0.118$, reflection spectra before and after injection of PAz are shown in **Figure 8**. The injection of PAz caused a shift of the reflection peak from 480 nm to 710 nm, because of an increase in the refractive index from 1.0 of air to 1.6 of PAz.

By LPL irradiation of light, reflection measured with polarizer parallel and perpendicular to the polarization direction of LPL is plotted in **Figure 9**. The reflection peaks depend on the irradiation time and polarization direction. By irradiation of a linearly polarized light at 488 nm (Ar + laser), azobenzene groups were aligned in the direction perpendicular to the polarization direction of the laser light.

After irradiation of LPL, reflection band shifted to longer wavelength with little shoulder at shorter wavelength. By observation with parallel and perpendicular polarizers, different two bands were respectively observed. The maximum wavelengths of the reflection bands at shorter and longer wavelength regions were 706 nm and 725 nm, respectively. Therefore, the refractive indices of PAz in the pores after the LPL irradiation, ordinary refractive index (n_o) and extraordinary refractive index (n_e), were estimated to be, respectively, 1.57 and 1.62 by using Bragg diffraction (Eq. (1)) with the parameters d (278 nm), f (0.118), and n_{SiO_2} (1.45). Namely, the photoinduced birefringence of PAz was 0.05 in the pores of SiO_2 inverse opal. It is less optical anisotropy comparing to solid film of PAz (0.13), indicating insufficient alignment

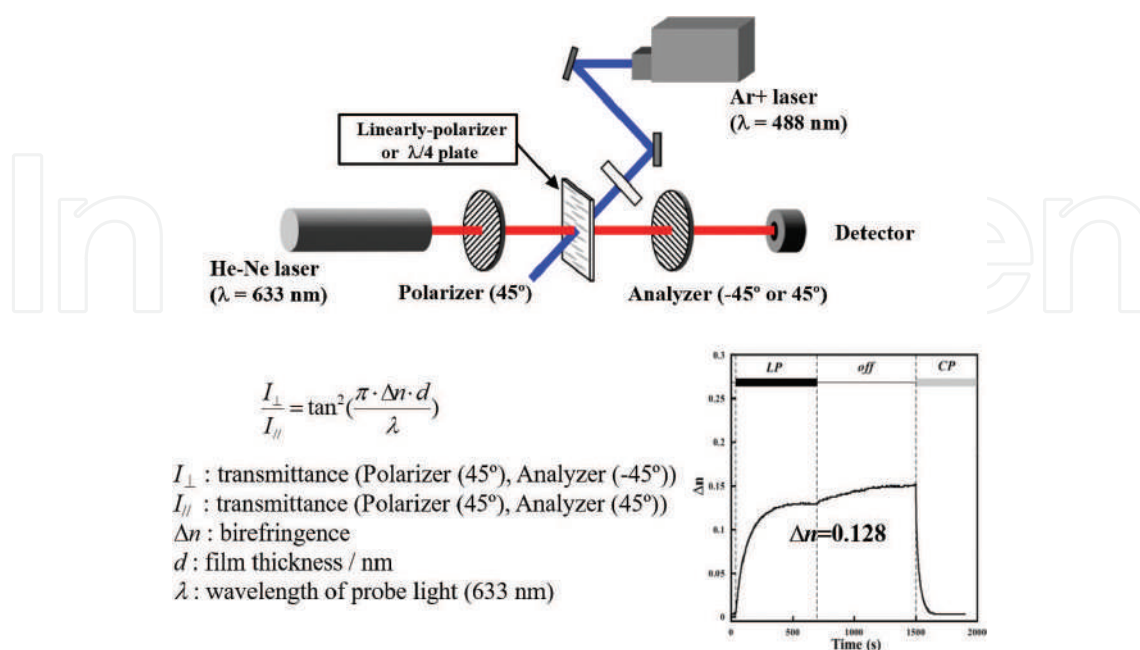


Figure 7. Schematic for birefringence measurement and the result of PAz.

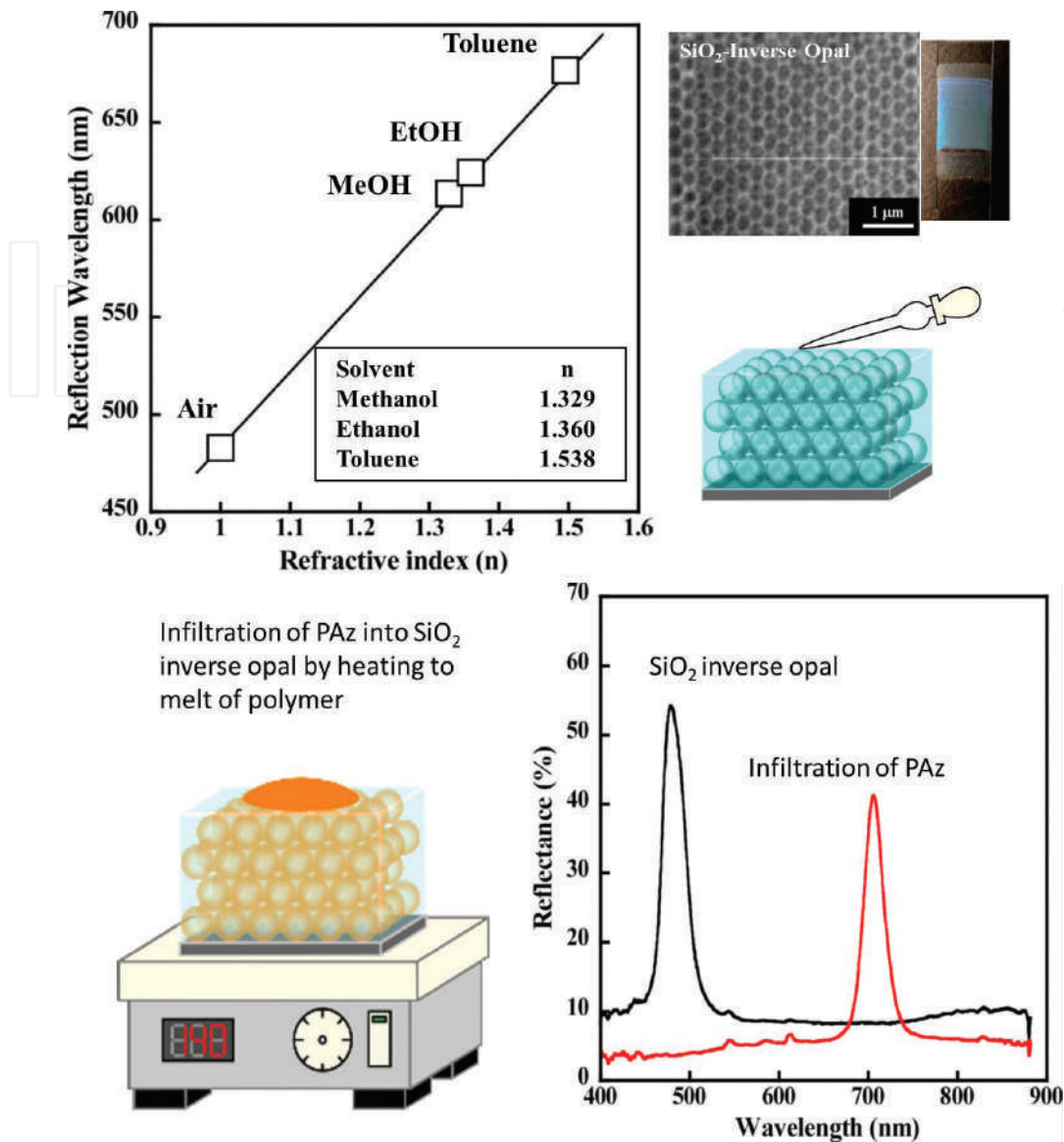


Figure 8. Plot of reflection wavelength change of SiO₂ inverse opal structure depending on solvents with various refractive indices (a) and reflection spectra before and after infiltration of PAz (b).

due to huge surface energy in the pores of SiO₂. In addition, reflection intensity decreased and increased by small and larger refractive index differences between PAz (1.57 and 1.62) and SiO₂ (1.45).

3. Conclusion

Optical properties of LCs represent the responsibility of external stimuli such as temperature, light, mechanical force, and electric and magnetic fields as well as chemical and electrochemical reactions, which are a driving force leading to dynamic change of materials from molecular level to macroscopic level. Dynamic system of LCs makes it a quite advantageous

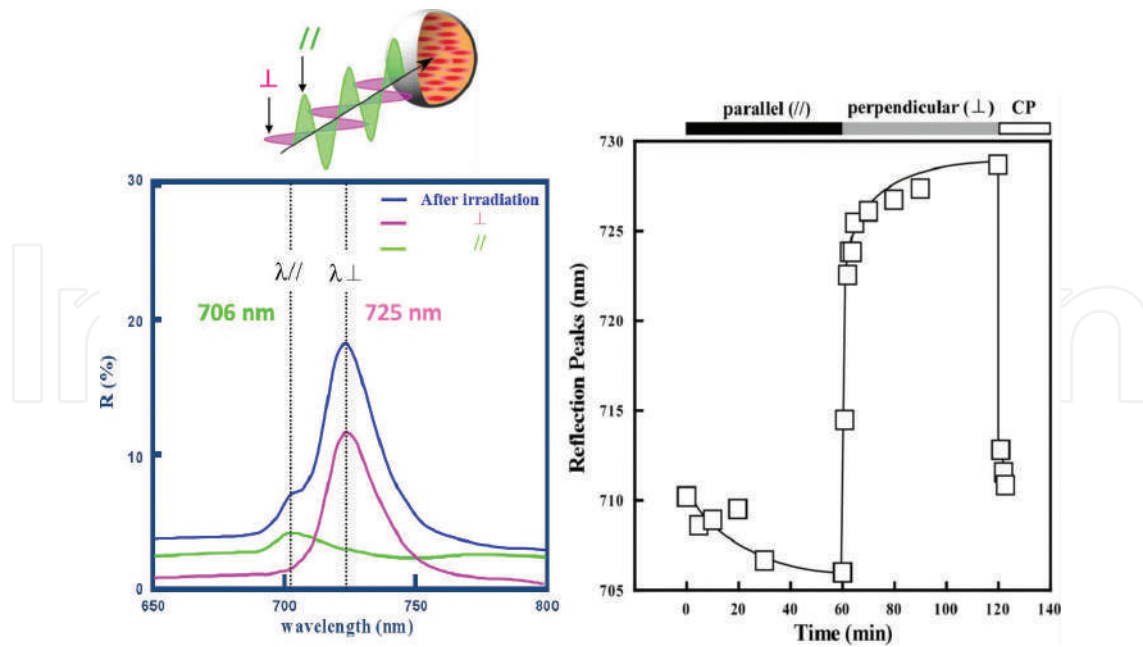


Figure 9. Reflection spectra of Paz-infiltrated SiO₂ film with parallel and perpendicular LPL irradiation of Ar + laser and plot of the wavelength of reflection peak [59].

approach toward bottom-up nanofabrication of photonic materials with novel tuning mechanism. In addition, the responsiveness to various stimuli can attribute to fascinating tunability of PBG, which provides numerous opportunities in all-optical integrated circuits and next-generation communication system.

Author details

Sunnam Kim* and Seiji Kurihara

*Address all correspondence to: sn-kim@kumamoto-u.ac.jp

Department of Applied Chemistry and Biochemistry, Kumamoto University, Kumamoto, Japan

References

- [1] Zan G, Wu Q. Biomimetic and bioinspired synthesis of nanomaterials/nanostructures. *Advanced Materials* (Deerfield Beach, Fla.). 2016;**28**:2099-2147
- [2] Pokroy B, Epstein AK, Persson-Gulda MCM, Aizenberg J. Fabrication of bioinspired actuated nanostructures with arbitrary geometry and stiffness. *Advanced Materials*. 2009;**21**:463-469

- [3] Pris AD, Utturkar Y, Surman C, Morris WG, Vert A, Zalyubovskiy S, et al. Towards high-speed imaging of infrared photons with bio-inspired nanoarchitectures. *Nature Photonics*. 2012;**6**:195-200. DOI: 10.1038/nphoton.2011.355
- [4] Bai L, Xie Z, Wang W, Yuan C, Zhao Y, Mu Z, et al. Bio-inspired vapor-responsive colloidal photonic crystal patterns by inkjet printing. *ACS Nano*. 2014;**8**:11094-11100
- [5] Ye B, Rong F, Gu H, Xie Z, Cheng Y, Zhao Y, et al. Bioinspired angle-independent photonic crystal colorimetric sensing. *Chemical Communications*. 2013;**49**:5331-5333
- [6] Hou J, Zhang H, Yang Q, Li M, Song Y, Jiang L. Bio-inspired photonic-crystal microchip for fluorescent ultratrace detection. *Angewandte Chemie International Edition*. 2014;**53**:5791-5795
- [7] Biró LP, Vigneron JP. Photonic nanoarchitectures in butterflies and beetles: Valuable sources for bioinspiration. *Laser & Photonics Reviews*. 2011;**5**:27-51
- [8] Campbell M, Sharp DN, Harrison MT, Denning RG, Turberfield AJ. Fabrication of photonic crystals for the visible spectrum by holographic lithography. *Nature*. 2000;**404**:53-56
- [9] Blanco A, Chomski E, Grabtchak S, Ibsate M, John S, Leonard SW, et al. Large-scale synthesis of a silicon photonic crystal with a complete three-dimensional bandgap near 1.5 micrometres. *Nature*. 2000;**405**:437-440
- [10] Deubel M, Freymann G von, Wegener M, Pereira S, Busch K, Soukoulis CM. Direct laser writing of three-dimensional photonic-crystal templates for telecommunications. *Nature Materials* 2004;**3**:444-447
- [11] Qi M, Lidorikis E, Rakich PT, Johnson SG, Joannopoulos JD, Ippen EP, et al. A three-dimensional optical photonic crystal with designed point defects. *Nature*. 2004;**429**:538-542
- [12] Hynninen A-P, Thijssen JHJ, Vermolen ECM, Dijkstra M, van Blaaderen A Self-assembly route for photonic crystals with a bandgap in the visible region. *Nature Materials* 2007;**6**:202-205
- [13] Jenekhe S, Chen X. Self-assembly of ordered microporous materials from rod-coil block copolymers. *Science*. 1999;**283**:372-375
- [14] Vlasov YA, Bo X-Z, Sturm JC, Norris DJ. On-chip natural assembly of silicon photonic bandgap crystals. *Nature*. 2001;**414**:289-293
- [15] Winfree E, Liu F, Wenzler LA, Seeman NC. Design and self-assembly of two-dimensional DNA crystals. *Nature*. 1998;**394**:539-544
- [16] Joannopoulos JD. Photonics: Self-assembly lights up. *Nature*. 2001;**414**:257-258
- [17] Gibbons WM, Shannon PJ, Sun S-T, Swetlin BJ. Surface-mediated alignment of nematic liquid crystals with polarized laser light. *Nature*. 1991;**351**:49-50
- [18] Kikuchi H, Yokota M, Hisakado Y, Yang H, Kajiyama T. Polymer-stabilized liquid crystal blue phases. *Nature Materials*. 2002;**1**:64-68

- [19] Shannon PJ, Gibbons WM, Sun ST. Patterned optical properties in photopolymerized surface-aligned liquid-crystal films. *Nature*. 1994;**368**:532-533
- [20] Ikeda T, Sasaki T, Ichimura K. Photochemical switching of polarization in ferroelectric liquid-crystal films. *Nature*. 1993;**361**:428-430
- [21] Kurihara S, Nomiyama S, Nonaka T. Photochemical control of the macrostructure of cholesteric liquid crystals by means of photoisomerization of chiral azobenzene molecules. *Chemistry of Materials*. 2001;**13**:1992-1997
- [22] Huang Y, Zhou Y, Doyle C, Wu S-T. Tuning the photonic band gap in cholesteric liquid crystals by temperature-dependent dopant solubility. *Optics Express*. 2006;**14**:1236-1242
- [23] Moreira M et al. Cholesteric liquid-crystal laser as an optic fiber-based temperature sensor. *Applied Physics Letters*. 2004;**85**:2691-2693
- [24] Baessler H, Laronge TM, Labes MM. Electric field effects on the optical rotatory power of a compensated cholesteric liquid crystal. *The Journal of Chemical Physics*. 1969;**51**:3213-3219
- [25] Finkelmann H, Kim ST, Munoz A, Palffy-Muhoray P, Taheri B. Tunable mirrorless lasing in cholesteric liquid crystalline elastomers. *Advanced Materials*. 2001;**13**:1069-1072
- [26] Kurihara S et al. Photo-tuning of lasing from a dye-doped cholesteric liquid crystals by photoisomerization of a sugar derivative having plural azobenzene groups. *Applied Physics Letters*. 2006;**88**:103121
- [27] Hatae Y, Moritsugu M, Ogata T, Kurihara S, Nonaka T. Photochemical modulation of the wavelength of lasing from a dye-doped cholesteric liquid crystal. *Molecular Crystals and Liquid Crystals*. 2005;**443**:87-94
- [28] Yoshioka T, Alam MZ, Ogata T, Nonaka T, Kurihara S. Photochemical tuning of the helical structure of cholesteric liquid crystals by photoisomerization of chiral azobenzenes, and their structural effects. *Liquid Crystals*. 2004;**31**:1285-1291
- [29] Yoshioka T, Ogata T, Zahangir AM, Nonaka T. Discontinuous change in the helical pitch of cholesteric liquid crystals by photoisomerization of a chiral azobenzene molecule. *Liquid Crystals*. 2004;**31**:15-19
- [30] Kurihara S, Yoshioka T, Zahangir A, Ogata T, Nonaka T. Preparation of composites of polymer liquid crystal/cholesteric liquid crystal and their photochemical switching and memory properties by photoisomerization of a chiral azobenzene molecule. *Journal of Applied Polymer Science*. 2004;**92**:2577-2580
- [31] Yoshioka T et al. Reversible-photon-mode full-color display by means of photochemical modulation of a helically cholesteric structure. *Advanced Materials*. 2005;**17**:1226-1229
- [32] Humar M, Muševič I. 3D microlasers from self-assembled cholesteric liquid-crystal microdroplets. *Optics Express*. 2010;**18**:26995-27003
- [33] Chen L et al. Photoresponsive monodisperse cholesteric liquid crystalline microshells for tunable omnidirectional lasing enabled by a visible light-driven chiral molecular switch. *Advanced Optical Materials*. 2014;**2**:845-848

- [34] Cao W, Muñoz A, Palffy-Muhoray P, Taheri B. Lasing in a three-dimensional photonic crystal of the liquid crystal blue phase II. *Nature Materials*. 2002;**1**:111-113
- [35] Hur S-T et al. Liquid-crystalline blue phase laser with widely tunable wavelength. *Advanced Materials*. 2013;**25**:3002-3006
- [36] Coles H, Pivnenko M. Liquid crystal 'blue phases' with a wide temperature range. *Nature*. 2005;**436**:997-1000
- [37] Castles F et al. Stretchable liquid crystal blue phase gels. *Nature Materials*. 2014;**13**:817-821
- [38] Lu S, Chien L. Electrically switched color with polymer-stabilized blue-phase liquid crystals. *Optics Letters*. 2010;**35**:562-564
- [39] Lin T-H et al. Red, green and blue reflections enabled in an optically tunable self-organized 3D cubic nanostructured thin film. *Advanced Materials*. 2013;**25**:5050-5054
- [40] Wang L et al. NIR light-directing self-organized 3D photonic superstructures loaded with anisotropic plasmonic hybrid nanorods. *Chemical Communications*. 2015;**51**:15039-15042
- [41] Chen X et al. Light-controllable reflection wavelength of blue phase liquid crystals doped with azobenzene-dimers. *Chemical Communications*. 2013;**49**:10097-10099
- [42] Lee M et al. Liquid crystalline blue phase I observed for a bent-core molecule and its electro-optical performance. *Journal of Materials Chemistry*. 2010;**20**:5813-5816
- [43] Liu K, Xu H, Hu H, Gan Q, Cartwright AN. One-step fabrication of graded rainbow-colored holographic photopolymer reflection gratings. *Advanced Materials*. 2012;**24**:1604-1609
- [44] Moein T et al. Holographic photopolymer linear variable filter with enhanced blue reflection. *ACS Applied Materials & Interfaces*. 2014;**6**:3081-3087
- [45] Coles H, Morris S. Liquid-crystal lasers. *Nature Photonics*. 2010;**4**:676-685
- [46] Jakubiak R, Bunning TJ, Vaia RA, Natarajan LV, Tondiglia VP. Electrically switchable, one-dimensional polymeric resonators from holographic photopolymerization: A new approach for active photonic bandgap materials. *Advanced Materials*. 2003;**15**:241-244
- [47] Escuti MJ, Qi J, Crawford GP. Tunable face-centered-cubic photonic crystal formed in holographic polymer dispersed liquid crystals. *Optics Letters*. 2003;**28**:522-524
- [48] He GS et al. Tunable two-photon pumped lasing using a holographic polymer-dispersed liquid-crystal grating as a distributed feedback element. *Applied Physics Letters*. 2003;**83**:2733-2735
- [49] Wu S, Fuh A. Lasing in photonic crystals based on dye-doped holographic polymer-dispersed liquid crystal reflection gratings. *Japanese Journal of Applied Physics*. 2005;**44**:977
- [50] Kubo S et al. Tunable photonic band gap crystals based on a liquid crystal-infiltrated inverse opal structure. *Journal of the American Chemical Society*. 2004;**126**:8314-8319

- [51] Shinkai S, Nakaji T, Nishida Y, Ogawa T, Manabe O. Photoresponsive crown ethers. 1. Cis-trans isomerism of azobenzene as a tool to enforce conformational changes of crown ethers and polymers. *Journal of the American Chemical Society*. 1980;**102**:5860-5865
- [52] Ogawa M. Preparation of a cationic azobenzene derivative-montmorillonite intercalation compound and the photochemical behavior. *Chemistry of Materials*. 1996;**8**:1347-1349
- [53] Seki T et al. Photochemical alignment regulation of a nematic liquid crystal by Langmuir-Blodgett layers of azobenzene polymers as "command surfaces". *Macromolecules*. 1989;**22**:3505-3506
- [54] Ikeda T, Tsutsumi O. Optical switching and image storage by means of azobenzene liquid-crystal films. *Science*. 1995;**268**:1873-1875
- [55] Kubo S et al. Control of the optical properties of liquid crystal-infiltrated inverse opal structures using photo irradiation and/or an electric field. *Chemistry of Materials*. 2005;**17**:2298-2309
- [56] Tarhan İİ, Watson GH. Photonic band structure of fcc colloidal crystals. *Physical Review Letters*. 1996;**76**:315-318
- [57] Park SH, Xia Y. Assembly of mesoscale particles over large areas and its application in fabricating tunable optical filters. *Langmuir*. 1999;**15**:266-273
- [58] Kubo S, Gu Z, Takahashi K, Ohko Y, Sato O, Fujishima A. Control of the optical band structure of liquid crystal infiltrated inverse opal by a photoinduced nematic-isotropic phase transition. *Journal of the American Chemical Society*. 2002;**124**:10950-10951
- [59] Kurihara S et al. Photoswitching properties of photonic band gap material containing azo-polymer liquid crystal. *European Polymer Journal*. 2007;**43**:4951-4960
- [60] Natansohn A, Rochon P. Photoinduced motions in azo-containing polymers. *Chemical Reviews*. 2002;**102**:4139-4176
- [61] Alam Z, Ohmachi T, Ogata T, Nonaka T, Kurihara S, Photoisomerization behavior and photoinduced surface relief gratings on azopolymer film by a monochromatic light irradiation. *Optical Materials*. 2006;**29**:365-370
- [62] Kim S, Ogata T, Kurihara S. Azobenzene-containing polymers for photonic crystal materials. *Polymer Journal*. 2017;**49**:407-412
- [63] Shishido A. Rewritable holograms based on azobenzene-containing liquid-crystalline polymers. *Polymer Journal*. 2010;**42**:525-533
- [64] Ichimura K, Suzuki Y, Seki T, Hosoki A, Aoki K. Reversible change in alignment mode of nematic liquid crystals regulated photochemically by command surfaces modified with an azobenzene monolayer. *Langmuir*. 1988;**4**:1214-1216
- [65] Ishiguro M, Sato D, Shishido A, Ikeda T. Bragg-type polarization gratings formed in thick polymer films containing azobenzene and tolane moieties. *Langmuir*. 2007;**23**:332-338

